Atomisation process of turbulent liquid sheets : Experimental analyses and numerical developments

Trung-Thanh Vu

Normandie Université

THÈSE

Pour obtenir le diplôme de doctorat

Spécialité: Physique

Préparée au CORIA, Université et INSA de Rouen Normandie

ATOMIZATION PROCESS OF TURBULENT LIQUID SHEETS
EXPERIMENTAL ANALYSES & NUMERICAL DEVELOPMENTS

Présentée et soutenue par

Trung-Thành Vũ

Thèse soutenue publiquement le 12 juillet 2017 devant le jury composé de

M. Stéphane Vincent	Professeur, MSME, Université Paris-Est Marne-la-Vallée, Marne-la-Vallée	Rapporteur
M. Rudy Bazile	Maître de Conférences HDR, IMFT, INP de Toulouse, Toulouse	Rapporteur
M. Jérôme Hélie	Expert Senior, Responsable Equipe Nozzle & Sprays, Continental, Toulouse	Examinateur
Mme. Françoise Baillot	Professeure, CORIA, Université de Rouen Normandie, Rouen	Examinatrice
Mme. Marie-Charlotte Renoult	Maître de Conférences, CORIA, INSA de Rouen Normandie, Rouen	Examinatrice
M. Christophe Dumouchel	Directeur de Recherche, CORIA, Université de Rouen Normandie, Rouen	Directeur de Thèse
M. Thibaut Ménard	Maître de Conférences, CORIA, Université de Rouen Normandie, Rouen	Co-directeur

Thèse dirigée par Christophe Dumouchel & Thibaut Ménard

CORIA, Université et INSA de Rouen Normandie

UNIVERSITÉ DE ROUEN NORMANDIE

ED PSIME

UMR 6614 CORIA COMPLEXE DE RECHERCHE INTERPROFESSIONNEL EN AEROTHERMOCHIMIE

Dedicated to my family

REMERCIEMENTS

Je tiens à remercier Monsieur Mourad Boukhalfa, directeur du CORIA, pour m'avoir accueilli au sein de son laboratoire, et par la même occasion Madame Armelle Cessou qui lui a succédé.

Je souhaiterais exprimer ma gratitude à Messieurs Stéphane Vincent et Rudy Bazile qui ont accepté d'être rapporteurs de ces travaux. Leurs remarques éclairantes et leurs suggestions pertinentes me sont précieux. Je remercie également Mesdames Françoise Baillot et Marie-Charlotte Renoult ainsi que Monsieur Jérôme Hélie pour leur participation au jury.

L'expression de ma reconnaissance profonde va à Christophe Dumouchel, mon directeur de thèse, pour la confiance qu'il m'a accordée, pour sa grande disponibilité et pour ses multiples conseils prodigués tout au long de ces années.

Je sais gré particulièrement à Thibaut Ménard qui a co-dirigé cette thèse. J'ai beaucoup apprécié de travailler sous son encadrement empreint de suivi régulier et de bienveillance.

Je remercie Jean-Bernard Blaisot qui, avec une grande pédagogie et expertise, a nourri mes réflexions dans le traitement d'images. Je pense aussi à Denis Lisiecki, sans lequel les mesures expérimentales n'auront pas pu réalisées dans les meilleurs conditions.

L'environnement sympathique et studieux au sein du CORIA est le socle sur lequel je me suis appuyé pour mener à bien ce projet. Mes pensées tournent vers l'ensemble des chercheurs et le personnel du laboratoire qui a soutenu les thésards comme moi par leurs travaux quotidiens, leurs échanges enrichissants et leur bonne humeur: François-Xavier Demoulin, Jean Cousin, Jorge César Brändle de Motta, Benjamin Duret, Jérôme Yon, Wojciech Aniszewski, Nicolas Hecht, Geoffroy Vaudor, Valérie Thierry, Guillaume Édouard, Cédric Chambrelan, Nathalie Delahaye.

Mention spéciale à mes amis et collègues avec qui j'ai partagé les moments inoubliables, les voyages joyeux et les matchs de foot amusants pendant ces années magnifiques: Manu, Lila, Sylvia et Antonio, Andrés, Chanisa, Ly, Erwan, Fred, Amandine et Abou, Stan, Kamel, Julien, Marcos et Pilar, Arezki, Javier, Antoine, Stefano, Félix, Hassan et tant d'autres que je ne peux tous citer.

Les mots les plus simples étant les plus forts, je rends hommage à mes parents, à ma sœur et sa famille, à mes beaux-parents et ma belle sœur qui ont jamais douté de moi, et qui malgré la distance sont toujours à mes côtés.

A Ngoc-Anh, pour sa tendresse et son amour, et à notre petite qui apporte, dans notre vie, une joie incomparable.

CONTENTS

1

INTRODUCTION

Liquid fuel atomization is crucial for the performance of internal combustion engines. Through an injector, the liquid is delivered into the combustion chamber and breaks down into droplets. The finer the drops, the quicker their evaporation and the more proper their mixing with air. A proficient combustion could hence be expected, with low pollutant emissions.

Atomization quality is primarily affected by the injector design and the operating conditions which shape the internal flow structure, the turbulence level, the velocity profile at the nozzle outlet, the cavitation and so forth. All these features are determinants of the breakup of the external liquid flow. Another key parameter to optimize the atomization process is the fuel physical properties. One can think of, among others, the dynamic surface tension controlled by the diffusion of the surfactants on the liquid-gas interface or the extensional viscosity which makes a liquid more resistant to the stretching, thereby affecting the breakup.

Effects of the injector design, the operating conditions and the liquid properties on the atomization are inter-dependent. Analyses of experimental data help us to understand the involved mechanisms and their interactions. On the one hand, this is useful for the numerical developments which should be carried out depending upon the configuration. On the other hand, quantitative criterion could be established to validate the simulation results.

Following the above research methodology, we attempt to study the disintegration of planar turbulent liquid sheets produced by a triple-disk injector. Experimental measurements provide the sheet images, used as input for a multi-scale analysis. We investigate, thanks to the latter, the behaviours of the liquid sheet, the ligaments appearing on its edges and the resulting droplets. Moreover, two immersed boundary methods are developed, aiming to simultaneously solve the nozzle flow and the breakup process. We carry out two applications, the first one on a liquid jet ejected by a cylindrical nozzle and the other a planar sheet issuing from a triple-disk injector.

2

LITERATURE REVIEW ON ATOMIZATION OF LIQUID SHEETS

In this chapter, an overview on the sheet atomization based on several survey articles is given. We briefly describe how a liquid jet breaks up under the Rayleigh-Plateau instability. Then, four methods forming liquid films are shown, together with the disintegration of the latter. The planar sheets issuing from a triple-disk injector are focused on in our study. Their particular features explain why we conduct different developments presented in the next chapters.

2.1 ATOMIZATION & BREAKUP OF LIQUID JETS

Atomization refers to the process during which a compact liquid volume breaks up into a spray, defined as a flow of small and dispersed drops. The droplets differ from one another in size, form, position and velocity. A well-known example is probably the breakup of a slender jet into a train of droplets under the Rayleigh-Plateau instability (Fig. 2.1). Exhaustive reviews on the examination of this phenomenon are available in Eggers 1997 [31], Eggers & Villermaux 2008 [32].

Savart 1833 [83], from his pioneering experiments, remarks that a cylindrical jet is unstable because of the disturbances applied on it at the opening of the nozzle. Plateau 1849 [74] concludes that the surface tension, by boosting the perturbations which reduce the liquid's surface area, is the origin of the instability. Indeed, the surface tension is caused by the attraction of the liquid molecules. Those on the liquid-gas interface have no neighbours above, and are therefore pulled inwards. This makes the liquid surface acquire the least surface area possible (Morrison 2013 [62]).

Additionally, as stated in Plateau 1849 [74] since the perturbations of long wavelength tend to reduce the surface area, they are favoured by the surface tension. It can be seen in Fig. 2.1 that perturbations make the cylinder surface wavy with the

presence of necks and crests. At each point on the surface there are two curvatures: κ_1 corresponds to the circle in the section perpendicular to the cylinder axis, and κ_2 the wave in the section along the cylinder axis. κ_1 is not homogeneous along the undulating stream, and neither does κ_2. The difference of κ_1 at a neck and a crest comes from the size disparity of the circle at these two positions, while that of κ_2 lies in the fact that its positive value at a crest turns negative at a neck. The difference in κ_1 results in a pressure gradient which drives the fluid from the neck to the crest, increasing the wave amplitude. The difference in κ_2 and the relating pressure gradient, on the other hand, conducts the fluid the other way round, thus lessening the development of the disturbing undulation. Obviously, the longer the wavelength of the perturbations, the smaller the difference in κ_2.

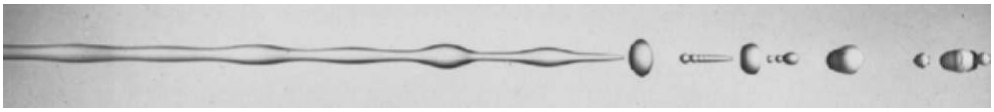

Figure 2.1: A decaying jet (Rutland & Jameson 1971 [82])

Nevertheless, the surface tension can not be the only driving agent of the instability as it would otherwise result in the collection of the entire fluid into a single large sphere to attain the smallest surface area. As argues Rayleigh 1879 [78], the inertia matters to the liquid thread decay, too. An internal flow, created by the pressure gradient, evokes the growth of the displacement amplitude which initiates the drop formation. When the pinched areas rupture, the bulged areas transform into droplets. This is due to the inertia which prevents the liquid from being transported from the necks to the crests since these latter are too far from each other in long-wavelength perturbations (Charru 2011 [8]). Rayleigh 1879 [78] provides a linear analysis where disturbances over a fluid column of diameter a are represented by a series of periodic displacement sinusoids. Perturbations of long enough wavelengths will grow larger in time. It is found that the fastest perturbation has an optimal wavelength of

$$\lambda_{opt} = 4.51a \tag{2.1}$$

and a growth rate of

$$\beta_{max} = \frac{0.344}{\sqrt{\frac{\rho a^3}{\sigma}}} \tag{2.2}$$

When its amplitude is equal to the jet radius and under the assumption that one drop is formed per optimal wavelength, the pinch-off occurs and the typical drop size is set to be

$$d = 1.89a \tag{2.3}$$

The existence of smaller satellite drops beside the large main ones, as noticed by Savart 1833 [83], can only be understood by considering the non-linear dynamics of the jet breakup (Yuen 1968 [108], Goedde & Yuen 1970 [41], Rutland & Jameson 1971 [82], Pimbley & Lee 1977 [73], Vassallo & Ashgriz 1991 [97], Papageorgiou 1995 [70], Kowalewski 1996 [50], Brenner et al. 1997 [7], Risso 2000 [80] for instance).

2.2 DISINTEGRATION OF LIQUID SHEETS

2.2.1 *Linear theory*

Atomization involves, in many types of spray nozzle, the change of the flow topology into an unstable planar sheet. Like the fluid thread breakup, the onset of the disintegration of a liquid film can be investigated by the linear stability theory similar to Rayleigh 1879 [78]. A survey of the researches following this approach is given in Sirignano & Mehring 2000 [84].

Squire 1953 [85] and Hagerty & Shea 1955 [45] assume that the disturbance upon the interface is periodic in space and grows in time everywhere at the same rate. Squire 1953 [85] considers a liquid sheet of constant thickness moving in a still gaseous environment. Both fluids are inviscid. The author analyses only the sinuous type of perturbation where the two surfaces of the film oscillate in phase (Fig. 2.2a). When the perturbation wavelength is large compared to the sheet thickness and the gas-to-liquid density ratio is of the order of 10^{-3}, it is proven that a plane liquid film is unstable if We is greater than unity. The liquid Weber number We is

a measure of the relative importance of the fluid's inertia compared to its surface tension

$$We = \frac{\rho U^2 h}{\sigma} \tag{2.4}$$

where ρ, U, h, and σ denote the liquid density, the velocity of the sheet, the half film thickness and the surface tension, respectively. In other words, an instability can develop on a liquid sheet if there is a certain difference in velocity between the two fluids. The sheet instability is thus driven by the Kelvin-Helmholtz instability. Main sources of instability arise from the aerodynamics forces released by the interactions between the liquid film and the surrounding gas (Oesterlé 2006 [67]). Contrary to the breakdown of a cylindrical jet, surface tension is the counter part of the process here. Another important finding presented in the paper of Squire 1953 [85] is the wavelength and the growth rate of the most unstable oscillation:

$$\lambda_{opt} = \frac{8\pi h}{We_g} \qquad \text{and} \qquad \beta_{max} = \frac{U}{4h}\sqrt{We_g} \tag{2.5}$$

The gaseous Weber number We_g is defined in the same fashion to the liquid Weber number (2.4) except the liquid density ρ is replaced by the gas density ρ_g.

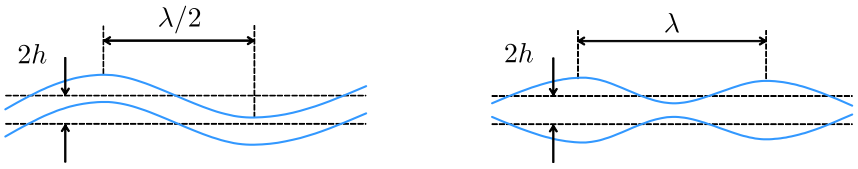

(a) Sinuous wave (b) Dilatational wave

Figure 2.2: Two basic wave forms

Meanwhile, Hagerty & Shea 1955 [45] conclude that only two types of instabilities may develop on the surfaces of the liquid sheet. Either the two surfaces of the film oscillate in-phase to produce sinuous waves, i.e. anti-symmetric mode (Fig. 2.2a), or they oscillate out-of-phase to generate dilatational waves, i.e. symmetric mode (Fig. 2.2b). Besides, it is demonstrated that the anti-symmetrical disturbances always grow faster than the symmetrical ones and mask the latter throughout the process.

2.2.2 *Breakdown of liquid films in different configurations*

Liquid sheets can be formed in a variety of ways: through fan nozzles, by the impingement of two cylindrical jets, by means of the impact of a jet on an obstacle or via compound nozzles among others. Concerning papers are carefully reviewed by Dumouchel 2008 [19]. Although the resultant sheets are quite different from one configuration to another, their breakup in a quiescent gas medium always occurs in three steps. First, deformations appear on the interface, their growth in time and space then creates ligaments, and finally drops are released from the rupture of these ligaments.

The disintegration of a liquid sheet, as depicted in Fig. 2.3, is described in Dombrowski & Johns 1963 [18]. On the interface, the initial perturbations give rise to unstable waves, among which a dominant one can be distinguished. It is the most rapidly amplified wave, growing at the rate of β_{max}, whose wavelength λ_{opt} is given by the linear stability theory developed by Squire 1953 [85] and Hagerty & Shea 1955 [45]. It is said that the wavy film fragments into pieces at each half wavelength $\lambda_{opt}/2$. Due to the surface tension, the broken parts roll up to form cylindrical threads, which subsequently undergo the Rayleigh-Plateau instability and break up into droplets (refer to § 2.1).

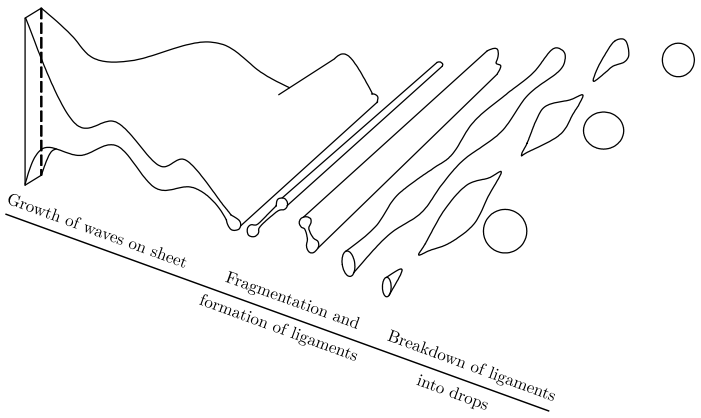

Figure 2.3: Disintegration scenario of a liquid sheet (Dombrowski & Johns 1963 [18])

2.2.2.1 *Fan nozzles*

The formation of liquid sheets using fan nozzles is by far the most common application. Figure 2.4 illustrates the discharge orifice of a fan nozzle. It is made by

the intersection of a V groove with a hemispheric cavity. Such a design provokes special approach passages which allow two streams to impinge behind the orifice (Lefebvre 1989 [51]). As the liquid spreads freely between the side walls, a thin film is generated in a plane perpendicular to the streams.

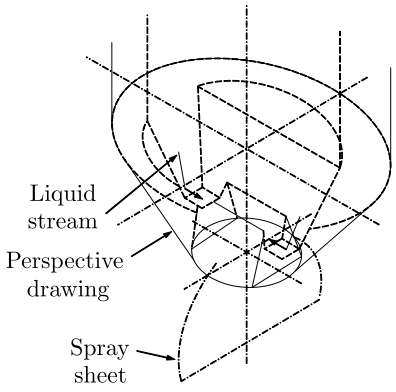

Figure 2.4: Mechanism of liquid flow through fan spray nozzles
(Dombrowski et al. 1960 [17])

A contribution to the literature of fan nozzle-generated liquid sheets should be the publication of Fraser et al. 1962 [37]. A set of single-hole fan nozzles are selected to investigate the effects of ambient atmosphere on two breakup modes namely sinuous and perforation. Flat liquid sheets are visualized by flash photography, while drops are collected in a cavity slide filled with oil and later recorded on a photomicrograph at high magnification. The authors measure the drop-size distribution from the photographic negative projected on a screen.

Only sinuous waves are observed under atmospheric pressure. When the density of the surrounding air ρ_a is reduced both breakup length and drop diameter increase. In accordance with the linear theory (see § 2.2.1), the growth rate of the fastest wave β_{max} must decrease with ρ_a. In consequence, the liquid film is disrupted further downstream where it becomes thinner. One could then expect threads to be narrow and droplets to be fine. However, the experiments performed by Fraser and his colleagues offer completely opposite results recording drops of larger size. As an explanation to this outcome, the authors argue that at diminished air density, while β_{max} decreases the optimal wavelength λ_{opt} gets longer. Therefore, the sheet fragments, corresponding to one-half wavelength $\lambda_{opt}/2$ (Fig. 2.3), contract into filaments with more liquid, offsetting the thinning of the sheet and leading to coarser spray.

Under partial vacuum conditions, the disintegration of a liquid film is switched into perforation mode. Perforation holes appear at the lower end of the sheet and extend until the disruption of the latter (Fig. 2.5b). The breakup takes place at a greater distance from the orifice than in the sinuous mode, and the sheet is thinner when it breaks down. Similar to what has been found in the experiments mentioned earlier, this results in a spray with mean drop-size higher than that of the sinuous mode. According to the authors, ligaments are derived from liquid originally included inside the large perforation holes. Without doubt, the bigger the perforation holes, the thicker the ligaments and the larger the drop diameter will be. It should be underlined that in both disintegration mechanisms, the liquid sheet always transforms into ligaments though by different manners.

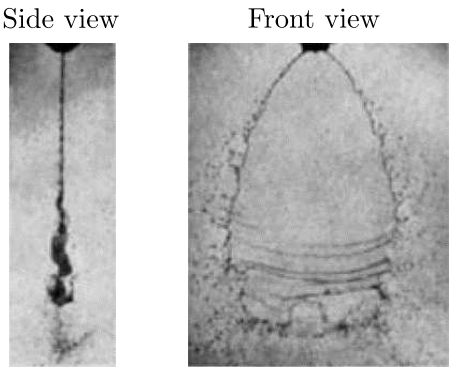

1.2 g/litre

(a) At atmospheric density

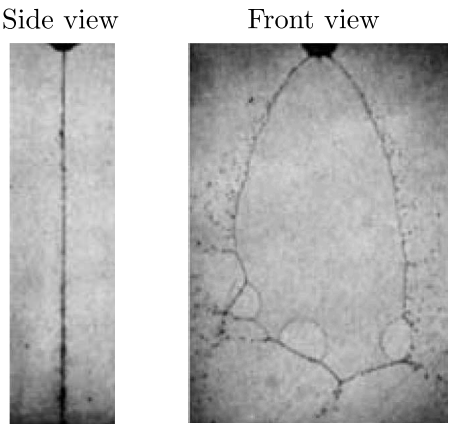

0.03-0.075 g/litre (29.25-28.25 Hg vacuum)

(b) At subatmospheric density

Figure 2.5: Fan nozzle-generated liquid sheets (Fraser et al. 1962 [37])

Fraser et al. 1962 [37] go further by putting forward an idealized fragmentation mechanism, similar to Fig. 2.3. The dominant wave is detached from the leading edge in form of a lamellae. The lamellae is parallel to the free rim and as wide

as a half optimal wavelength $\lambda_{opt}/2$. It contracts into a filament which is divided into drops of equal size. The authors use the optimum wavelength predicted by Squire 1953 [85] and assume that the volume of filament is identical to that of the lamellae. The drop diameter is deduced in accordance with Rayleigh's analysis [78]. It is found that the drop-size depends on the average velocity U, the film thickness S_b, the radial distance x_b at breakup, the mass density of liquid ρ and of air ρ_a and the surface tension σ as follow

$$d = C\left(\frac{\rho}{\rho_a}\right)^{1/6}\left(\frac{S_b x_b \sigma}{\rho U^2}\right)^{1/3} \sim We^{-\frac{1}{3}} \tag{2.6}$$

where C is a constant empirically obtained from the experimental dataset and We the liquid Weber number based on the film thickness.

It is worth noting that as shown in Fig. 2.5a, for most part, threads do not transversally fly off and there is no fragmentation in this direction (Brémond 2003 [5]). The disintegration scenario indicated in Fig. 2.3 by Dombrowski & Johns 1963 [18] seems to be open for criticism.

2.2.2.2 *Impact of a jet on an obstacle*

Letting a circular jet hit a solid disc of finite size at normal incidence is also an interesting method to form a flat liquid sheet (see Fig. 2.6a). Here, U_0 is the velocity of the incoming jet and D_0 its diameter. ρ and σ stand for the liquid mass density and surface tension, respectively. D_i represents the diameter of the solid disc. It can be observed from Fig. 2.6b that a radially expanding film is shaped, laying on the plane perpendicular to the jet axis and drops detach from the sheet at a radial position denoted by R (Fig. 2.6a).

In a series of two research articles, Clanet & Villermaux 2002 [14] and Villermaux & Clanet 2002 [101] examine the sheet creation under this scheme as well as its characteristics. The experiments are carried out in the same manner in both works. Visualization is made possible by a short exposure photograph system and a high speed camera. The sheet thickness is measured based on the light interference method. The velocity in the liquid film is studied with help of the tracking records of the ash particles scattered on the sheet surface. The drop-size is quantified thanks to the image analysis. The radial position where the transition from sheet

into drops occurs is given by the averaged images. It is found that this position grows linearly with the Weber number of the incoming jet (2.7) up to a critical value of the latter and decreases from this limit on.

$$We = \frac{\rho U_0^2 D_0}{\sigma} \tag{2.7}$$

The critical Weber number is able to discern two regimes of the sheet evolution. Clanet & Villermaux 2002 [14] scrutinize the first regime whereas the second one is left for further investigation in Villermaux & Clanet 2002 [101].

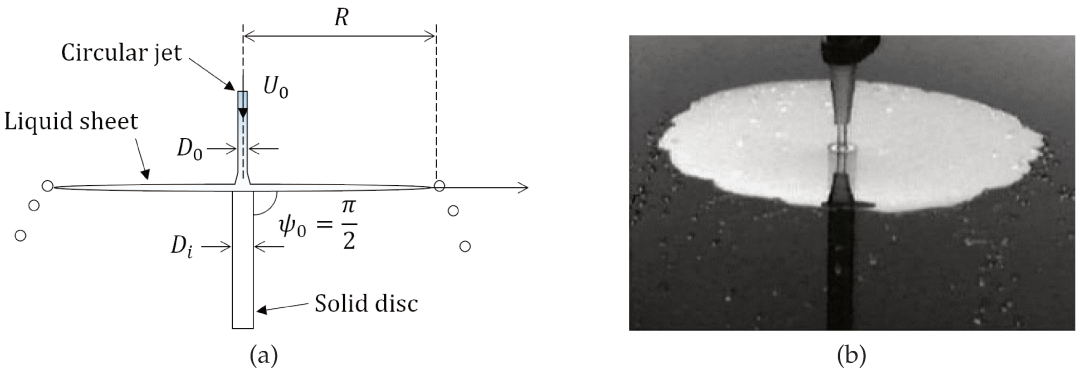

Figure 2.6: Diagram of a sheet formed by the impact of a liquid jet on a solid disc (a) and side-view of liquid sheet in smooth regime (b)
(Clanet & Villermaux 2002 [14])

Over the range of low Weber numbers, the sheet remains smooth before becoming free standing and droplets are expelled directly from its circumference (Fig. 2.7a). The interactions of the liquid film with the surrounding air is negligible. Clanet & Villermaux 2002 [14] state that the liquid sheet shows features that are comparable with the properties of the fan-nozzle sheets. First of all, the velocity along the radial direction is constant and equal to the velocity of the impact jet. Additionally, the sheet thickness is proportional to the inverse of the distance from the impact region.

The authors also provide a detailed explanation of the drop formation. When a fluid particle flows into the film periphery, the surface tension keeps it at a stagnation state, against the inertia force which pulls it outwards. Semi-cylindrical cusps appear on the border of the sheet and are continually fed by other incoming particles. Beads travel along the rim and when the body forces due to centrifugal acceleration and gravity overcome the capillarity attaching forces, drops tear off (refer to Fig. 2.7a). The attraction of the beads is caused by the core of the sheet

and thus could be characterized by its thickness at the detachment point. As a result of this local force balance, the mean drop-size varies as

$$\begin{aligned} d &\sim D_0 We^{-1/3} \qquad \text{for} \quad D_0 \ll a \\ d &\sim D_0 We_a^{-1/3} \qquad \text{for} \quad D_0 \gg a \end{aligned} \tag{2.8}$$

where $We_a = \frac{\rho U_0^2 a}{\sigma}$, $a = \sqrt{\frac{2\sigma}{\rho g}}$ the capillary length and g the gravitational acceleration.

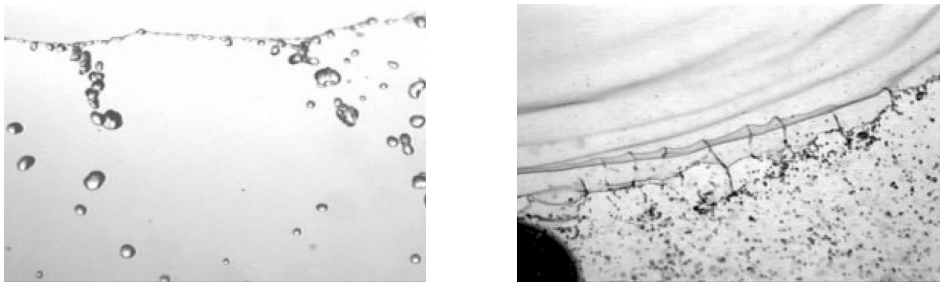

(a) (b)

Figure 2.7: Close-up view of the edge of the sheet in smooth regime (a) (Clanet & Villermaux 2002 [14]) and in flapping regime (b) (Villermaux & Clanet 2002 [101])

When the Weber number (2.7) exceeds a critical value beyond which the radial extent of the sheet starts to decrease, the flapping regime occurs. As shown in Fig. 2.7b, the liquid film sustains a shear, flag-like instability under the Kelvin-Helmholtz mechanism. Drops are ejected from the ligaments which are intermittently detached from the periphery of the sheet. Now, the surrounding medium is proved to play a crucial role in the process interacting with the liquid sheet, in contrast to the smooth regime. On the one hand, the flag instability happens at a higher Weber number when one lessens the air density. On the other hand, not only the liquid jet but also the ambient gas determine the breakup radial position which is linked to its determinants by

$$R \sim D_0 \left(\frac{\rho}{\rho_a}\right)^{1/6} \left(\frac{1}{We}\right)^{1/3} \tag{2.9}$$

Furthermore, Villermaux & Clanet 2002 [101] analyse the transverse cut of the sheet using planar laser illumination. The film thickness has no influence on the wavelength of the most amplified wave, in agreement with the linear theory. Yet the associated growth rate is found to be stronger than exponential. This could be accounted for, according to the authors, by the continuous thinning of the sheet

while approaching the rim. Besides, the group velocity of the waves is derived from the radial displacement of the crests of the sheet disturbances which are recorded in time-resolved images. Then, the mode selection of the instability is calculated from the time interval between two crests as they reach the rim (Fig. 2.8).

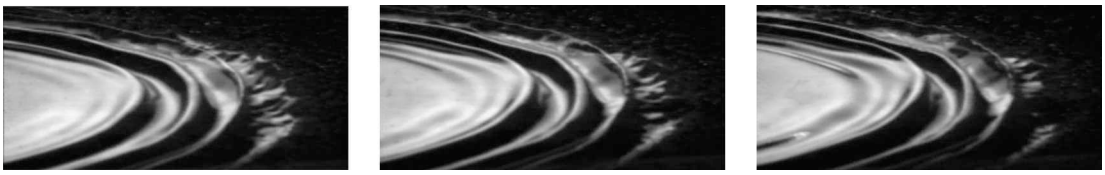

Figure 2.8: A time-resolved series of the sheet undulation waves propagating towards the rim (Villermaux & Clanet 2002 [101])

More importantly, Villermaux & Clanet 2002 [101] advance a drop formation scenario which is different to that of Dombrowski & Johns 1963 [18]. The liquid propagating at constant velocity in the sheet perceives, in its own frame of reference, a recurrent acceleration given by the periodic passage of the sheet undulations (see Fig. 2.9).

The forces that act on a fluid particle moving in the sheet are nearly balanced. Two possibilities can arise. When the surrounding medium's density is close to zero, the forces are strictly balanced. This is because the sheet sustains neutrally stable waves resulting from the equilibrium between the liquid inertia and the surface tension. Otherwise, the disequilibrium induced by the depression in the ambient phase will lead the wave amplitude to increase. Due to the difference in velocity between the liquid and the waves, a fluid particle experiences transient accelerations. In particular, the component of the acceleration which is parallel to the sheet is alternately directed towards and away from the liquid. When it is directed away from the liquid and when the force balance ensured by the surface tension has broken, the drops tear off from the sheet rim. In other words, the periodic passage of the sheet undulations triggers a Rayleigh-Taylor instability which produces liquid fingers or indentations perpendicular to the free rim. The typical size of these fingers is the Rayleigh-Taylor wavelength

$$\lambda_{\perp} \sim \sqrt{\frac{\sigma}{\gamma \rho}} \tag{2.10}$$

where γ stands for the acceleration of the detaching drop.

Ligaments initially take the form of the strips of the liquid and then develop further in the stream-wise direction. Drop should be released at the tip of the Rayleigh-Taylor indentations. The drop-size is therefore close to the instability wavelength and scales with We^{-1}. One could interpret the above result as the force balance when a droplet of size d peeled off from a strip of thickness $\lambda_\perp$. At the very moment, the relationship reads

$$\rho d^3 \gamma \sim \sigma \lambda_\perp \tag{2.11}$$

Figure 2.9: Shape of the liquid sheet close to the rim showing a primary undulation of wavelength λ and the component γ of the acceleration experienced by the liquid parallel to the sheet (Villermaux & Clanet 2002 [101])

2.2.2.3 *Impingement of two cylindrical jets*

The third way to produce planar sheets is the impingement of two liquid jets. Figure 2.10 sketches the experimental set-up from Brémond & Villermaux 2006 [6] where two identical cylindrical jets of diameter d_j and velocity u_j collide at an angle α from the line of impact. They form a liquid film perpendicular to the plane on which their axes lie. It can be seen that the sheet is radially broadening, though being shifted downwards from the point of the jet collision. It resembles to a leaf surrounded by a thick rim (Fig. 2.12a).

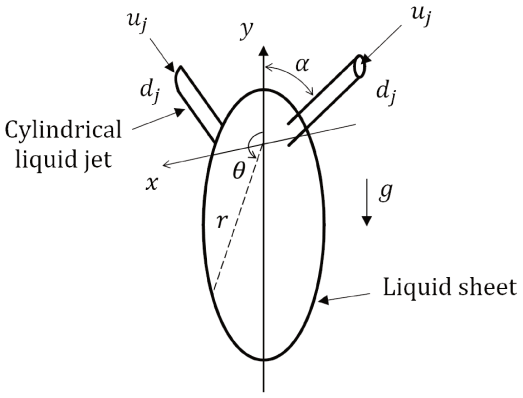

Figure 2.10: Liquid sheet formed by the oblique collision of two identical cylindrical jets (Brémond & Villermaux 2006 [6])

Brémond & Villermaux 2006 [6] utilize the image analysis to study the behaviours of the liquid sheets. A back-light optical arrangement is installed to record the frozen images of the spray, from which the authors derive the drop-size distribution. An interferometric technique is employed to quantify the sheet thickness.

The authors explain that the film size in the smooth basic state (Fig. 2.12a) depends on the collision conditions: the velocity of the liquid jets, its diameter and the impact angle. They re-find that these problems involve an equilibrium between inertia and capillarity. The stationary shape thus displays a Weber number similarity, as demonstrated before by Taylor 1959 [94], Huang 1970 [49], Clanet & Villermaux 2002 [14]. Concretely, for several Weber numbers (2.12) and a fixed impact angle the sheet contours normalized by $We \times d_j$ collapse in a unique shape. We is the Weber number of the liquid jet.

$$We = \frac{\rho {u_j}^2 d_j}{\sigma} \tag{2.12}$$

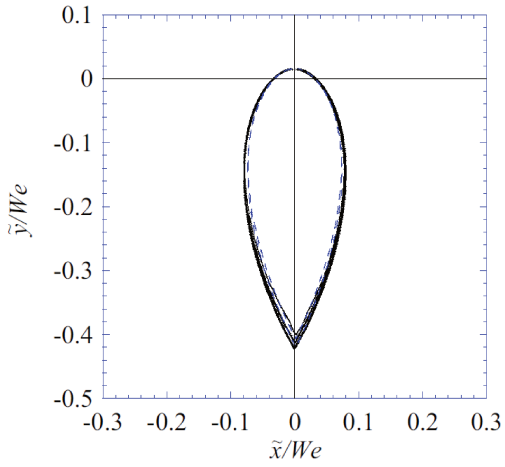

Figure 2.11: Liquid sheet contours at basic state normalized by $We \times d_j$. $\alpha = 45^o$
Continuous curves: $d_j = 1.05$ mm, We varies between 106 et 324.
Dashed curves: $d_j = 1.42$ mm, We varies between 90 and 160.
(Brémond 2003 [5])

At the sheet border, which is perturbed by a tungsten wire coming close to it, the disturbances appear and grow until ligaments are formed with their feet attached to the rim (Fig. 2.12b). These ligaments then elongate and decay into droplets (Fig. 2.12c). It is remarked that the growth of the perturbations modifies the sheet contraction mechanism. When the amplitude of the perturbations overcomes the thickness of the rim, the sheet contraction is accelerated because the inner part

of the liquid film is much thinner than the rim size. The authors claim that there is a coupling between the rim destabilization and the sheet thickness modulation. By tracking the trajectory of a single particle seeded on the film, it can be demonstrated that the speed at which the thickness field modulations propagate is the same as the particle velocity and thus identical to that of the fluid. The oscillation of the sheet thickness occurs at a constant atomization frequency.

The authors also find out that the rim destabilization is rather due to the capillary instability but not a signature of the wire wake. Three reasons can warrant this conclusion. First, the frequency of the rim destabilization remains unvarying irrespective of the jet velocity and the wire size. Additionally, the optimum excitation is attained when the vibration frequency corresponds to a spatial wavelength of the order of the rim radius. And finally, one drop is released per wavelength with its size proportional to the local rim diameter. Nevertheless, since the rim is fed by the liquid flowing in the sheet it bears a non-uniform, accelerated axial velocity. The instability mechanism is therefore unlike the classical configuration.

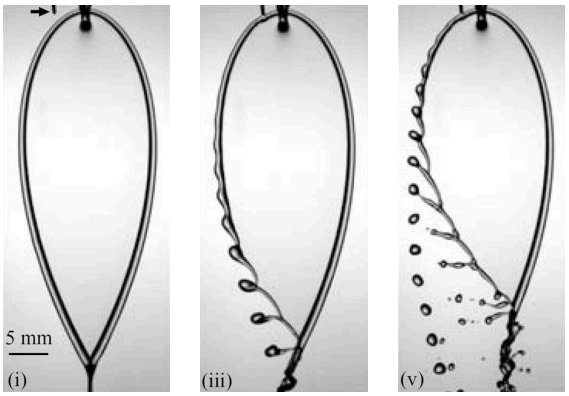

Figure 2.12: A sheet rim is increasingly perturbed from left to right by a small tungsten wire (Brémond & Villermaux 2006 [6])

Brémond & Villermaux 2006 [6] terminate their paper by inspecting the stretching rate of the ligaments. They propose that if the variable is weak, the corrugation of a ligament is pronounced giving irregular drops. In contrast, when the ligament elongates strongly, its skin is smooth when it leaves the rim and the drop-size distribution will be narrow. The authors give a rough estimation of the stretching rate γ, which is of the order of

$$\gamma \sim \frac{1}{\alpha\sqrt{We}} \tag{2.13}$$

2.2.2.4 *Compound nozzles*

We now consider the flat liquid sheet formation via compound nozzles which is our configuration of interest. Such atomizers are usually operated at low pressure drive in gasoline port-fuel injection. One of them could be a triple-disk injector as employed by Dumouchel et al. 2005 [22] (see Fig. 2.13). The injector has three superposed disks having each one circular hole. Specifically, the discharge orifice is deviated from the injector axis. As a result, a complex internal flow is established: a secondary non-axial flow which organizes as a double counter-rotating swirl at the nozzle exit as shown in Fig. 2.14 (Heyse et al. 1997 [47], Nagasaka et al. 2000 [63]) and a consistent turbulence level (Glodowski et al. 1996 [40], Chen et al. 1998 [9]). Dumouchel et al. 2005 [22] compute internal flow by a Reynolds-averaged Navier-Stokes (RANS) approach and a turbulence model named renormalization group (RNG) $\kappa - \epsilon$. Drop-size distributions are measured via a laser diffraction technique.

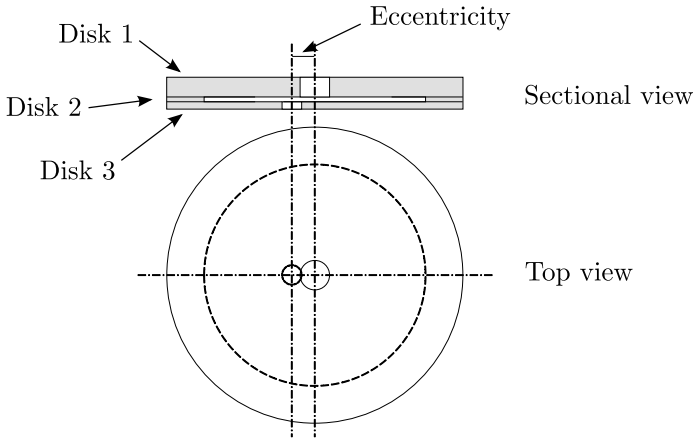

Figure 2.13: Triple-disk injector (Dumouchel et al. 2005 [22])

Furthermore, the authors suggest an atomization scenario where the swirl stretches the flow to form a flat sheet (Fig. 2.15). At the sheet edges, some of the turbulence-induced perturbations grow until the liquid system rearranges as a ligament network. The collapse of these ligaments eventually produces droplets. Figure 2.16 depicts a strong linear relationship between the non-axial kinetic energy and the turbulent kinetic energy against the surface energy of the spray. Both secondary flow and turbulence are therefore responsible for the spray formation. Meanwhile, the aerodynamic forces have negligible effects because the gaseous Weber number is small.

Besides, the internal dimensions are explored by considering various compound nozzles. The diameter of the discharge orifice is kept constant while different thicknesses and offsets are evaluated. Like Michalek et al. 1997 [61] and Parrish & Evers 1995 [71], it is confirmed that the cavity height and the eccentricity of the discharge orifice are the most important geometry parameters. Dumouchel et al. 2005 [22] identify an optimal geometry able to produce highest energy available for atomization, i.e. the non-axial kinetic energy and the turbulent kinetic energy.

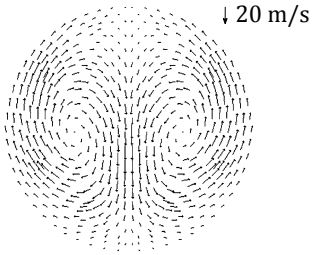

Figure 2.14: Double counter-rotating swirl at the nozzle exit (Dumouchel et al. 2005 [22])

Favourable effects of the swirl on the spray formation come from two reasons. As the swirl is stronger, the radial expansion of the sheet is more pronounced. Consequently, its thickness is reduced to yield further small drops. In addition, turbulence is enhanced by the wall friction. At high injection pressure or with low viscous liquid, it becomes high enough to promote initial perturbations. Hence, ligaments near the nozzle exit are more numerous, smaller in size and may disintegrate in finer droplets.

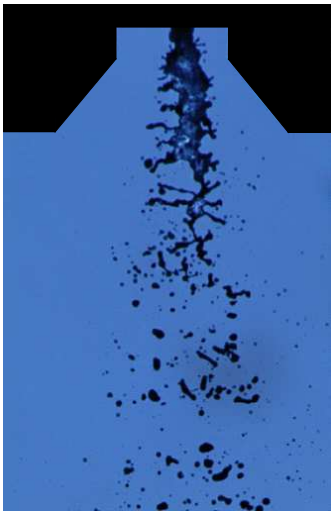

Figure 2.15: Breakup of a water sheet (Grout et al. 2007 [43])

In a direct continuation of this study, Grout et al. 2007 [43] apply the fractal analysis to the back-lighted images of the liquid sheet. Near the injector outlet, the tex-

tural fractal dimension which characterizes the tortuosity of the liquid-gas interface correlates with the Reynolds number. The authors claim therefore that turbulence promotes perturbations on the liquid-gas interface. Further downstream, the flow reorganizes into a ligament network and the ligaments disrupt into droplets. Grout et al. 2007 [43] measure the structural fractal dimension which represents the above processes and note that it scales with the Weber number. Clearly, the reorganization of the flow and the rupture of the ligaments are dominated by the surface tension forces.

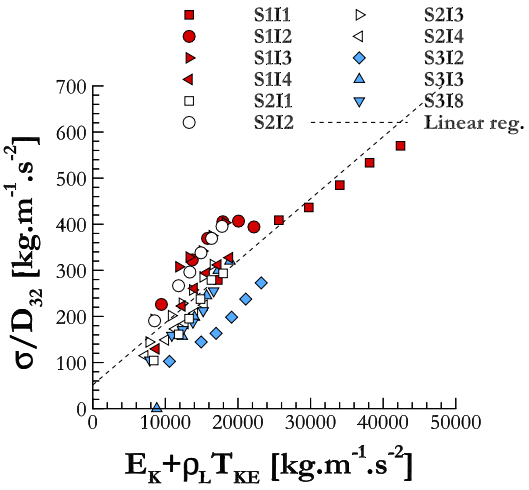

Figure 2.16: Per unit volume, surface energy of the spray against non-axial kinetic energy and turbulent kinetic energy (Dumouchel et al. 2005 [22])

2.3 OBJECTIVES OF THE THESIS

We have outlined, in this chapter, essential features of the breakup of liquid sheets in different configurations, showing the complexity of the liquid-gas interface evolution. Furthermore, the flow that develops inside the triple-disk injector as well as the sheet breakup are described in details thanks to the preceding works. Two remarks can be made from this literature review, explaining why we pursuit different developments in the next chapters.

Firstly, it is shown that the nozzle flow has significant effects on the sheet breakdown. In the injector exit section, the double vortex stretches the flow to form a planar liquid film. A consistent turbulence enhances the perturbations to grow until a ligament network is formed at the sheet borders. These ligaments eventu-

ally break up into droplets. To numerically solve the atomization process, we aim to include both internal and external flows in a unique simulation. Hence, two relevant immersed boundary methods are developed and coupled with a level-set/volume-of-fluid/ghost-fluid method in chapter 5, taking into account the irregular form of the injector wall in a Cartesian grid. For validation purpose, the numerical results are compared with other studies available in the literature for two well-documented configurations. We apply the immersed boundary methods to numerically simulate a jet emanating from a cylindrical nozzle as well as a liquid sheet generated by a triple-disk injector.

In addition, mechanisms of interface evolution occur at the same time but at different scales throughout the breakup of the liquid film. A back-lighting optical arrangement is built in chapter 3 to record the sheet images. The latter serve as inputs for a multi-scale tool in chapter 4, with its first application on the deformation of the entire liquid system. It appears that the perturbations on the sheet edges have a significant impact on the liquid film contraction. Moreover, the dynamics of the production and breakdown of the ligaments are also analysed, showing their effects on the poly-dispersion of the resulting spray.

Conclusions and perspectives are drawn in chapter 6, summarizing principal developments and main results of the thesis and several improvements in the future.

3

EXPERIMENTAL WORK AND IMAGE PROCESSING

We now introduce a home-made back-light optical set-up, constructed to visualize the atomization process. In fact, the back-lighted images of the liquid sheets emanating from a triple-disk injector are recorded. They will serve as inputs for the multi-scale tool in chapter 4.

This chapter begins with the presentation of the hydraulic circuit, followed by the injector design, the working fluids and the operating conditions. Then, some features of the visualization system are specified and the resultant back-lighting photographs are exhibited. We close the chapter with the image processing, carried out thanks to the C/C++ programs developed by Jean-Bernard Blaisot and his colleagues and the software ImageJ (`https://imagej.nih.gov/ij`).

3.1 HYDRAULIC CIRCUIT

The objectives of the hydraulic circuit are twofold: transferring liquid from a supply to the triple-disk injector which throws out a planar sheet (refer to § 2.2.2.4), and controlling the pressure at the nozzle inlet. The layout of the system can be seen in Fig. 3.1.

The starting point of the system is a cylindrical reservoir, used as a source of liquid supply. We put next to it a separator tank, having its volume divided into two deconnecting parts by a piston. To transfer the working fluid from the reservoir to the lower part of the separator tank, air in the upper part is sucked out by a vacuum pump. We control the liquid amount via a level indicator. The reservoir and the separator tank have each the same height, but the volume of the former is slightly higher than that of the latter to ensure that no gas remaining beyond the top level of the liquid inside the reservoir can be transported to the separator tank.

Once the isolation valve is opened, the fluid stored in the separator tank is pressurized towards the atomizer by air coming from the compressed air network of the laboratory. Remark that the liquid and the compressed air are isolated by the piston to prevent air bubbles from being admitted inside the injected fluid.

The circuit's ending point is the triple-disk injector. It is installed on a three-dimensional (3D) displacement system, suitable for visualizing the liquid flow at several distances from the nozzle in order to cover the whole disintegration process of the liquid films. A filter is placed before the atomizer to remove solid particles from the liquid. We collect the formed spray by a recovery cavity.

To fulfil the second target of the hydraulic circuit, the injection pressure is monitored over the $0 - 7$ MPa range by a pressure regulator. Three pressure gauges are mounted on several positions in the system for local indication of pressure and safety check. They bear the labels (1), (2) and (3) in Fig. 3.1. The pressure gauge (3) indicates the injection pressure.

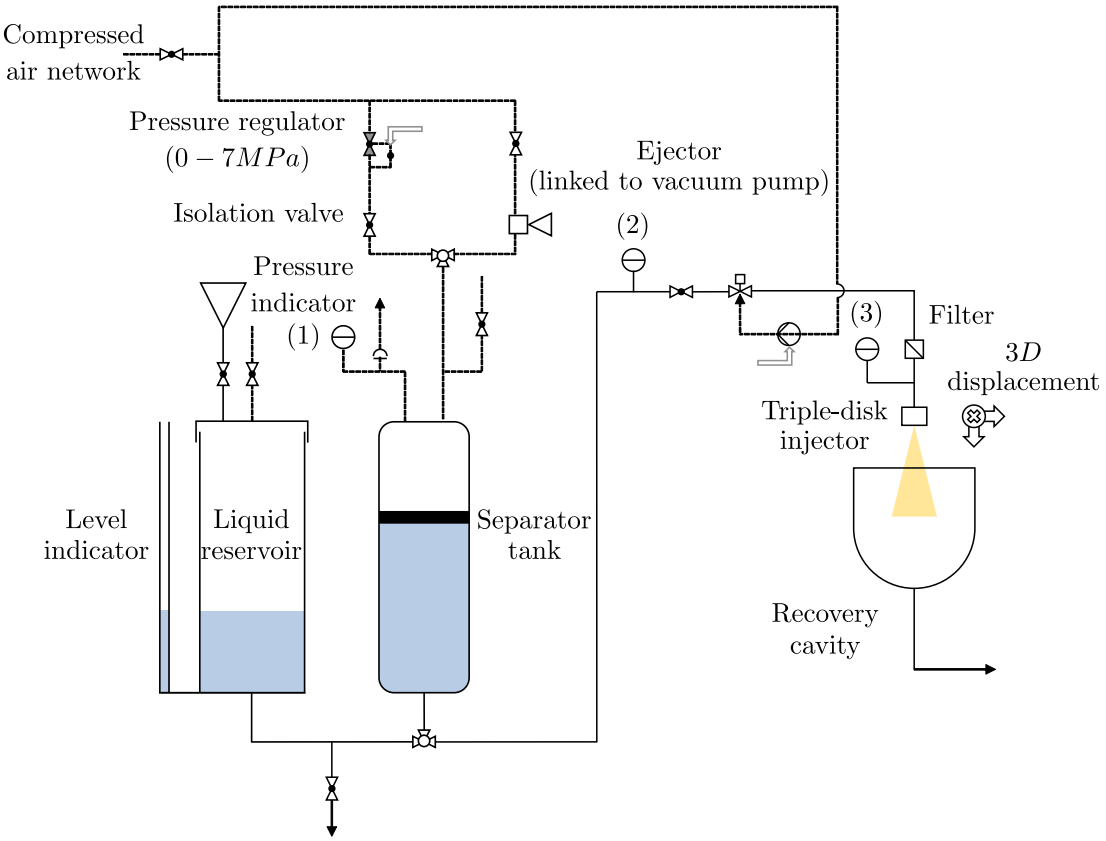

Figure 3.1: Hydraulic circuit (Courtesy of Denis Lisiecki)

Figure 3.2 shows two cutting plans of the triple-disk injector utilized in our study. The height and diameter of three superposed disks that constitute the nozzle are also depicted.

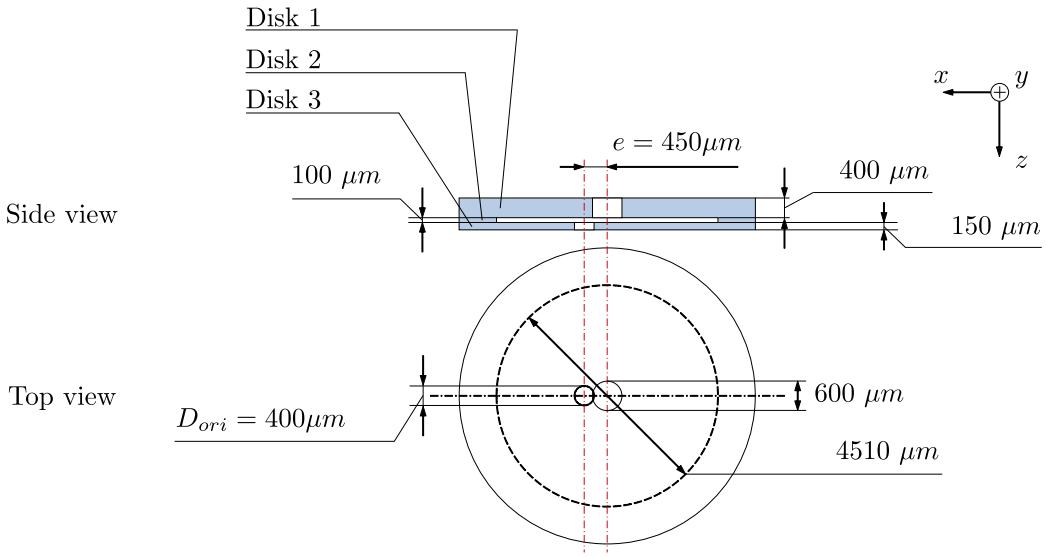

Figure 3.2: Geometrical characteristics of the triple-disk nozzle
(Eccentricity of the discharge orifice $e = 450$ µm)

Our device is proportional to the optimal geometry producing the highest energy available for the breakup process, i.e. the non-axial kinetic energy and the turbulence energy (refer to § 2.2.2.4).

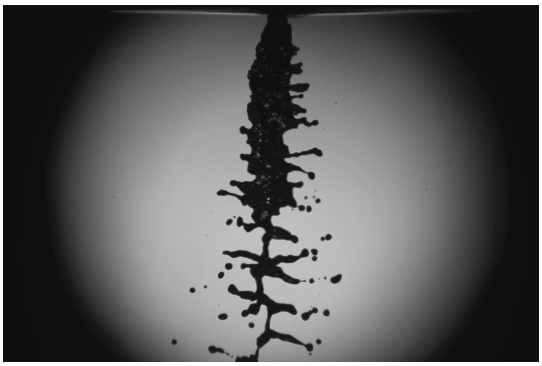

Figure 3.3: Production and disintegration of a water sheet
(Injection pressure $\Delta P_i = 0.1$ MPa)

The injection system is operated in continuous mode. Liquid is pressurized to flow from the separator tank to the triple-disk injector without interruption during an

experiment. It enters the nozzle by the metering orifice (disk 1 in Fig. 3.2), passes through the cavity (disk 2) and issues via the discharge orifice (disk 3). Due to the eccentricity of the latter, the flow is drastically deflected. Some fluid particles pass directly from the entrance to the exit of the nozzle whereas the others invade the cavity and reach the discharge orifice by a transversal way. Interactions of these trajectories provokes the secondary flow (Dumouchel et al. 2005 [22]). As shown in Fig. 3.3, in the plane of symmetry of the atomizer, a liquid film is formed as soon as the flow issues from the nozzle and becomes free of any parietal constraints, with perturbations developing on its edges. A ligament network is created further downstream, and eventually breaks down into droplets.

3.3 WORKING FLUIDS

Aiming to analyse the effects of the surface tension forces on the sheet breakup, fluids having surface tension coefficient which varies from one to another are necessary. To this end, isopropanol is blended with water in different proportions to obtain six mixtures called F0, F1, F2, F3, F5 and F10. The number indicates the mass percentage of isopropanol. F0 stands for water; and the mass fraction of isopropanol in F1, F2, F3, F5 and F10 are 1 %, 2 %, 3 %, 5 % and 10 %, respectively.

	σ [Nm^{-1}]	ρ [kgm^{-3}]	μ [Pas^{-1}]	ν [m^2s^{-1}]
F0	69.29×10^{-3}	997.92	0.99×10^{-3}	0.99×10^{-6}
F1	59.09×10^{-3}	995.98	1.03×10^{-3}	1.03×10^{-6}
F2	53.66×10^{-3}	994.06	1.07×10^{-3}	1.08×10^{-6}
F3	50.47×10^{-3}	992.10	1.14×10^{-3}	1.15×10^{-6}
F5	46.24×10^{-3}	988.90	1.26×10^{-3}	1.27×10^{-6}
F10	39.79×10^{-3}	982.04	1.62×10^{-3}	1.65×10^{-6}

Table 3.1: Physical properties of the liquids

Physical properties of the liquids are summarized in Tab. 3.1 where σ is the surface tension, ρ the mass density, μ the dynamic viscosity and ν the kinetic viscosity of the fluids. Surface tension is measured by the tensiometer LAUDA TVT 2. The device Anton Paar V3000 offers liquid mass density, dynamic and kinetic viscosities. Whereas their mass densities are similar, the surface tension decreases gradually while adding more isopropanol in water. Meanwhile, the tendency of the dynamic viscosity is inverse.

Low injection pressure is a desirable operating condition for our experiments. For that, three reasons can be given. First, it is expected to lessen the interactions between the liquid system and the ambient air as our objective is to study only the influence of the surface tension over the film breakdown. Second, it ensures that the ligaments are thick and the droplets are mostly on-focus for a better spatial and temporal description by the multi-scale analysis (chapter 4). Third, thicker liquid structures could be easily detected from the background. We thus maintain an injection pressure of 0.1 MPa because it is low enough and stable during all experiments.

To characterize the fluid system described in § 3.1, mass flow rate and metering velocity should be quantified. These parameters are mandatory to derive not only the discharge coefficient which indicates the performance of the system but also the non-dimension numbers which inquire into the atomization regime.

The usual measuring method is to weight the amount of the injected liquid within a controlled time interval. More precisely, it consists in a two-step procedure, repeated for three injection pressures comprising 0.07, 0.1 and 0.13 MPa. First, we set a desirable injection pressure ΔP_i and put on the hydraulic system during a duration Δt. Second, the fluid accumulated in the recovery cavity (see Fig. 3.1) is weighted to deduce the injected mass Δm. The mass flow rate Q_m for each injection pressure is given by

$$Q_m = \frac{\Delta m}{\Delta t} \tag{3.1}$$

and the metering velocity V_q is

$$V_q = \frac{Q_m}{\rho\left(\frac{\pi D_{ori}^2}{4}\right)} \tag{3.2}$$

where D_{ori} denotes the diameter of the discharge orifice.

One can compute the discharge coefficient C_D thanks to (3.3). The discharge coefficient is a dimensionless number used to characterize the pressure losses in fluid systems. It is defined as the ratio of the measured volumetric flow rate to the ideal-

ized value. The latter is traditionally inferred from Bernoulli's principle (3.3) and corresponds to an ideal nozzle which expands an identical working fluid from the same initial conditions to the same exit pressure without any losses.

$$C_D = \frac{Q_v}{\pi D_{ori}^2 \sqrt{\frac{\Delta P_i}{8\rho}}} \tag{3.3}$$

where ΔP_i is the injection pressure and Q_v the volumetric flow rate, easily derived from the mass flow rate Q_m as below

$$Q_v = \frac{Q_m}{\rho} \tag{3.4}$$

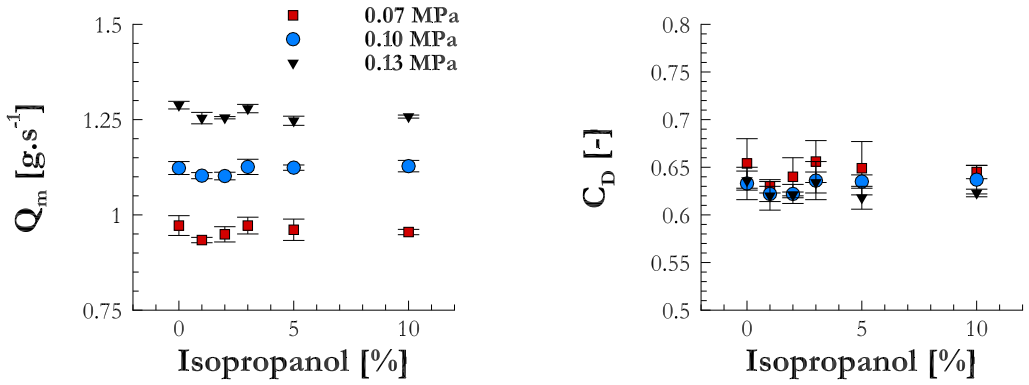

(a) Mass flow rate

(b) Discharge coefficient

Figure 3.4: Operating conditions

Figure 3.4 indicates the mass flow rate and the discharge coefficient for all fluids at three injection pressures. It appears that the mass flow rate increases with respect to the injection pressure only (Fig. 3.4a). Moreover, it stays unvarying for the six mixtures. These observations could be interpreted by the energy budget recommended by Dumouchel et al. 2005 [22] wherein pressure energy brought to the liquid is consumed as flowing energy, friction losses, non-axial kinetic energy and turbulent kinetic energy. In case of no friction loss or when the discharge coefficient is equal to unity, pressure energy is completely transformed into flowing energy and kinetic energies. As plotted in Fig. 3.4b, C_D remains around 0.65 for all working fluids and injection pressures. As a consequence, the flow is fully developed to attain well-established conditions. The discharge coefficient varies slightly although considerable changes in terms of viscosity are observed from

one liquid to another (Tab. 3.1). One can explain this result by the fact that with higher viscosity, friction losses increase; and non-axial kinetic energy and turbulence are diminished in their turn to compensate flowing energy and therefore keep the discharge coefficient at a stable value.

Table 3.2 exhibits the metering velocity V_q and the following dimensionless numbers and characteristic time which correspond to $\Delta P_i = 0.1$ MPa:

- The liquid Weber number indicates whether the kinetic or the surface tension energy is dominant.

$$We = \frac{\rho V_q^2 D_{ori}}{\sigma} \tag{3.5}$$

- The gaseous Weber number compares the aerodynamic forces to the surface tension. The larger this number, the stronger the interactions between the liquid flow and the surrounding medium and the finer the droplets will be.

$$We_g = \frac{\rho_g V_q^2 D_{ori}}{\sigma} \tag{3.6}$$

- The Reynolds number represents the relative importance of the inertia and the viscosity. It determines if the flow regime is laminar, transient or turbulent.

$$Re = \frac{\rho V_q D_{ori}}{\mu} \tag{3.7}$$

- The Ohnesorge number accounts for the influence of the viscosity on the atomization by relating a viscous time to a capillary one.

$$Oh = \frac{\mu}{\sqrt{\rho \sigma D_{ori}}} \tag{3.8}$$

- The capillary time is the characteristic time of the Rayleigh-Plateau instability.

$$t_\sigma = \sqrt{\frac{\rho D_{ori}^3}{\sigma}} \tag{3.9}$$

Notice that the gaseous Weber number is very small lying between 0.56 and 1.01. The interactions between the liquid system and the ambient air are negligible, according to Sterling & Sleicher 1975 [86]. Thus, the aerodynamic forces have negligible effects on the atomization process.

	V_q [ms^{-1}]	We [–]	We_g [–]	Re [–]	Oh [–]	t_σ [ms]
F0	8.96	462	0.56	3613	5.95×10^{-3}	0.96
F1	8.81	523	0.63	3408	6.71×10^{-3}	1.04
F2	8.82	576	0.70	3278	7.33×10^{-3}	1.09
F3	9.03	641	0.78	3143	8.06×10^{-3}	1.12
F5	9.04	699	0.85	2838	9.32×10^{-3}	1.17
F10	9.14	825	1.01	2216	12.96×10^{-3}	1.26

Table 3.2: Metering velocity and non-dimensional numbers
(Injection pressure $\Delta P_i = 0.1$ MPa)

3.5 VISUALIZATION SYSTEM

A back-light optical arrangement is implemented to image the liquid sheets which issue from the triple-disk injector. Figure 3.5 shows the schematic of the optical diagnostic, similar to that of Ngô 2013 [64]. A set of back-lighted pictures is acquired, useful for the multi-scale analysis.

The straightforward approach to designing a back-light configuration is to align its two principal components, namely a light source and a detector with the liquid film. As the latter is formed in the plane of symmetry of the injector (refer to § 3.2), these instruments are mounted on the axis perpendicular to this plane, one on the left of the sheet and the other on the right. The visualization plane coincides with the plane of symmetry of the nozzle (Ozx).

We employ a HSPS NANOLITE flash lamp as the light source. It emits incoherent and wide-spectrum pulse with a short duration of 15 ns. With the aid of a 140 mm lens between the flash lamp and the liquid sheet, light is diffused and a regular intensity of illumination is concentrated on the ejecting flow near the nozzle exit.

The detector consists of a camera, a shutter and an objective with extension ring. The CCD DALSA Panthera 11M4 camera offers a definition of $4016 \times 2672\ pixel^2$. The pixel size is $9\ \mu m$. To increase the magnification of the objective, an extension ring is placed between the camera and the objective. With the magnification of the optical system, the spatial resolution of the image is $3.5\ \mu m/pixel$ and its size is thus $14.06 \times 9.35\ mm^2$.

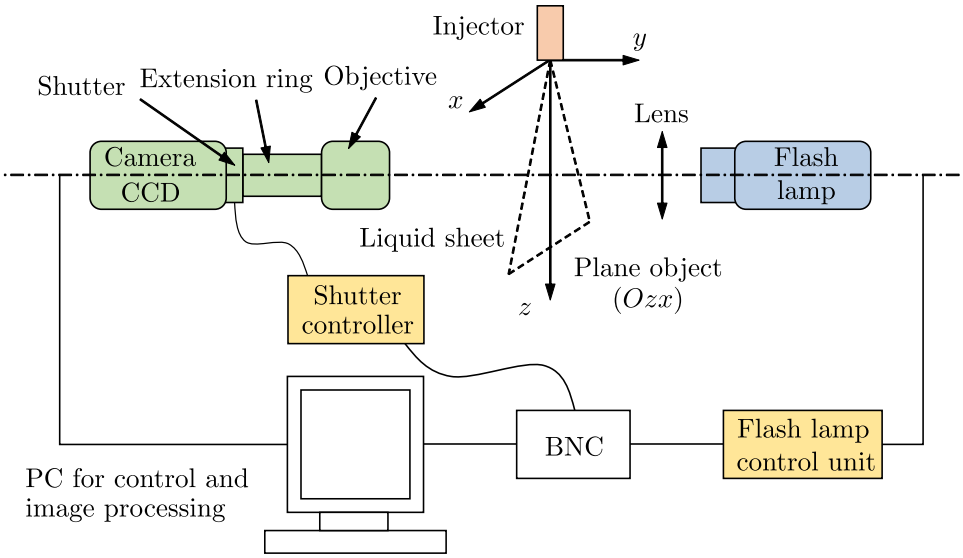

Figure 3.5: Visualization system

The synchronization protocol of the visualization system is as follows. The flash lamp is synchronized with the camera and triggered by TTL signals from its control unit. The BNC pulse generator sends a synchronization signal to trigger the flash lamp and the camera. After receiving the TTL signal, the flash lamp provides a brief bright light while the camera opens its shutter and capture an image. $8-bit$ images are transferred to the computer via an USB connection. The delays associated with the light source and the detector are adjusted so that there is enough light when the camera shutter opens.

We maximize the opening duration of the objective. The shutter is opened during $70\ ms$. The flash imposes the camera exposure time as its duration ($15\ ns$) gets shorter than that of the shutter ($70\ ms$). Remark that within a time interval of $15\ ns$, the displacement of the fastest fluid particle moving at a velocity of $9.14\ ms^{-1}$, as reported in Tab. 3.2, is approximately $0.14\ \mu m$. This displacement is much lower than the spatial resolution of the image ($3.5\ \mu m/pixel$), proving that our imaging system is able to freeze the breakup process under consideration.

Examples of the sheet back-lighting images are shown in Fig. 3.6. The top of these pictures coincides with the exit plane of the discharge orifice. One can notice that the shape of the liquid film evolves as soon as the flow leaves the injector outlet. Even though, the atomization is still not accomplished at the bottom of the photographs. To cover a larger part of the breakup of the system further downstream, we move the nozzle upward by a distance of 3.5 mm corresponding to a half of the height of the field of view (Fig. 3.7). Two vertical positions of the atomizer are considered hereafter, namely "up" and "down" as illustrated respectively in Figs. 3.6 and 3.7. Remind that they are separated by a 3.5 mm distance.

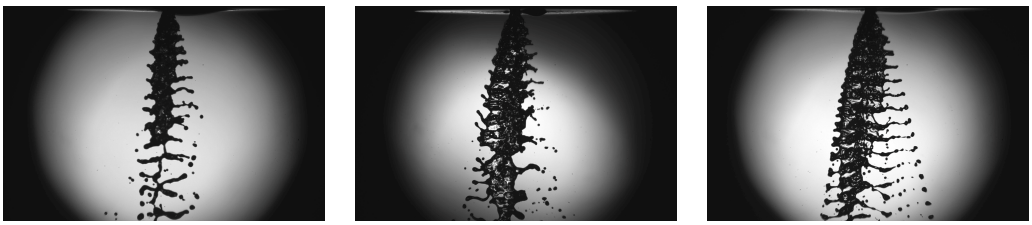

(a) F0 (b) F5 (c) F10

Figure 3.6: Snapshots of the liquid sheets - Position "up"

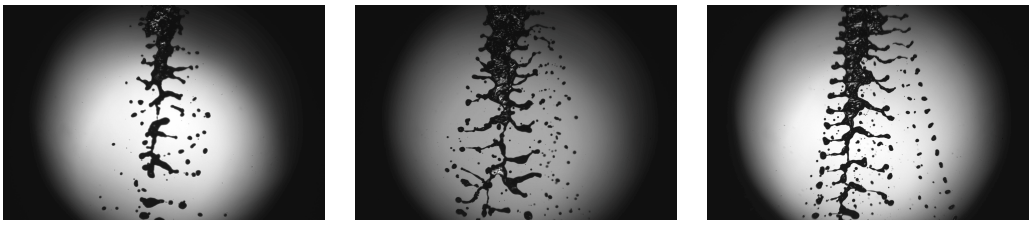

(a) F0 (b) F5 (c) F10

Figure 3.7: Snapshots of the liquid sheets - Position "down"

A grey-scale digital picture can be thought of as a 2D table (Figs. 3.6 and 3.7). We call each smallest element of the table "pixel". Its value carries intensity information or grey-level. Indeed, the grey-level is proportional to the illumination energy received by the camera during the exposure time of the latter. It is said in § 3.5 that this duration is enforced by the flash lamp and equal to 15 ns. We obtain $8-bit$ digital photographs which refer to 2^8 or 256 grey-levels ranging from 0 to 255. For the sake of clarity, let's consider an image I_m (Fig. 3.6a). I_m is a 2D

matrix of 4016×2672 $pixel^2$. The value that a pixel contains is $I_m(i,j)$ satisfying the conditions

$$0 \leqslant I_m(i,j) \leqslant 255 \qquad \text{with } i = \overline{1,4016} \text{ and } j = \overline{1,2672} \tag{3.10}$$

where i and j are respectively the horizontal and vertical coordinates of the pixel in the 2D grid I_m.

From a set of water sheet images in Fig. 3.8, it is clear that the background is not homogeneous and changes from one picture to another. The first step of the image processing thus involves the elimination of spatial and temporal variations in the background. Furthermore, it will be shown in the next chapters that the liquid-gas interface is crucial to perform the multi-scale analysis. Hence, the detection of the liquid sheet, the ligaments and the droplets, and the conversion of the images to binary should be included in the image processing as well. Details are provided in the following subsections.

(a) (b) (c)

Figure 3.8: Photographs of the water sheets

3.6.1 *Normalization*

In the current study, the purpose of the normalization is to correct inhomogeneities on the image background as well as snapshot-to-snapshot variabilities. These drawbacks are respectively caused by spatial and temporal fluctuations of the illuminating source.

We need two special photographs to perform the normalization process: the obscurity picture I_o taken without any light, and the background I_b where the flash

lamp is activated but not the atomizer. One can obtain the normalized image $\bar{I}_m$ (Fig. 3.9a) from the original one I_m (Fig. 3.6a) via the following formulae

$$\bar{I}_m(i,j) = \alpha \times \frac{I_m(i,j) - I_o(i,j)}{I_b(i,j) - I_o(i,j)} \times N_{background} \tag{3.11}$$

and

$$\alpha = \frac{I_{br}}{I_{mr}} \tag{3.12}$$

where I_{br} and I_{mr} are the average intensities calculated over a pre-selected rectangular zone of the images I_b and I_m, respectively. The rectangular zone in the image I_m must contain no object. Clearly, I_{br} and I_{mr} represent the average illumination energy received by the camera in the rectangular zones in these two pictures I_b and I_m. If there is no temporal fluctuations, the coefficient α is equal to unity. Otherwise, it varies around 1 and permits to correct the snapshot-to-snapshot variations on the background. Moreover, to rigorously keep the grey-scale of the normalized photograph in the 0 – 255 range, $N_{background}$ is set to be slightly lower than 255.

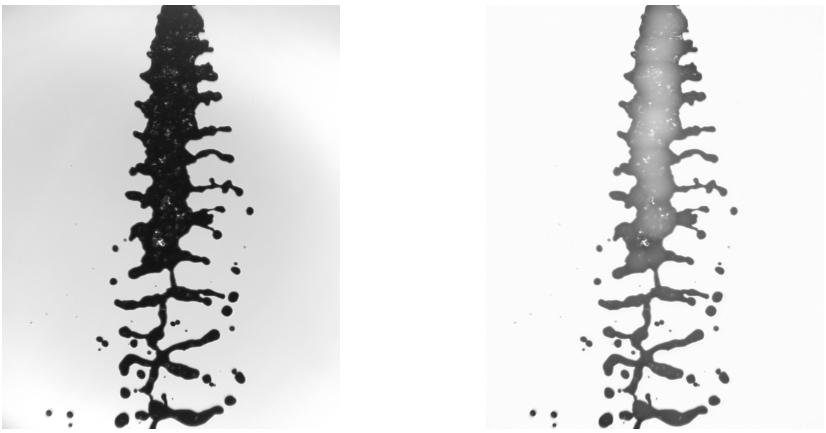

(a) Image $\bar{I}_m$ (b) After rolling ball operation $\bar{I}_m^{rb}$

Figure 3.9: Normalized images

In addition, we deal with the uneven illuminated background of the normalized image by the rolling ball algorithm. These spatial irregularities are due to the vibration of the spark discharge in the flash lamp. The plug-in of the software

ImageJ is based on Sternberg 1983 [87]. In our case, it seems to be appropriate to make the background more homogeneous.

Let's examine the resulting images, the first one $\bar{I}_m$ (Fig. 3.9a), and the second one $\bar{I}_m^{rb}$ resulted from $\bar{I}_m$ thanks to the rolling ball algorithm (Fig. 3.9b). The comparison could be done by their grey-level histograms, displayed in Fig. 3.10a for $\bar{I}_m$, and in Fig. 3.10b for $\bar{I}_m^{rb}$. For both cases, the liquid film and the filaments on its borders are made up of low value pixels. This explains why in the histograms, numerous pixels take moderate values approximately 50 in Fig. 3.10a or within the range of 60 to 160 in Fig. 3.10b. In contrast, the background is represented by high grey-levels (from 200 to 255 for $\bar{I}_m$ or around 250 for $\bar{I}_m^{rb}$).

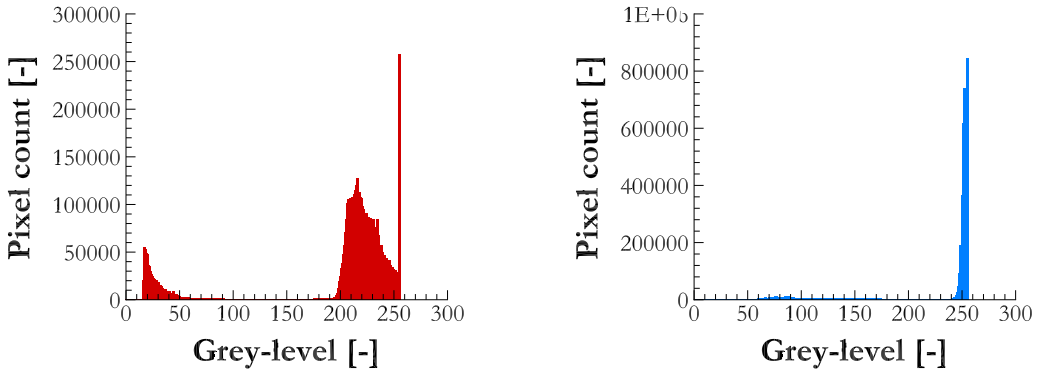

(a) Image $\bar{I}_m$

(b) After rolling ball operation $\bar{I}_m^{rb}$

Figure 3.10: Histogram of normalized images

Nevertheless, the photograph with the rolling ball algorithm offers a homogeneous background on which large structures appear more distinctive (see Figs. 3.9b and 3.10b). The image will be processed by the single-threshold method in § 3.6.2.1 for the identification of the sheet and the ligaments. To localize the droplets, on the other hand, we shall employ the wavelet-transformation technique for the normalized picture without the above treatment (§ 3.6.2.2).

3.6.2 *Localization*

Localization consists in dissociating the liquid elements to the background. Two different methods are necessary depending upon the object category. We adopt one threshold in terms of grey-level to distinguish the sheet and the ligaments as described by Grout 2009 [42]. With regard to the drop finding, the wavelet transform is demonstrated to be effective in Blaisot & Yon 2005 [4] and Fdida & Blaisot 2010 [35].

3.6.2.1 *Single-threshold method*

We apply the single-threshold recipe to the normalized images undergoing the rolling ball algorithm ($\bar{I}_m^{rb}$ in Fig. 3.9b for example). The pixels whose value is lower than the threshold l change into dark, i.e. the grey-level becomes 0. The others carrying intensities superior to the cut-off grey-level are converted into white with its value equal to 255. The threshold l is individually determined for each image by

$$l = Mode - K_b \times StdDev \tag{3.13}$$

$Mode$ stands for the most representative mode of the background, given by the principal one in the histogram (Fig. 3.10b). $StdDev$ denotes the standard deviation of the intensity distribution. Like Grout 2009 [42], the binary parameter $K_b = 2$ is chosen. Clearly, from Fig. 3.10b l is adjusted such that its value is always smaller than the minimum grey-level of the background which corresponds to the region around 250. At the same time, l is superior to the maximum intensity of the pixels constituting the objects, represented by the interval from 60 to 160. Therefore, the cut-off grey-scale l allows to discriminate between the background and the liquid elements.

The localized image $\widehat{I}_m$ of the original one I_m is displayed in Fig. 3.11a. One can see that big structures are well detected. It remains, however, several white areas in the center of the liquid film. They are the bright regions appearing on the sheet, which can be attributable to the fact that some light is transmitted through the

latter. As illustrated in Fig. 3.11b, these areas are easily deleted by the fill holes option of the software ImageJ.

(a) Image $\widehat{I}_m$ (b) After fill holes option

Figure 3.11: Localized images by single-threshold method

3.6.2.2 *Wavelet-transformation technique*

It is predicted by an imaging model in Blaisot & Yon 2005 [4] and Fdida & Blaisot 2010 [35] that when a droplet is fine or stays far from the focus plane, its image becomes blurred. Consequently, the smallest or most unfocused drops, having a poor contrast, can be lost by the classic thresholding (§ 3.6.2.1). The contrast is defined as the ratio of the luminance of the brightest pixel to that of the darkest one. A high contrast is a desired aspect of any display. To improve the detection performance, a two-stage procedure is carried out for the normalized picture (Fig. 3.12a).

Drops are localized, in the first step, by a classic thresholding. We impose for every image a cut-off grey-level I_t corresponding to the minimum contrast C_t of a droplet able to be recognized by the technique.

$$C_t = \frac{I_t - I_{min}}{I_{max} + I_{min}} \tag{3.14}$$

where I_{min} and I_{max} are the minimum and the maximum intensities of the picture, respectively. $C_t \simeq 0.5$ or $I_t \simeq 0.5\,(I_{min} + I_{max})$ is frequently recommended

to find as many objects as possible and to avoid unwanted signal. As shown in Fig. 3.12b, the contrasted elements are properly localized. Yet, for most part out-of-focus and small-size drops are lost.

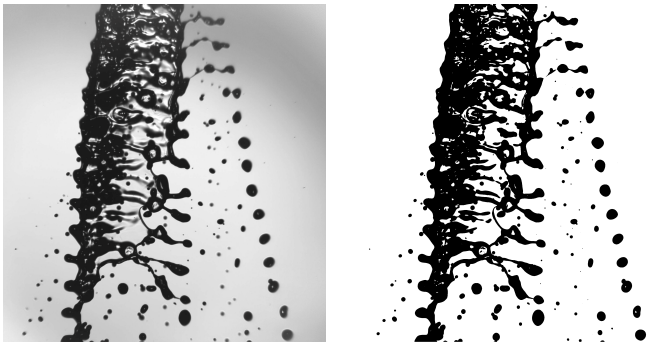

(a) Normalized image

(b) Localized image by classic thresholding

Figure 3.12: Image processing by combing classic thresholding and wavelet transform (1)

To overcome this problem, in the second step, we use the wavelet transform to determine any local grey-level variation which indicates the presence of a droplet. In effect, in the vicinity of the droplet the second derivative of the grey-scale is modified. This induces a concavity of the pixel intensity distribution which should be determined by the wavelet transform.

The wavelet transform can be seen as a spectral analysis, like the Fourier's transform, but spatially localized. The linear convolution of a normalized image I with a so-called wavelet function ψ is

$$W_{\psi,I}\left(\vec{b}, a\right) = I\left(\vec{X}\right) \otimes \psi_{\vec{b},a}\left(\vec{X}\right) \tag{3.15}$$

where $\vec{X}$ indicates a pixel position in the picture and W stands for the wavelet coefficients. ψ is defined as

$$\psi_{\vec{b},a}\left(\vec{X}\right) = \frac{1}{\sqrt{a}}\Psi\left(\frac{\vec{X} - \vec{b}}{a}\right) \qquad \text{with } a > 0 \tag{3.16}$$

Remark that ψ depends on two parameters, namely the shifting vector $\vec{b}$ which is a pointer over a pixel; and the dilatation coefficient a which adjusts the width of the function. Ψ is the mother wavelet. This is a 2D oscillating function having its mean value equal to zero.

Owing to its ability to localize the concavity of the pixel intensity in the drop outline, the Mexican hat is chosen to analyse droplet images.

$$\Psi(r) = \left(1 - r^2\right) e^{-\frac{r^2}{2}} \tag{3.17}$$

This function is the second derivative of a Gaussian function. Therefore, the convolution of a picture with the wavelet can be understood as the second derivative of the grey-level, which is firstly convoluted by a Gaussian filter. It corresponds to the part of the image where grey-scale concavity or convexity are found. Note that the higher the dilatation coefficient a is, the more spatial frequencies are eliminated by the filter and the larger the scales at which the concavities and the convexities can be observed. In order to identify the interface of a droplet, a should be set to approximate the width of the blurred area around the liquid element.

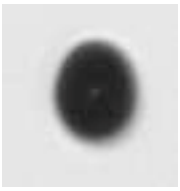

(a) Normalized picture of a drop

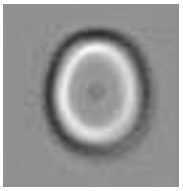

(b) Wavelet coefficient photograph

(c) Localized image by wavelet transform

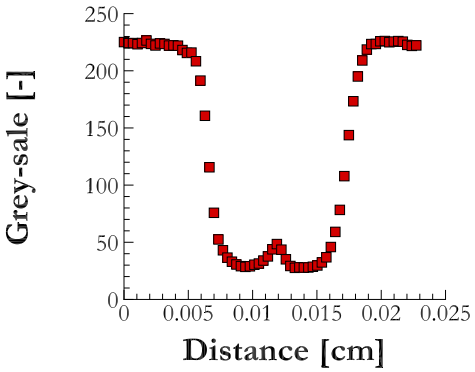

(d) Grey-level distribution along the horizontal median line of the normalized picture (Fig. 3.13a)

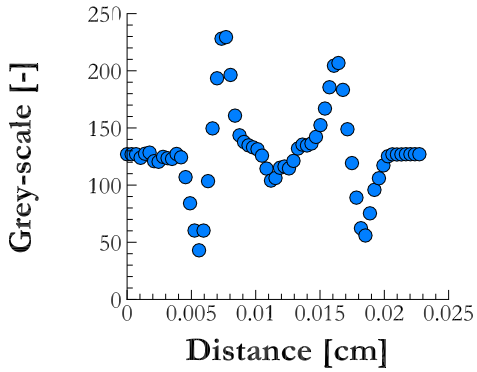

(e) Pixel intensity distribution along the horizontal median line of the wavelet coefficient photograph (Fig. 3.13b)

Figure 3.13: Drop finding by wavelet transform

Refer to Fig. 3.13 for an illustration of the technique applied to a normalized photograph of a droplet (Fig. 3.13a). A wavelet image is created, as shown in Fig. 3.13b, carrying wavelet coefficients $W\left(\overrightarrow{X}\right)$. Negative values of W correspond to pixels in a convex grey-level zone, typically the external side of the drop interface,

and positive values a concave zone or the internal side. W is equal to zero in uniform regions of the background. One should bear in mind that negative or nil values of W are encoded between 0 and I_{med}, and positive values between I_{med} and $2I_{med}$ to represent the wavelet coefficients by an image. I_{med} is the medium wavelet coefficient of the background. For the sake of clarity, Figs 3.13d and 3.13e plot the histogram along the median line of the normalized picture and that of the wavelet coefficient image, respectively. Here, the scale parameter $a = 3$ $pixels$ and the threshold $I_{wct} = 1.3I_{med}$ are applied on the wavelet picture for the drop contour detection (Fig. 3.13c).

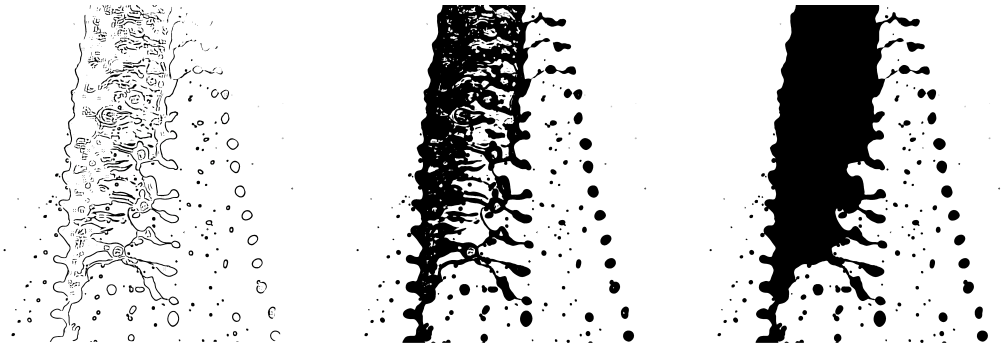

(a) Localized image by wavelet transform

(b) Union of localized images in Figs. 3.12b and 3.14a

(c) After fill holes option

Figure 3.14: Image processing by combing classic thresholding and wavelet transform (2)

We set $a = 8$ $pixels$ and $I_{wct} = 1.1I_{med}$, as commonly suggested to identify as many droplets as possible. The localized picture by the classic thresholding (Fig. 3.12b) is combined with the one processed by the wavelet transform (Fig. 3.14a). The treatment of the union image (Fig. 3.14b) is fulfilled by erasing remaining white areas thanks to the fill holes option. The final result is presented in Fig. 3.14c, where almost all droplets are satisfactorily detected despite of their small size and their out-of-focus position.

4

MULTI-SCALE ANALYSIS

As stated in chapter 2, mechanisms of the liquid-gas interface evolution occur in a wide range of time and length scales throughout the breakup of the liquid sheet. It is therefore appropriate to adopt a multi-scale analysis to investigate the atomization process.

The multi-scale tool is now applied to the disintegration of the liquid films emanating from the triple-disk injector. Below is the organization of this chapter. First, we recall the concept of the multi-scale analysis, followed by two simple illustrations. Next, an atomization scenario is proposed thanks to the observation of the back-lighted pictures of the turbulent planar liquid sheets. These images are supplied by the experiments of chapter 3. They are then processed to obtain the surface-based scale distribution, allowing us to investigate the atomization process of the entire liquid system. In particular, the dynamics of the production and breakdown of the ligament network are also analysed. It is shown that the above processes have a significant impact on the poly-dispersion of the resulting spray.

4.1.1 *Concepts*

The liquid-gas interface area continuously evolves during the atomization. As noticed by Mansour & Chigier 1991 [56], the surface-to-mass ratio is increased throughout the process. Such variation is associated with the energy exchange between the two fluids and the interface (Evers 1994 [33]). The interface creation requires energy; the reduction of interface inversely returns energy to the system. For each unit mass, the interface stores an energy which is equal to the product of the specific surface area, i.e. surface area per unit mass, and the surface tension. Furthermore, visualizations of liquid atomization reveal that mechanisms of interface evolution occur concomitantly but at different scales. The liquid flows deform in a complex way depending on a wide range of time and length scales, as quoted in chapter 2. Dumouchel et al. 2015 [26], while temporally pursuing an atomizing liquid ligament, remark that the contraction of the ligament into swells is accompanied by a local reduction of the specific surface area; whereas its elongation into threads locally increases the specific surface area (Fig. 4.1). Given these complex characteristics of the interface evolution, a multi-scale approach involving the specific surface area seems to be appropriate to investigate the atomization process.

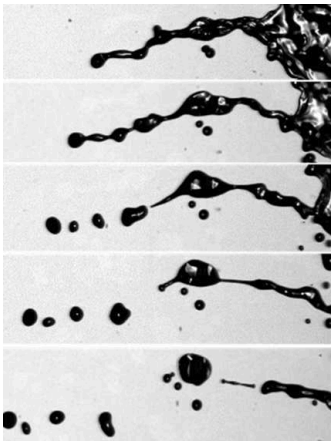

Figure 4.1: Atomizing ligaments (Dumouchel et al. 2015 [26])

One candidate method, with the notion of the surface-based scale distribution, is introduced by Dumouchel et al. 2008 [21]. The distribution is obtained by per-

forming the Euclidean Distance Mapping (EDM) method on 2D images. In the resulting pictures, each liquid pixel contains its distance to the nearest gas pixel. The EDM method is used to determine the fractal dimension of a contour (Bérubé & Jébrak 1999 [3] for instance). It is emphasized in Dumouchel et al. 2015 [25] that since only 2D projection of the liquid system is taken into account, the scale distribution is rather the specific length observed over the entire scale space. The specific length is the contour length of the projection of the system over the surface area of the latter.

Below is a brief summary of the formulation of the surface-based scale distribution. In Fig. 4.2a, let's consider a 2D system having a total surface area of S_T. It is eroded by a circle of diameter d. The erosion procedure is illustrated in Fig. 4.2, starting as Fig. 4.2b to end at Fig. 4.2c. The area of the resulting eroded system (the grey part in Fig. 4.2c) is denoted by $S(d)$. The diameter d of the erosion circle is known as the scale of observation.

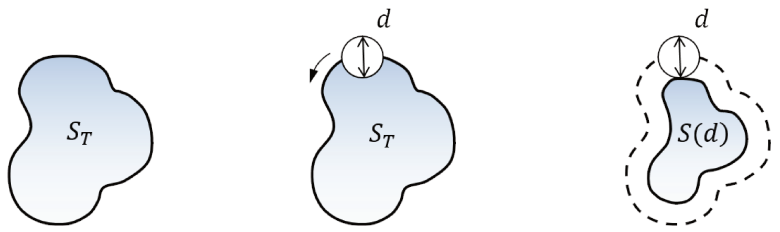

(a) Initial system (b) Start of erosion (c) End of erosion

Figure 4.2: Erosion procedure

The cumulative surface-based scale distribution is a function of d and is given by:

$$E_2(d) = \frac{S_T - S(d)}{S_T} \tag{4.1}$$

Remark that $E_2(0) = 0$ since $S(0) = S_T$. When d reaches a critical value d_{max} specific to each system, the object is entirely erased by the erosion procedure. Thus, $S(d \geqslant d_{max}) = 0$ and $E_2(d \geqslant d_{max}) = 1$. Moreover, $E_2(d)$ increases monotonously from 0 to 1.

The first derivative of $E_2(d)$ is the surface-based scale distribution:

$$e_2(d) = \frac{dE_2(d)}{dd} \tag{4.2}$$

To clarify how $e_2(d)$ can describe the system, we examine in Fig. 4.3 two successive erosions at scales d and $d + \Delta d$. (4.2) can be developed as

$$\begin{aligned} e_2(d) &= \frac{dE_2(d)}{dd} = \lim_{\Delta d \to 0} \frac{E_2(d+\Delta d) - E_2(d)}{\Delta d} \\ &= \lim_{\Delta d \to 0} \frac{(S_T - S(d+\Delta d))/S_T - (S_T - S(d))/S_T}{\Delta d} \\ &= \lim_{\Delta d \to 0} \frac{S(d) - S(d+\Delta d)}{S_T \times \Delta d} = \lim_{\Delta d \to 0} \frac{P(d) \times \Delta d/2}{S_T \times \Delta d} = \frac{P(d)}{2S_T} \\ &= \frac{\text{Perimeter of the eroded system at scale } d}{2 \times \text{Total surface of the system}} \end{aligned} \tag{4.3}$$

where $P(d)$ is the perimeter of the eroded system at scale d. Equation (4.3) indicates that the surface-based scale distribution is the ratio between the perimeter of the eroded system at a certain scale and twice the total surface area of the initial system. In consequence, $e_2(d)$ is the specific length of the 2D system observed at scale d. Notice that when $d = 0$, it is similar to the concept of the specific surface in 3D (Evers 1994 [33]).

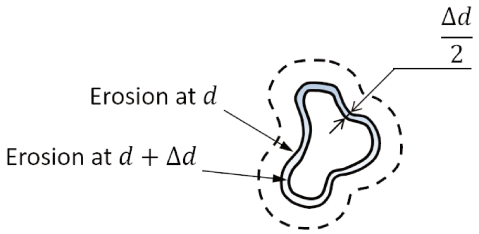

Figure 4.3: Two successive erosions at scales d and $d + \Delta d$

For illustration purpose, consider two simple objects. The first one is a circle of diameter D (Fig. 4.4a). The second one is a rectangle of width W (Fig. 4.4b). Indeed, we suppose here that the rectangle interface is represented only by its two longest sides where the erosion procedure is carried out.

It can be demonstrated that the scale distribution of the circle is linear, expressed by:

$$e_2(d) = \begin{cases} -\frac{2}{D^2}d + \frac{2}{D} & \text{if } d \leqslant D \\ 0 & \text{otherwise} \end{cases} \tag{4.4}$$

The circle's scale distribution is a straight line (Fig. 4.5a). It can be seen that the slope of the line is independent of d and is equal to $-2/D^2$.

(a) A circle (b) A rectangle

Figure 4.4: Simple objects

When it turns to the rectangle, the scale distribution is the following step-function.

$$e_2(d) = \begin{cases} \frac{1}{W} & \text{if } d \leqslant W \\ 0 & \text{otherwise} \end{cases} \tag{4.5}$$

This function is plotted against the scale in Fig. 4.5b where its value takes an abrupt downturn at a scale equal to the rectangle width W.

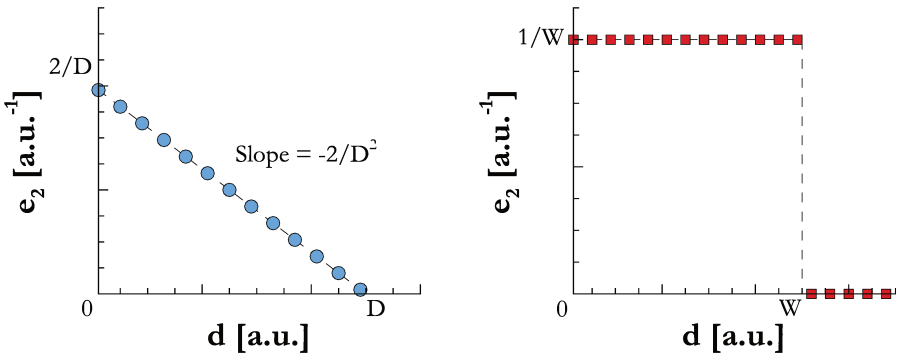

(a) A circle (b) A rectangle

Figure 4.5: Scale distribution of simple objects

The above examples clearly indicate that the scale distributions of a circle differs from that of a cylinder. Consequently, objects encountered in atomization like droplets and ligaments having their projections similar to these two basic geometries can be distinguishable via their respective surface-based scale distributions.

Three successive applications are conducted by Dumouchel and his colleagues [23–25] who make use of the scale entropy diffusion model to describe how the liquid system evolves over time. The flow is recognized as a multi-scale object. Its

shape can be represented by the scale distribution which is in turn linked to the scale entropy function. Initially, Queiros-Conde 2003 [77] and Queiros-Conde et al. 2008 [76] develop the model for turbulent interface study.

Individual atomizing ligaments which appear at the sheet borders are investigated in Dumouchel et al. 2015 [26]. The back-lighting high speed film of the liquid sheet ejected from a triple-disk injector are recorded by Ngô 2013 [64]. Based on the scale distribution's time course, the ligaments are found to experience elongation and capillary deformation at their creation. Determined by the reminiscence of the sheet dynamics, the initial elongation may be weak or strong, which will affect the whole subsequent rupture of the filaments. The authors introduce, for the liquid threads, a Weber number which is the ratio between two characteristic times representing respectively the capillary instability and the elongation. They detect a critical Weber number We_c based on which two ligament categories can be identified. For a Weber number inferior to We_c, the effects of initial elongation is limited and no secondary ligaments are produced. Their subsequent decay involves mainly the capillary mechanism and drops of equivalent size are formed. In contrast, for a Weber number higher than We_c, the initial elongation favours the development of stretched secondary ligaments. Their breakdown results in a coarser drop size-distribution and numerous fine droplets. In this regard, it is interesting to look at the experiments of Marmottant & Villermaux 2004 [58] which deal with the fragmentation of a stretched ligament formed by the withdrawal of a tube initially dipping at a free surface. Two concurrent phenomena, i.e. capillary breakup and elongation, are examined by their respective characteristic times. The authors consider two limit cases where only one small droplet is produced with a slowly stretched bridge; and a set of droplets with distributed sizes is obtained from the breakup of the ligament submitted to a fast extension. It seems that the elongation is useful to the atomization since it delays the capillary breakup, causing larger drop-size distribution and enhancing the production of small droplets.

Also examining the capillary instability of a liquid cylindrical column but a recent paper by Dumouchel et al. 2017 [27] is based on simulation results rather than experimental ones. The authors apply several wave-numbers of initial perturbations on the interface, and measure a 3D scale distribution. Two specific scales are computed. The small one d_1 is defined as in Dumouchel et al. 2015 [25] while the large one d_{max} is the system's maximum scale, as introduced above. Whereas the large scale follows the Rayleigh linear theory, the small one exhibits three dy-

namic regimes. The succession of these regimes is related to the non-linear effects, in agreement with the literature. It is highlighted that the duration of the last two regimes is reduced as the wave-number increases. Furthermore, the discrepancy of d_1 growth rate in the first regime with the linear theory appears to be in proportion to the subsequent non-linear effects. The latter are hence detected in the small scale region since the beginning of the process.

Figure 4.6 shows a liquid ligament which experiences a pure stretching. Its deformation can be schematized by an ideal cylinder whose geometry varies in time (Dumouchel 2017 [20]). The ligament is elongated by an external constraint and its volume is kept constant. Its diameter $D(t)$ diminishes in time and its scale distributions $e_2(d,t)$ calculated from (4.5) are successive step-functions. The pulling of the liquid filament causes its length $L(t)$ to grow and its diameter $D(t)$ to decrease at the same time. For simplicity, the comparison of these two geometrical properties can be made between two instants t_1 and t_2, showing the temporal evolution of the ligament's size (Fig. 4.6).

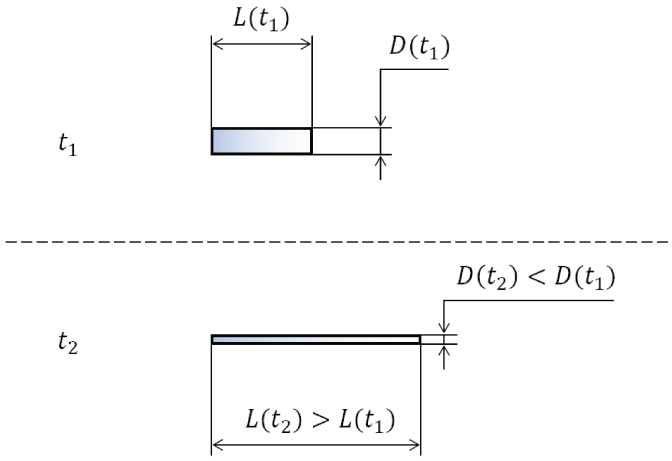

Figure 4.6: Thinning of a stretched cylindrical ligament

Similar to Marmottant & Villermaux 2004 [58], the elongation rate of the cylindrical ligament is defined by:

$$\dot{\epsilon} = \frac{1}{L(t)} \frac{\partial L(t)}{\partial t} \equiv \frac{\dot{L}(t)}{L(t)} \tag{4.6}$$

Thanks to the volume conservation

$$L(t) \times \frac{\pi}{4} D^2(t) = constant \tag{4.7}$$

one gets

$$\dot{L}(t)\, D^2(t) + 2D(t)\, \dot{D}(t)\, L(t) = 0 \quad \text{and} \quad \frac{\dot{L}(t)}{L(t)} = -\frac{2\,\dot{D}(t)}{D(t)} \tag{4.8}$$

In addition, considering that the liquid-gas interface is composed of its two horizontal edges solely, we can compute the specific length of the liquid thread which is identical to that of the scale distribution of the rectangle (4.5).

$$e_2(d,t) = \frac{1}{D(t)} \quad \text{or} \quad e_2(d,t)\, D(t) = 1 \tag{4.9}$$

Calculating the temporal derivative of both sides in (4.9) to obtain

$$D(t)\, \dot{e}_2(d,t) + e_2(d,t)\, \dot{D}(t) = 0 \quad \text{and} \quad \frac{\dot{D}(t)}{D(t)} = -\frac{\dot{e}_2(d,t)}{e_2(d,t)} \tag{4.10}$$

Remark from (4.10) that for a rectangle, the variation rate of the scale distribution $\frac{\dot{e}_2(d,t)}{e_2(d,t)}$ is independent of scale d at every instant t.

The (4.11) relationship below results from the combination of (4.10) and (4.8). It indicates how the elongation rate of the ligament's perimeter, defined as $P(t) = 2L(t)$ is linked to the variation rate of its specific length during the thinning of a liquid thread.

$$\frac{\dot{P}(t)}{P(t)} = 2\frac{\dot{e}_2(0,t)}{e_2(0,t)} \qquad \text{and} \qquad \dot{e}_2(0,t) > 0 \tag{4.11}$$

(4.11) indicates that the specific length $e_2(0,t)$ increases in time since its temporal derivative $\dot{e}_2(0,t)$ is positive. Thanks to (4.9), this is equivalent to a reduction of the cylinder diameter or a thinning of the liquid ligament.

However, the thinning of a liquid thread is not caused systematically by the pure stretching. Other mechanisms such as the capillary contraction can also provoke a reduction of the ligament diameter or a growth of its specific length. This mechanism is driven by the surface tension forces which expel the liquid out of a liquid bridge (Fig. 4.7). The volume of the latter decreases, unlike during the pure stretching described in the previous paragraphs. In this case, the reduction of the

ligament diameter is not compensated by the increase of its circumference, leading to the inequality below:

$$\frac{\dot{P}(t)}{P(t)} < 2\frac{\dot{e}_2(0,t)}{e_2(0,t)} \qquad \text{and} \qquad \dot{e}_2(0,t) > 0 \tag{4.12}$$

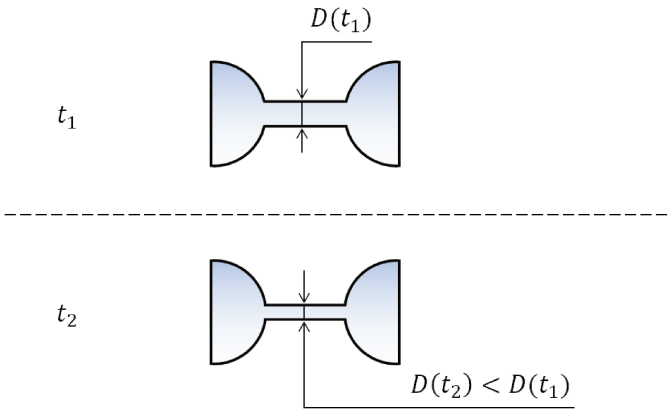

Figure 4.7: Capillary contraction of a ligament

A liquid filament can expands in length while remains unchanged in diameter, keeping a constant specific length. This situation can occur, for example, during the production of a ligament, as shown in Fig. 4.8. The following formulae are thus verified.

$$\frac{\dot{P}(t)}{P(t)} > 2\frac{\dot{e}_2(0,t)}{e_2(0,t)} \qquad \text{and} \qquad \dot{e}_2(0,t) = 0 \tag{4.13}$$

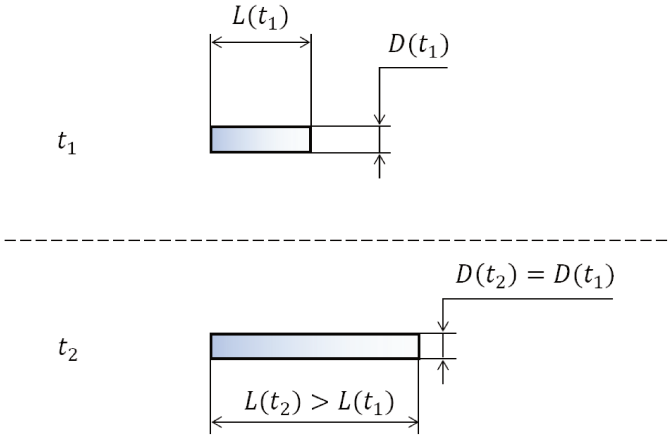

Figure 4.8: Production of a cylindrical ligament

So as to examine the deformation of the liquid system, in § 4.3.1 the above relationships between the variation rates of the perimeter and specific length are applied, aiming to identify the corresponding mechanisms. A technique is then

employed to isolate the ligament network from the bulk of the sheet before using these relationships exclusively on the liquid threads in § 4.3.2. This allows us to study the formation of these ligaments and their rupture into droplets. It is found that these processes play an important role on the drop-size distribution of the resultant spray.

4.1.2 *Measurements*

The temporal multi-scale description of the atomization of the liquid sheets produced by the triple-disk injector are performed in two steps.

First, the EDM operator is applied for 150 binary images converted from the grey-scale snapshots in positions "up" and 150 others from the pictures "down" (Figs. 3.6 and 3.7). We thus obtain the corresponding euclidean distance maps which indicate for each pixel in the liquid objects of the original binary picture the distance to the nearest pixel in the background or to the liquid-gas interface (Figs. 4.9a and 4.9b). In deed, the pixels in the center of the liquid film are dark because they stay far from the interface whereas those near the sheet border are attributed with bright colours.

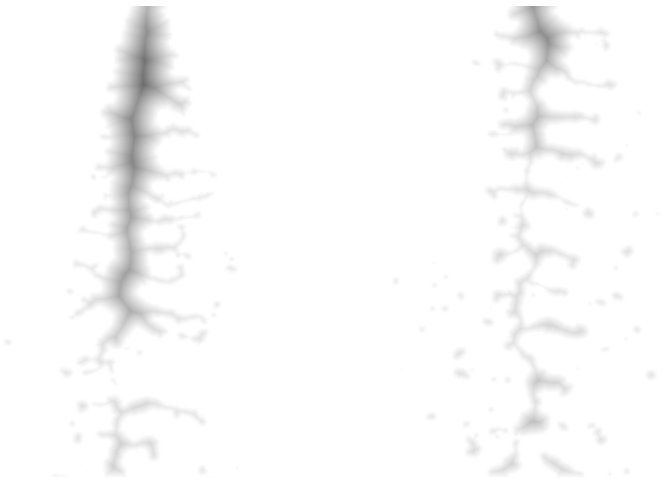

(a) Position "up" (b) Position "down"

Figure 4.9: EDM images of the water sheets

Second, to temporally follow the breakup process, one needs to measure the local cumulative surface-based scale distribution. To this end, the total surface area and the surface area of the eroded systems are necessary in a limited space (4.1). We

thus use, on each euclidean distance picture, a rectangular analysing window in which a measurement is proceeded to have the total surface area and the surface area of the eroded systems. To obtain a temporal description of the atomization process, the window is slid on each euclidean distance map from the top down (Fig. 4.10). For every window position, the position z_i of its horizontal median line is divided by the metering velocity V_q (Tab. 3.2) giving an equivalent time t_i.

$$t_i = \frac{z_i}{V_q} \tag{4.14}$$

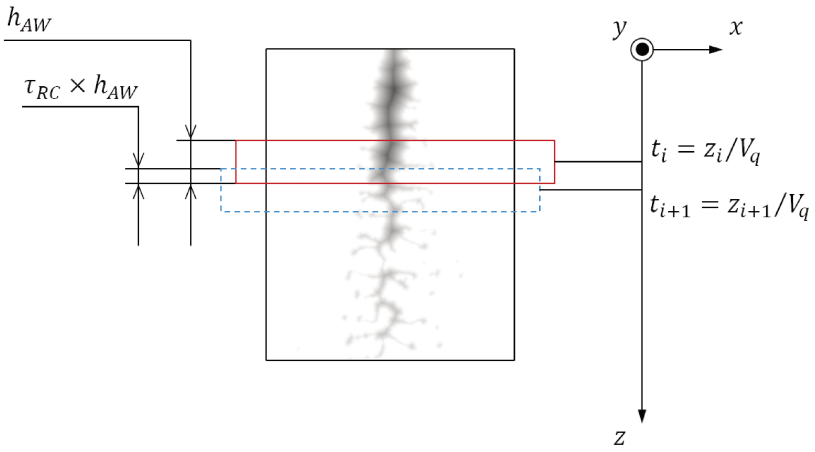

Figure 4.10: Analysing window

We then count, for each EDM image m and for each window location $z_i = V_q \times t_i$, the number $n(m, d, t)$ of the pixels whose distances to the liquid-gas interface are inferior to a scale d. Clearly, $n(m, d, t)$ is proportional to the surface of the eroded surface area of the object (the white part in Fig. 4.2c) and $n(m, \infty, t)$ the total number of the liquid pixels. Consequently, the local cumulative surface-based scale distribution (4.1) can be calculated as

$$E_2(m, d, t) = \frac{n(m, d, t)}{n(m, \infty, t)} \tag{4.15}$$

allowing to derive the average local cumulative scale distribution from

$$E_2(d, t) = \frac{\sum_{m=1}^{N} E_2(m, d, t)}{N} \tag{4.16}$$

where $N = 150$ is the total number of the images.

The local surface-based scale distribution $e_2(d,t)$ is derived as in (4.2) by a central difference.

$$e_2(d,t) = \frac{E_2(d+\Delta d,t) - E_2(d-\Delta d,t)}{2\Delta d} \tag{4.17}$$

Two preliminary tests are carried out, examining the height of the analysing window and the necessary number of images to guarantee a good statistical description of the atomization process under consideration.

The first test aims to justify the choice of the analysing window height h_{AW} (Fig. 4.10). We begin by fixing its center at position $z = 3497$ µm in the images at position "up" and "down". Then, three rectangular windows of different heights are considered. The testing values are 100, 200 and 300 pixel. We measure three cumulative scale distributions for Fo which correspond to these three values. Figures 4.11a and 4.11b show the results for the images at position "up" and "down", respectively. Apparently, the three curves representing the cumulative scale distributions corresponding to the three window heights overlay one over another. h_{AW} has therefore negligible impact on the cumulative scale distribution. Like Grout et al. 2007 [43], we adopt $h_{AW} = 200$ pixel since the authors investigate similar liquid sheets ejected from a triple-disk injector with an analogous optical arrangement and the spatial resolution of the images obtained in this study is close to those in our configuration.

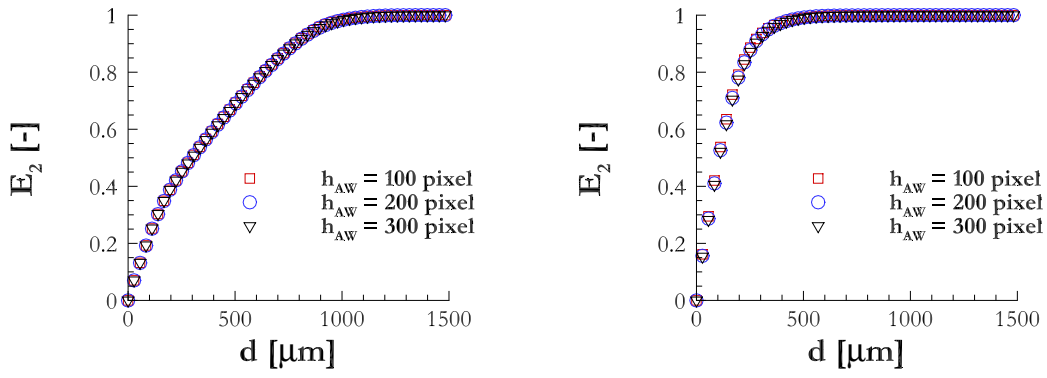

(a) Images in position "up"

(b) Images in position "down"

Figure 4.11: Testing the analysing window height

Moreover, a high recovery rate $\tau_{RC} = 0.75$ is applied in our study in order to attain a smooth temporal description of the atomization process. Concretely, the

analysing windows corresponding to t_i is recovered by the subsequent one t_{i+1} (Fig. 4.10). The lower part the window t_i representing 75 % of its surface area is covered by the adjacent t_{i+1}.

In the second test, the number of images necessary to obtain a sufficient statistic is examined. To this end, we use the pictures at position "up" for Fo, on which we place an analysing window at position $z = 3497$ µm , as in the previous test. Four cumulative scale distributions are measured, corresponding to different numbers of snapshots used which are 10, 50, 100 and 150. Figure 4.12a displays these cumulative scale distributions. It seems that the results are not very sensitive to the number of images. However, at the small scale range from 200 to 400 µm, the cumulative scale distribution converges from 100 images (Fig. 4.12b). This justifies that for each fluid and for each position "up" or "down", 150 images available from our experiments guarantee good statistical description of the breakup of the liquid sheet.

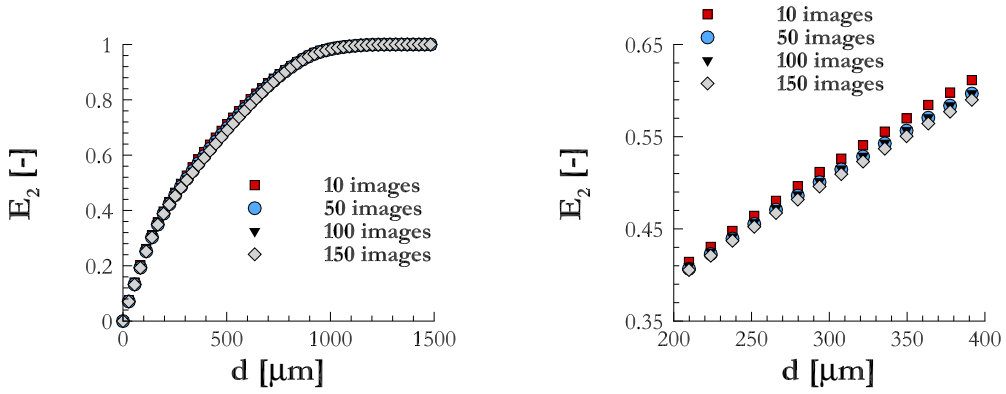

(a) Cumulative scale distribution

(b) Cumulative scale distribution - Zoom on the scale range from 200 to 400 µm

Figure 4.12: Testing the number of images

The scale distributions $e_2(d,t)$ for Fo over all the scale space at several instants are shown in Fig. 4.13a. In particular, in the small scale range, the scale distribution oscillates when d is smaller than 50 µm and becomes too high when $d = 0$ (Fig. 4.13b). The fact that the surface-based scale distribution increases with d is clearly non-physical. It is probably due to the fact that an image is constituted from square pixels. While approaching the liquid-gas interface, the latter can not be finely described by these pixels which contain the distance to the interface. To correct this behaviour of $e_2(d,t)$ near $d = 0$, one can make use of the quasi-

linearity of the scale distribution in the adjacent region. In effect, the values of $e_2(d,t)$ at the small scales are reconstituted by a linear extrapolation from those at larger neighbouring scales (Fig. 4.13c).

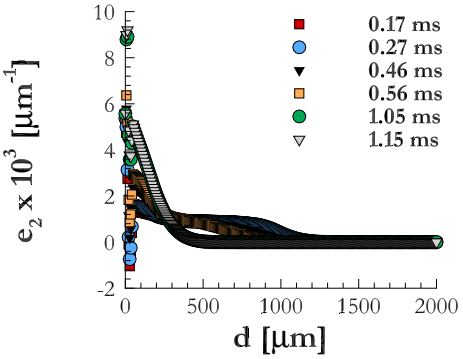

(a) Scale distribution before the correction

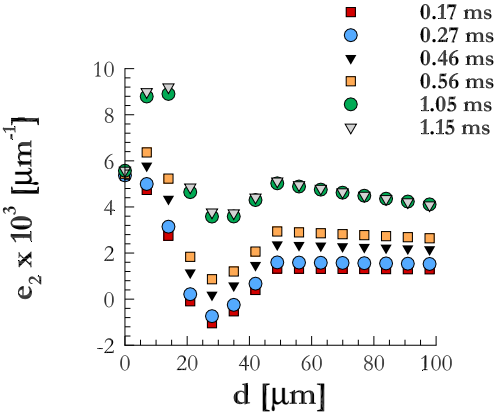

(b) Before the correction - Zoom on the small scale region

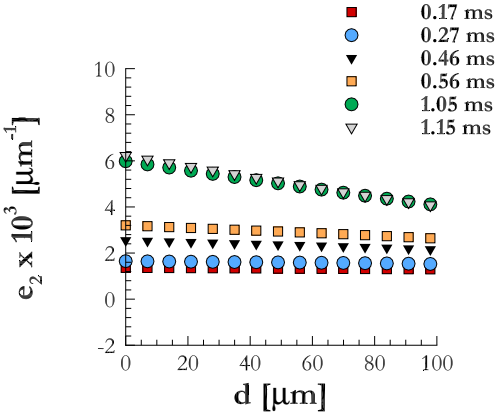

(c) After the correction - Zoom on the small scale region

Figure 4.13: Extrapolation of the scale distribution at small scales

4.2 DESCRIPTION OF THE IMAGES

The back-lighted images collected from the experiments in chapter 3 serve as input of the multi-scale analysis to inspect the atomization process. Before this task can be done, observation of these images is indispensable. We thus start by a description of the back-lighted images, resulting in a breakup scenario proposed at the end of this section. Essential features of the disintegration of the planar turbulent liquid sheets are summarized in the scenario.

To enhance the representativeness of the description and facilitate the distinction between different fluids based on their characteristics, only F0 and F10 are presented here. Figures 4.14 and 4.15 exhibit some snapshots of F0 at two positions "up" and "down", respectively. Images for the liquid F10 are shown in Figs. 4.16 and 4.17.

The two mixtures F0 and F10 share a significant common property in their atomization process. In both cases, the liquid system consists of three principal elements: (i) A large centre part surrounded by (ii) a ligament network and (iii) numerous droplets. The center part which represents the bulk of the sheet increases in size to reach a maximum width, then contracts until the end of the process. On both sides of the sheet, one can see the ligaments develop on the borders. The birth of several disturbances and their growth, together with the contraction of the liquid film, especially between two perturbation extremities might be the origin of the ligament formation. The breakup of the ligaments then produces droplets, which are the last element of the system. Almost all drops are in-focused, which points out that the liquid sheet is rather 2D, locating in the plane of symmetry of the injector as the ligaments produced on its edges. One should bear in mind that the double-counter swirl stretches the flow to form a 2D sheet with turbulence-induced disturbances on its edges (see Dumouchel et al. 2005 [22]).

However, marked differences could be found in the sheet breakup of these two fluids. First, the opening angle of the liquid film is larger for F10 than for F0. Since the mass flow rate is kept constant for two fluids, one could expect that the F10 sheet is thinner, reducing the diameter of the liquid ligaments. It is clear that the ligaments' extremities for F10 are aligned with the initial opening angle whereas those for F0 are not. Moreover, the ligaments existing on the sheet borders of F10 are more equitably distanced, making possible a single oscillating frequency of the whole liquid system. Such a behaviour is not found for F0. In addition, the F10 filaments are long and much deformed whereas those of F0 are smooth and more numerous.

More importantly, these snapshots show that the liquid system of F0 is not as reproducible as that of F10. This can be explained by a consistent turbulence level for the mixture F0. Notice that the Reynolds number of F0 is higher than that of F10 (Tab. 3.2). Finally, the F0 drops are not numerous but homogeneous in size whereas many fine droplets are formed for F10, with larger drop-size distribution.

Provided with these distinctions, it appears that the formation of the ligaments F10 is due to the capillary instability, explaining their regularity in space. Meanwhile, the turbulence has a great impact on the ligament production for the liquid F0 because they are irregular in size from one image to another. Notice that the Reynolds number for F0 is much higher than that for F10 (Tab. 3.2).

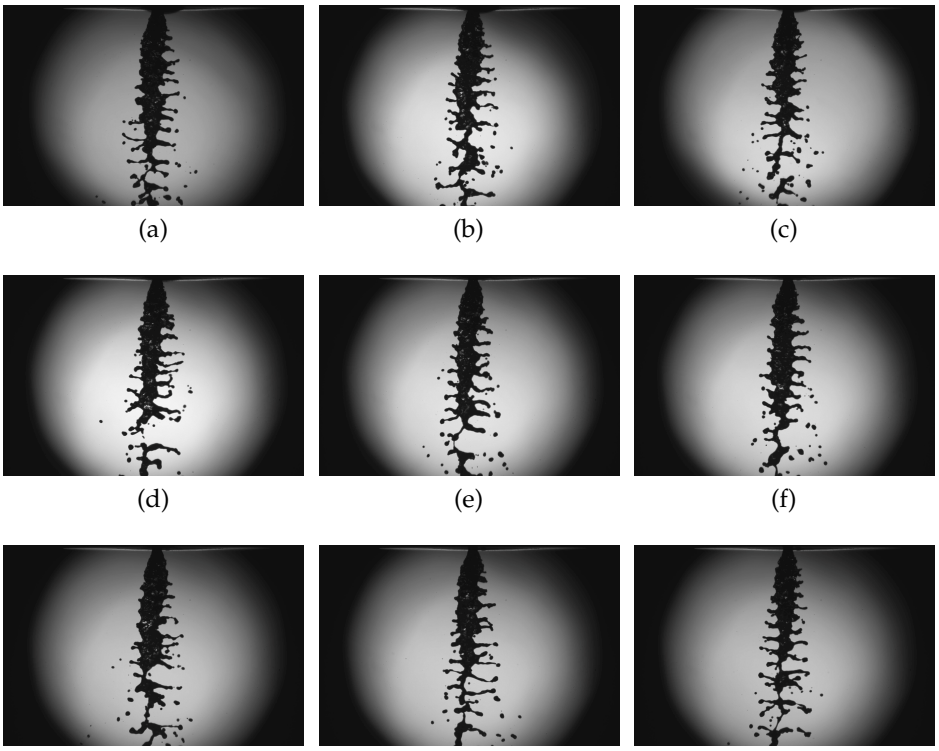

(a) (b) (c)

(d) (e) (f)

(g) (h) (i)

Figure 4.14: Snapshots of the liquid sheets Fo - Postion "up"

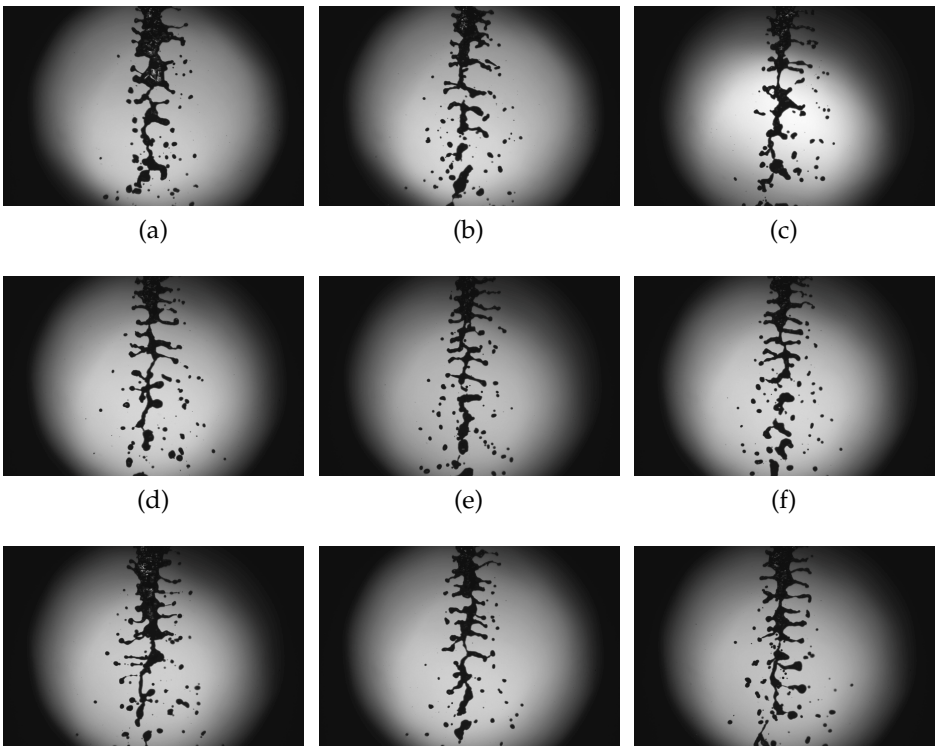

(a) (b) (c)

(d) (e) (f)

(g) (h) (i)

Figure 4.15: Snapshots of the liquid sheets Fo - Postion "down"

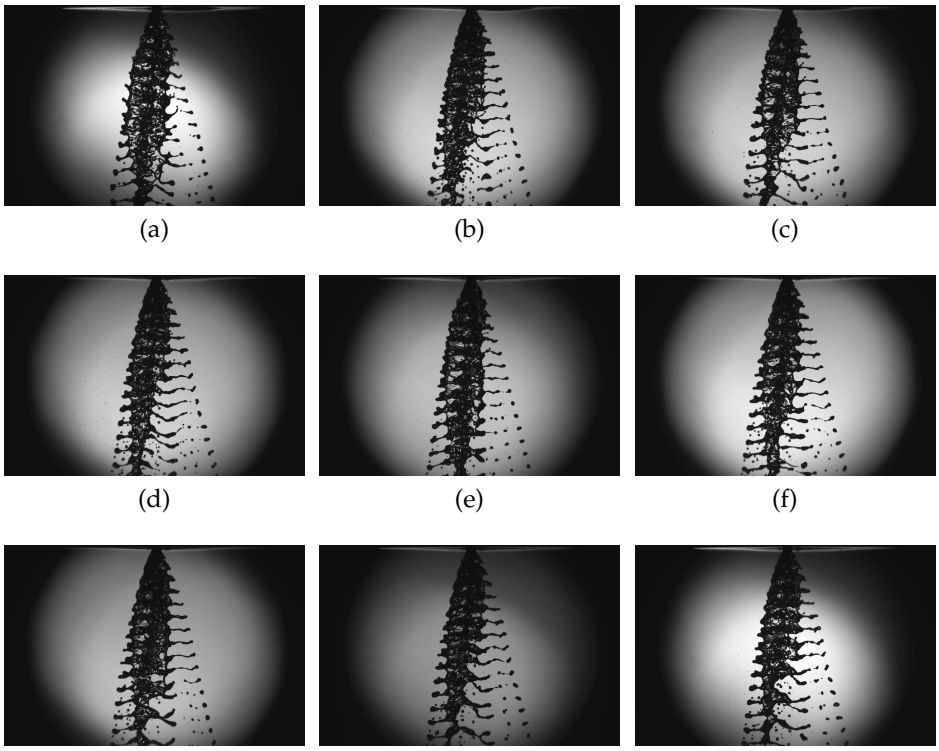

(a) (b) (c)

(d) (e) (f)

(g) (h) (i)

Figure 4.16: Snapshots of the liquid sheets F10 - Postion "up"

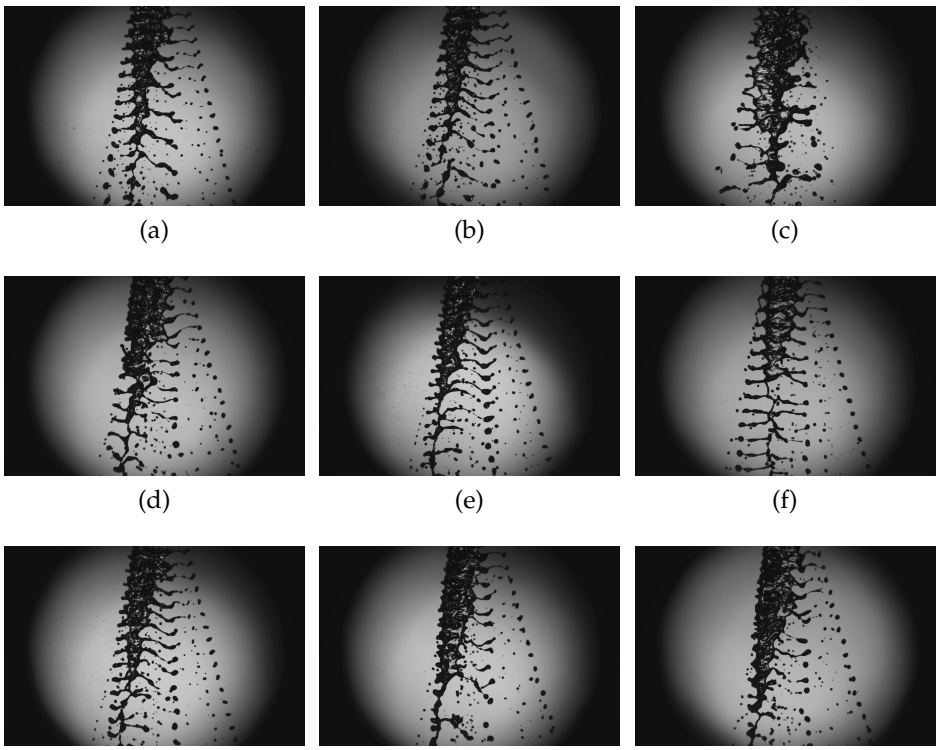

(a) (b) (c)

(d) (e) (f)

(g) (h) (i)

Figure 4.17: Snapshots of the liquid sheets F10 - Postion "down"

Based on all the observations above, we come up with the following atomization scenarios of the turbulent liquid sheet issuing from the triple-disk injector. On the borders of the liquid film, the turbulence initiates the development of the perturbations. The latter grow to form a ligament network which then breaks down into droplets. As shown in Brémond & Villermaux 2006 [6], the development of the disturbances has a great impact on the behaviour of the liquid film. The extremities of the perturbations and the ligaments tend to preserve continuously their straight trajectory fixed by the initial opening angle of the liquid sheet. The fluid F10 can be found in this configuration (Fig. 4.18b). Alternatively, the extremities of the liquid ligaments are not aligned with the sheet opening angle, resulting in another breakup scenario (Fig. 4.18a) which is more suitable for F0.

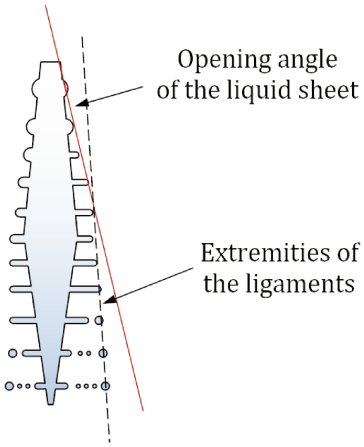

(a) F0

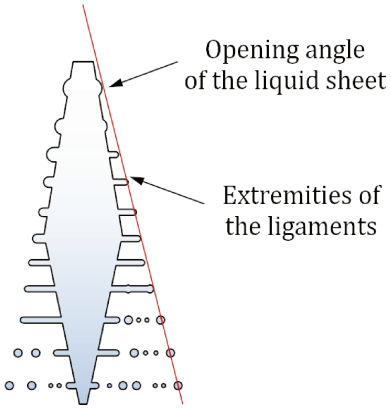

(b) F10

Figure 4.18: Two atomization scenarios

4.3.1 *Entire liquid system*

4.3.1.1 *General remarks*

Figures 4.19 and 4.20 depict the cumulative surface-based scale distributions for two liquids Fo and F10, respectively. $E_2(d,t)$ are plotted as a function of the scale d. Each curve corresponds to a time or a position of the analysing window (refer to Fig. 4.10).

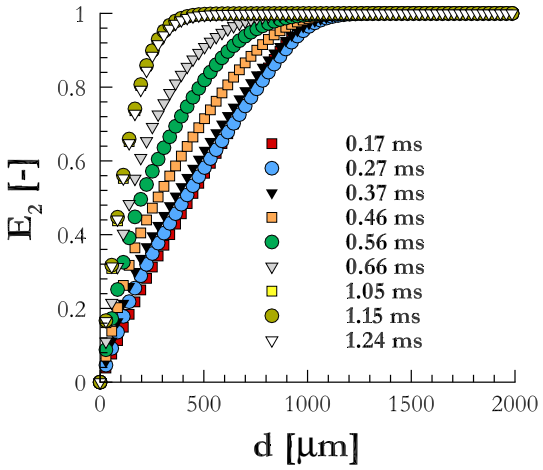

Figure 4.19: Cumulative surface-based scale distribution for Fo

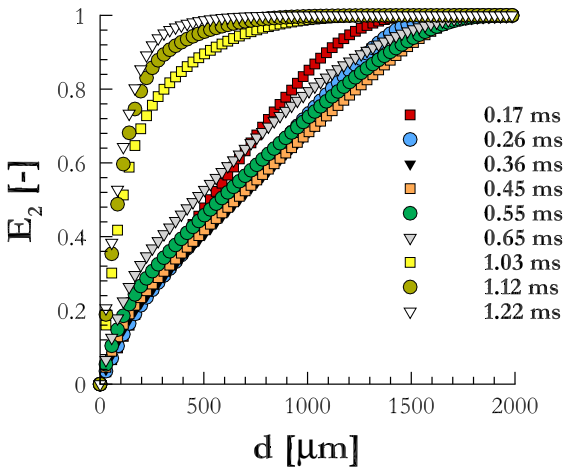

Figure 4.20: Cumulative surface-based scale distribution for F10

Remark that all curves increase with d from zero until reaching unity from the scale d_{max}, as explained in the paragraph after (4.1). These functions are proven to be the cumulative scale distributions. The scale range covered by $E_2(d,t)$ depends on liquid and time. The cumulative scale distributions of two fluids differ one from another, having distinct form even at two close instants. Seemingly, the chosen times do not correspond to equivalent phases of Fo and F10 liquid systems.

We now turn to the surface-based scale distributions, presented in Figs. 4.21 and 4.22 for Fo and F10, respectively. $e_2(d,t)$ are drawn over the scale-space, with each curve corresponding to an instant.

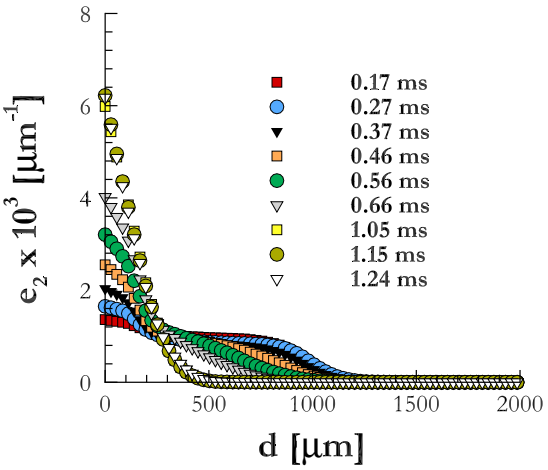

Figure 4.21: Surface-based scale distribution for Fo

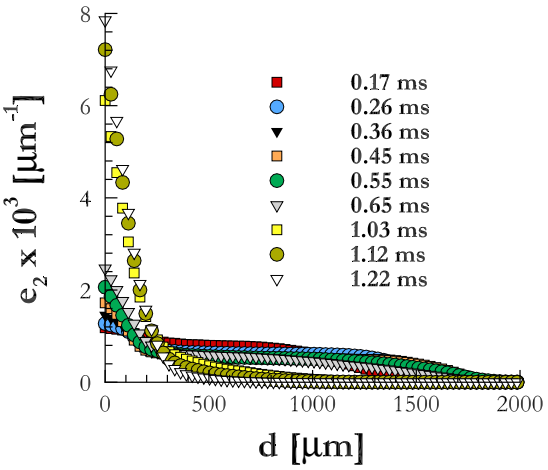

Figure 4.22: Surface-based scale distribution for F10

The scale distributions diminish as the scale increases. It is equal to zero beyond the scale d_{max}. Clearly, when $d \geqslant d_{max}$, the cumulative scale distribution becomes unity and its derivative $e_2(d,t)$ is thus unvaryingly equal to zero.

$e_2(d,t)$, at early instants, resembles to a step function over an intermediate range (around 600 μm for Fo and 1000 μm for F10). Notice that a cylinder has similar scale distribution (Fig. 4.5b). This demonstrates that the form of the projection of our liquid system at such moments is close to a rectangle. However, $e_2(d,t)$ behaves differently at small scales, indicating non-negligible influence of the perturbations appearing on the sheet borders (refer to § 4.2). Additionally, at large scales, $e_2(d,t)$ is not a step function any more. Indeed, its variation from a stable value over the intermediate scale range to zero is not abrupt but rather gradual, signifying that the geometry of the liquid system is not a perfect rectangle. Towards the end of the process, the scale distribution decreases rapidly with d. Its non-nil values cover a scale interval much smaller than at early instants.

By comparing the two fluids, one can notice that d_{max} for F10 is higher than that of Fo at early moments when the scale distribution is close to a step function. The above observation is also true for the maximum value of $e_2(d,t)$ at late instants. Since $e_2(d,t)$ represents the contour length per unit surface, one could expect a better atomization efficiency when the liquid F10 is used rather than Fo.

The snapshot-to-snapshot fluctuations of $E_2(d,t)$ provide useful information about the behaviour of the liquid system, especially at the beginning of its breakup. Such fluctuations could be quantified by the root-mean-square-deviation of the cumulative scale distribution as follow

$$rmsdE_2(d,t) = \sqrt{\frac{\sum_{m=1}^{N} \left(E_2(m,d,t) - E_2(d,t)\right)^2}{N}} \tag{4.18}$$

$rmsdE_2(d,t)$ for Fo and F10 are respectively depicted in Figs. 4.23 and 4.24. Notice that the fluctuations of $E_2(d,t)$ for the liquid F10 is lower than that of Fo. For Fo, the fluctuations of $E_2(d,t)$ grow in time over all scales. Contrarily, they increase at first instants for F10, then decrease before staying still from 0.24 ms. These clear dissemblances between the two fluids point out that the evolution of their respective liquid systems are driven by different mechanisms. This is in agreement with the observations in § 4.2, the capillary instability plays an essential role in

the breakup process for the liquid F10 whereas Fo is influenced mainly by the turbulence.

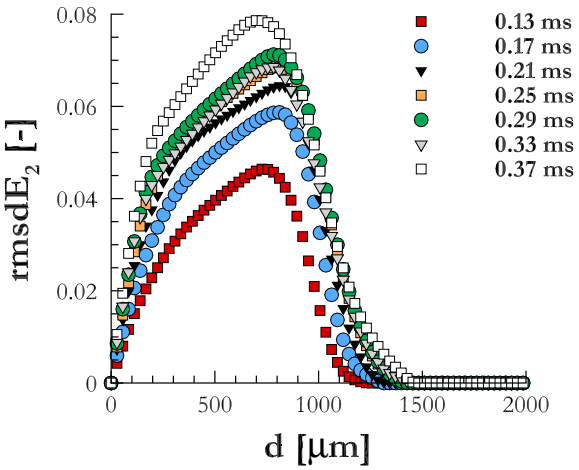

Figure 4.23: Snapshot-to-snapshot fluctuations of the cumulative scale distribution for Fo

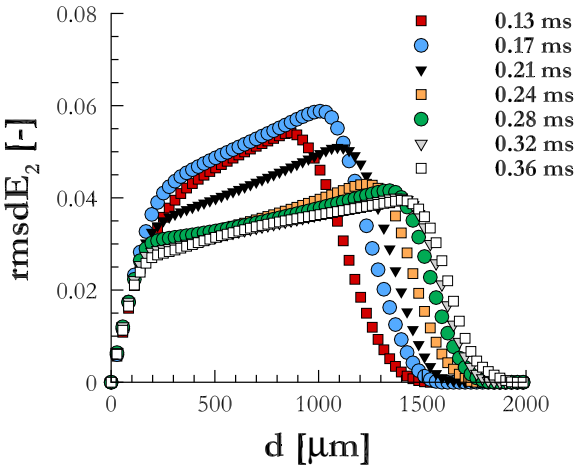

Figure 4.24: Snapshot-to-snapshot fluctuations of the cumulative scale distribution for F10

4.3.1.2 *Evolution of the maximum scale*

The maximum scale $d_{max}(t)$ represents the large liquid structure. In practice, we determine $d_{max}(t)$ as the scale from which the cumulative scale distribution $E_2(d,t)$ attains 0.99. This threshold is chosen to ensure a good statistical description of the process. It is different to unity to avoid a too important weight of the unique event $E_2(d,t) = 1$ requiring all instantaneous cumulative scale distributions $E_2(m,d,t)$ to be equal to one (refer to (4.16)). Figure 4.25 draws its temporal evolution for six fluids.

$d_{max}(t)$ increases at early moments. This indicates that the sheet spreads as soon as the liquid flow is ejected from the nozzle and becomes free of any parietal constraint. The scale d_{max} reaches a maximum value and remains nearly constant within a short duration. Then, the liquid film contracts allowing d_{max} to decrease rapidly. The maximum scale becomes unvarying at the end of the process. This constant value is the average size of biggest elements created at the end of the process or the width of the sheet base.

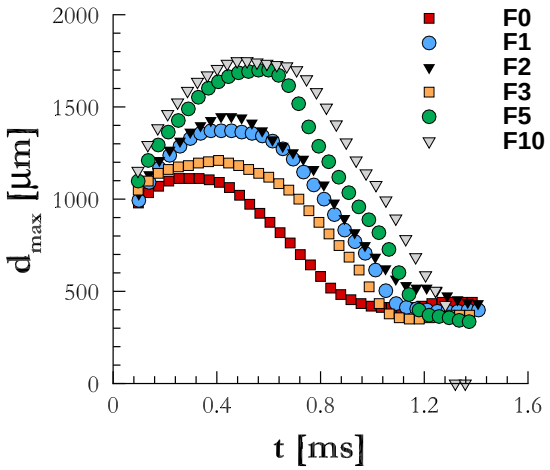

Figure 4.25: Temporal evolution of the maximum scale

The expanding of the films F5 and F10 is more pronounced than that of the other fluids. It seems that the sheet reaches larger width when its contraction is more delayed. The contraction starts sooner for mixtures of high surface tension coefficients such as F0, F1, F2 and F3.

	F0	F1	F2	F3	F5	F10
Θ [°]	33	34	36	37	39	41

Table 4.1: Opening angle of the liquid sheet

d_{max} could be used in the determination of the opening angle of the liquid sheet. Knowing the position of the first analysing window which is nearest to the discharge orifice (Fig. 4.10) $z_1 = V_q \times t_1$ and the corresponding maximum scale $d_{max}(t_1)$, the opening angle of the liquid sheets Θ is derived from

$$\tan\Theta = \frac{d_{max}(t_1) - D_{ori}}{z_1} \equiv \frac{d_{max}(t_1) - D_{ori}}{V_q \times t_1} \tag{4.19}$$

Θ for six fluids are shown in Tab. 4.1. Remark that the opening angle of the sheet increases gradually from F0 to F10. The increment between two neighbouring fluids is small, staying approximately 1 or 2 °.

Refer to chapter 2 where we recall the investigation of Brémond & Villermaux 2006 [6] on the liquid films formed by the oblique collision of two cylindrical jets. At basic state (without any perturbation introduced at the sheet edges), the sheet contour normalized by $We \times d_j$ collapses in a unique shape for different liquid Weber numbers We and incoming jet diameters d_j. The authors claim that the problem under consideration involves an equilibrium between inertia and capillarity. In like manner, we present the normalized maximum scale $\tilde{d}_{max}$ against the normalized time $\tilde{t}$ in Fig. 4.26.

$$\tilde{d}_{max} = \frac{d_{max}}{We \times D_{ori}} \text{ and } \tilde{t} = \frac{z}{We \times D_{ori}} \equiv \frac{t \times V_q}{We \times D_{ori}} \tag{4.20}$$

Remark that the six curves are almost parallel when the sheet contracts. It thus proves that a Weber number similarity is found for the shape of the bulk of the liquid film, even with the perturbations appearing on the borders of the latter.

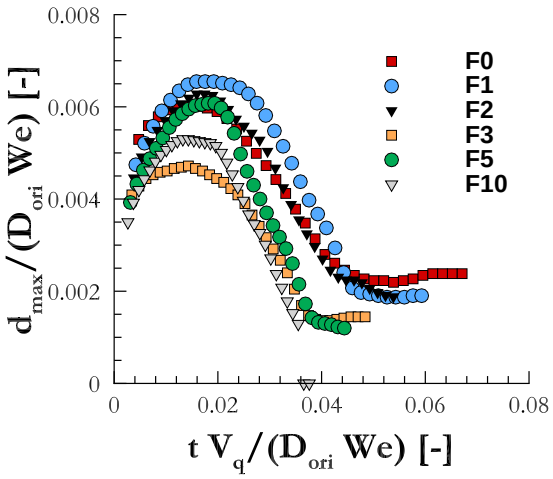

Figure 4.26: Normalized maximum scale $\tilde{d}_{max}(\tilde{t})$

Moreover, notice that from Fig. 4.26 the peak value of the normalized maximum scale $\tilde{d}_{max}(\tilde{t})$ of F0, F1, F2 and F5 are close one to another while that of two fluids F3 and F10 are smaller. The maximum values of $\tilde{d}_{max}$ for F3 and F10 are below those of the other fluids and appear earlier.

The behaviours of the liquids and their organization can be explained by the variation of the surface tension and the opening angle. Remember that as shown in

Brémond & Villermaux 2006 [6], the sheet contraction can be advanced and enhanced by the disturbances.

For the fluids F0, F1 and F2, the maximum value of $\tilde{d}_{max}(\tilde{t})$ are close one to another, showing that the sheet contraction is much alike to the one without any disturbance in Brémond & Villermaux 2006 [6]. This can be explained by the fact that a time scale t_c representing the collapse of the liquid film is smaller than that of the perturbations t_p. Remark that t_p should vary like the capillary time, similar to Brémond & Villermaux 2006 [6].

While changing from the previous fluid group to F3, the opening angle is increased (Tab. 4.1), delaying the contraction of the liquid film. It is equivalent to an increase of t_c, permitting a growth of the perturbations which in their turn, trigger the sheet contraction. Now, we have the following inequality $t_c > t_p$.

When the mixture F5 is used, the surface tension is reduced, promoting the development of the disturbances on the sheet edges. In this case, the characteristic time t_p of the perturbations overcomes that of the sheet contraction t_c. Thus, the collapse of the liquid film F5 is not activated by the disturbances and becomes similar to F0, F1 and F2.

Let's turn to F10 for which the opening angle is increased the most, causing the characteristic time of the sheet contraction to grow and we obtain $t_c > t_p$. Again, the perturbations have enough time to develop and active the sheet contraction. This explains the fact that like F3, the peak of d_{max} for F10 is smaller than that of F0, F1, F2 and F5.

4.3.1.3 *Deformation dynamics*

We analyse, in this subsection, how the liquid system evolves in time. Let's start with the calculation of the temporal derivative of the scale distribution.

$$\dot{e}_2(d,t) = \frac{\partial e_2(d,t)}{\partial t} \tag{4.21}$$

To simplify the analysis, we discuss the liquid sheets F0 and F10 solely. Figure 4.27 plots three curves $\dot{e}_2(d,t)$ which correspond to three instants. Each of them cuts

the horizontal axis at a specific scale called $d_1(t)$ which is nearest to the origin among points of intersection. In other words, $\dot{e}_2(d_1(t), t)$ is equal to zero. For the sake of clarity, $d_1(0.17\ ms) \approx 200\ \mu m$ for Fo (Fig. 4.27a) and $d_1(0.65\ ms) \approx 700\ \mu m$ for F10 (Fig. 4.27b).

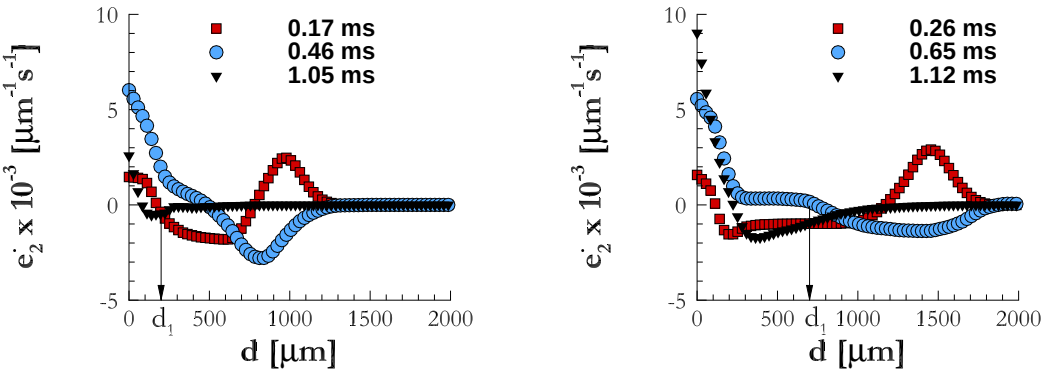

(a) Fo (b) F10

Figure 4.27: Temporal derivative of the scale distribution

When $d < d_1(t)$, $\dot{e}_2(d,t)$ is positive saying that the specific length $e_2(d,t)$ temporally increases in the small scale interval. As shown in § 4.1.1, this equivalent to the thinning of a liquid thread since $e_2(d,t)$ is the inverse of its diameter (4.9). In contrast, $\dot{e}_2(d,t)$ is negative when $d > d_1(t)$. Hence, in the large scale interval $e_2(d,t)$ decreases in time, indicating the thickening mechanism. In consequence, the scale space is delimited by $d_1(t)$ into two intervals where there is an augmentation of the specific length at scales lower than $d_1(t)$ and at the same moment, a reduction of the specific length at scales higher than $d_1(t)$. In other words, the liquid system perceives a thinning at scales lower than $d_1(t)$ whereas it suffers a thickening at scales higher than $d_1(t)$. Clearly, in the course of time $d_1(t)$ quantifies the small scale interval over which the specific length increases or a thinning mechanism occurs. This scale is expected to inquire into the temporal evolution of the atomization process where continuous evolution of the liquid-gas interface area takes place.

The dynamics of the scale $d_1(t)$ is shown in Fig. 4.28 where four distinctive zones are identified. Let's consider Fo only. In Zone 1 (up to 0.32 ms), $d_1(t)$ rises slightly getting low values. It then reaches the maximum at the beginning of Zone 2 (0.32 ms) and falls monotonously until the end of Zone 2 (0.64 ms). Between 0.64 and 0.82 ms, the scale stays nearly constant (Zone 3). It then decreases further and takes small values until the end of the breakup process (Zone 4). Clearly, in Zone

2, the specific scale $d_1(t)$ significantly increases and covers all the liquid structures that perceive the thinning mechanism, even the sheet that contracts, and not only the ligament network. $d_1(t)$ thus distinguishes different mechanisms but not liquid structures.

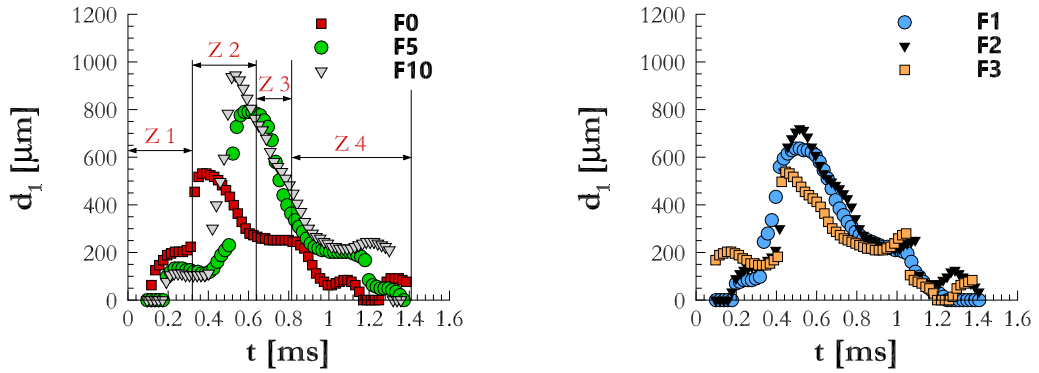

(a) Fo, F5 and F10 (b) F1, F2 and F3

Figure 4.28: Temporal evolution of the scale d_1 (Four zones Z1, Z2, Z3 and Z4 for Fo)

Moreover, we calculate the variation rate of the scale distribution $\frac{\dot{e}_2(d,t)}{e_2(d,t)}$. Figure 4.29 shows $\frac{\dot{e}_2(d,t)}{e_2(d,t)}$ as a function of scale. Remark that the variation rate at different instants stays still at d approaching zero. This behaviour is similar to a rectangle (refer to (4.10)). It thus suggests the importance of the threads at the small scale interval. In the next subsection, we thus analyse the breakup of the liquid film by using the relationships between two variation rates introduced in § 4.1.1.

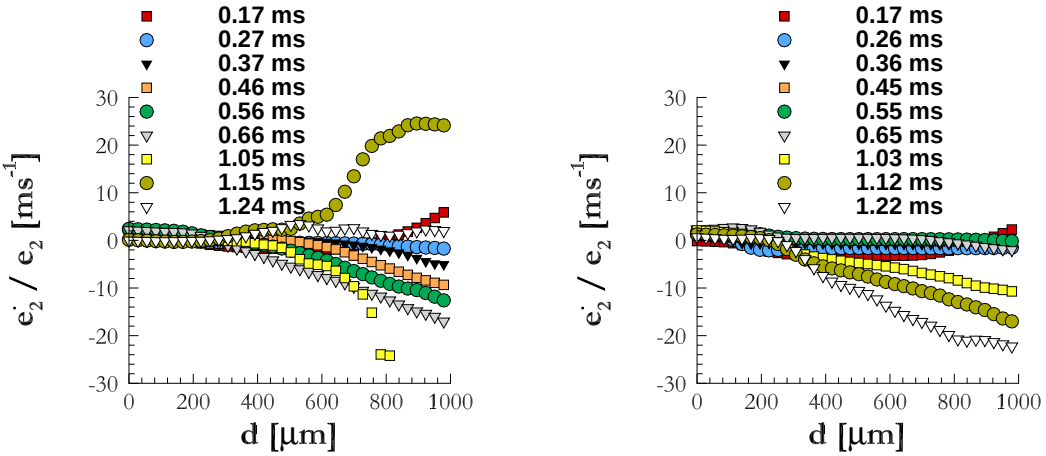

(a) Fo (b) F10

Figure 4.29: Variation rate of the scale distribution

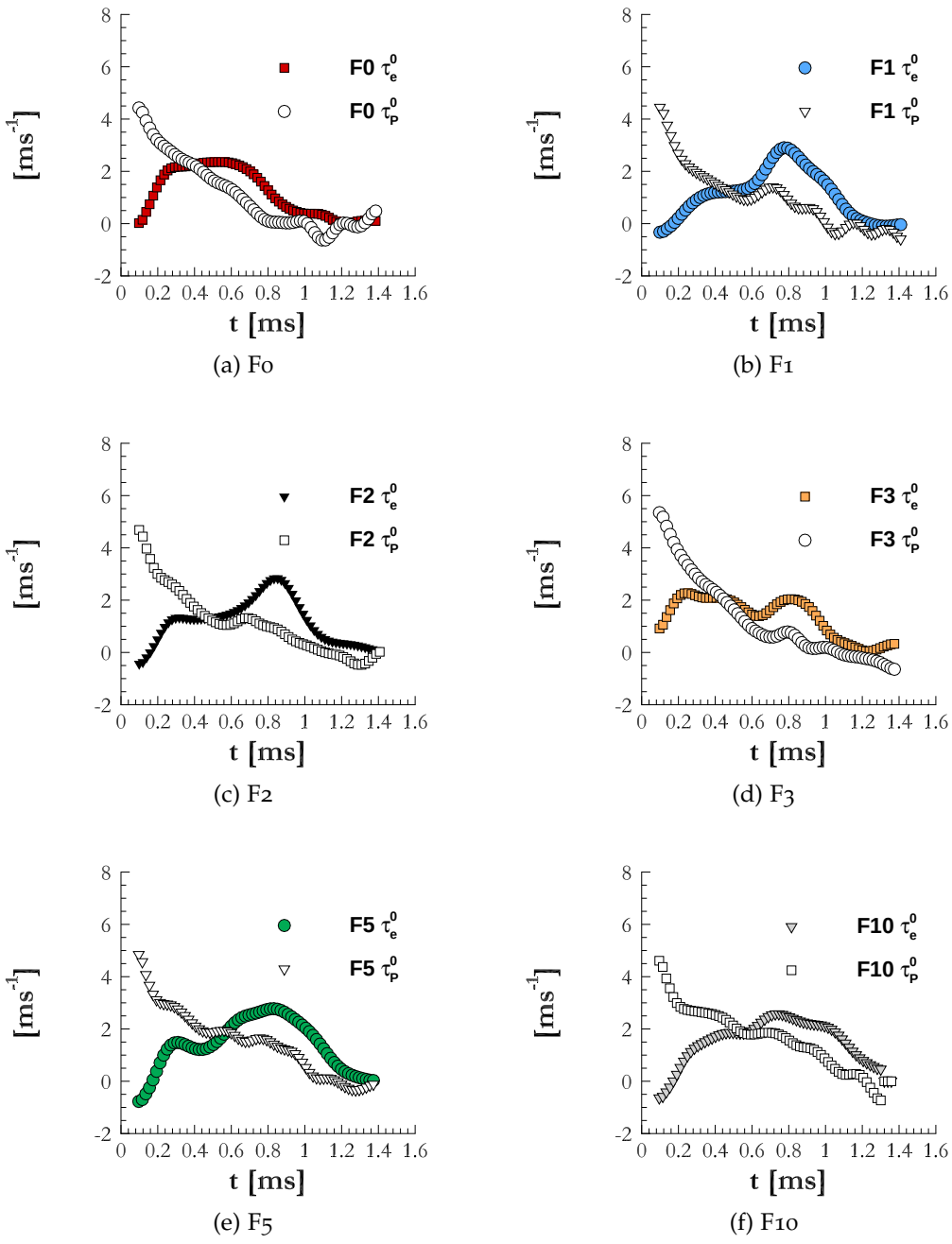

(a) Fo (b) F1

(c) F2 (d) F3

(e) F5 (f) F10

Figure 4.30: Variation rates based on the scale distribution and the contour length of the liquid system at scale zero

To characterize the deformation of the liquid system, we consider the following characteristic variation rates, similar to those of a cylindrical ligament (§ 4.1.1):

$$\tau_P^0 = \frac{\dot{P}(0,t)}{P(0,t)} \quad \text{and} \quad \tau_e^0 = 2\frac{\dot{e}_2(0,t)}{e_2(0,t)} \tag{4.22}$$

where $P(0,t)$ is the system's circumference, derived from

$$P(0,t) = 2 \times S_T(t) \times e_2(0,t) \tag{4.23}$$

(4.23) is evidenced by the fact that the scale distribution is equal to the ratio between the perimeter of the eroded system and twice the total surface of the initial liquid system (4.3).

Figure 4.30 plots τ_p^0 and τ_e^0 for six fluids. Remark that τ_p^0 is always positive. The interface is thus created throughout the process.

For each liquid, two time intervals can be distinguished during the breakup. In the first part, $\tau_p^0 > \tau_e^0$. This means that the ligaments are created at the sheet border, causing a growth of the liquid-gas interface. In the second part, τ_e^0 increases while a reduction of τ_p^0 is observed. We now have the inequality $\tau_p^0 < \tau_e^0$. Seemingly, the interface production represented by τ_p^0 is not linked to the thinning mechanism characterized by τ_e^0 in both two time intervals. These two variation rates follow one another until reaching zero at the end of the atomization process.

Notwithstanding, the information at the scale zero (Fig. 4.30) concerns the entire liquid system which includes not only the ligaments but also the liquid sheet. It is appropriate to isolate the threads before performing a similar analysis, as will be described in the next subsection.

4.3.2 *Analysis of the ligament network*

We aim to study how the liquid threads developing on the sheet borders deform throughout the atomization of the liquid film. To this end, a specific scale is first detected, allowing to delimit the ligament network from the central part of the sheet. The ligaments' geometric properties could hence be derived with help of this scale. To characterize the evolution of the ligaments, we use the variation rates as in the deformation of a cylindrical liquid filament (see § 4.1.1). This analysis is relevant at least during the first half of the sheet breakup process

4.3.2.1 *Geometrical properties*

We search for a characteristic scale d_L which isolates the filaments to the bulk of the liquid sheet (Fig. 4.31). Seemingly, at this scale the ligament network is completely erased by the erosion procedure. An abrupt perimeter loss should be recorded at d_L because the main part of the liquid system circumference consists of the ligaments' contour length. d_L seems to be equivalent to the diameter of the liquid threads.

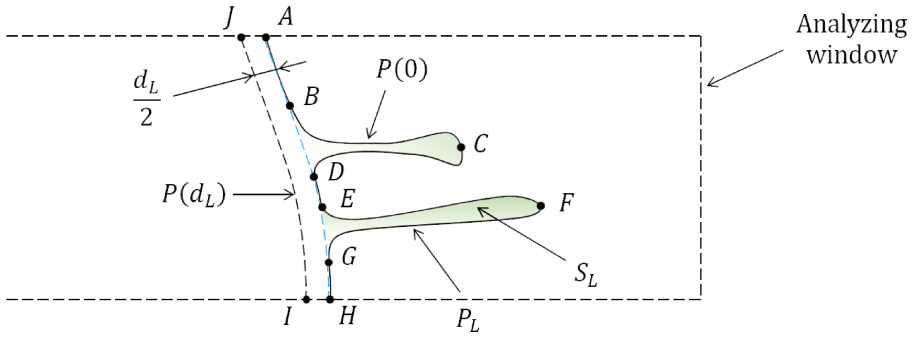

Figure 4.31: Measurement of the ligaments' geometrical properties

To detect d_L, we calculate the perimeter distribution of the eroded systems. Remember that at an instant t the scale distribution $e_2(d,t)$ is the specific length of a system resulting from the erosion of the liquid system thanks to a circle of diameter d (4.3). The circumference of the eroded system at scale d is thus

$$P(d,t) = 2 \times S_T(t) \times e_2(d,t) \tag{4.24}$$

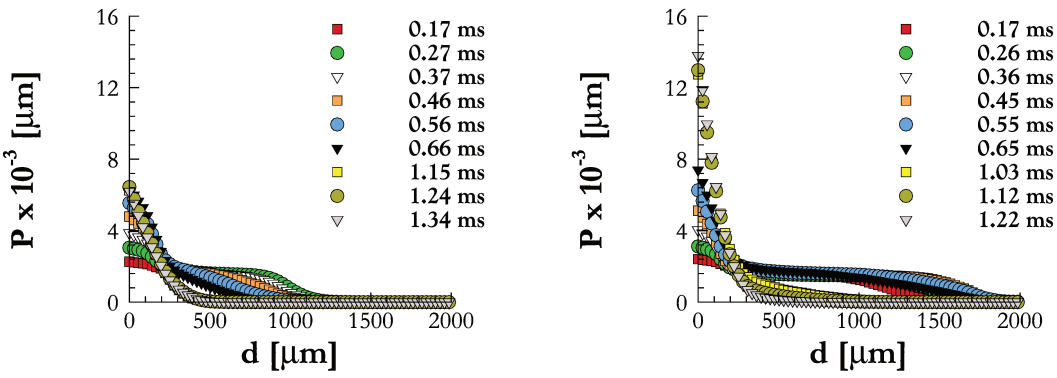

(a) Fo (b) F10

Figure 4.32: Perimeter of the eroded systems

Such distributions are depicted in Figs. 4.32a and 4.32b for the liquids Fo and F10, respectively. Notice that the perimeter distributions are similar to the scale distributions (Figs. 4.21 and 4.22).

Several curves in Fig. 4.32 have an inflexion point corresponding to d_L which can be made visible thanks to the derivative of the contour length distribution with respect to scale.

$$P'(d,t) = \frac{\partial P(d,t)}{\partial d} \tag{4.25}$$

The scale $d_L(t)$ is then defined as the one at which the minimum of $P'(d,t)$ over the small scale interval is attained (Figs. 4.33a and 4.33b). d_L varies lightly around 150 µm from one instant to another. Its values for Fo are higher than for F10.

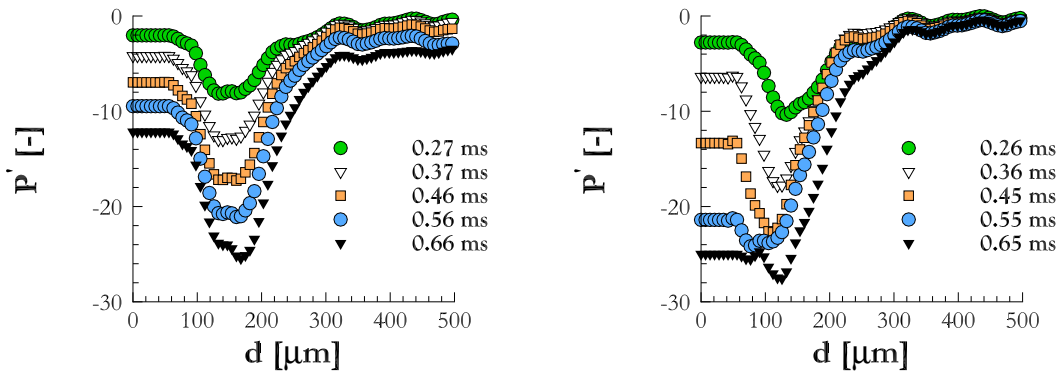

(a) Fo (b) F10

Figure 4.33: Derivative of the perimeter of the eroded systems with respect to scale

Figure 4.31 suggests how to derive, at an instant t, the ligaments' perimeter with the assumption that for all ligaments, their length is much higher than their diameter.

$$P_L = P(0) - P(d_L) \tag{4.26}$$

Although the ligaments' geometrical properties such as their perimeter $P_L(t)$ and their specific scale $d_L(t)$ depend on time, t is ignored for better readability. In fact, we suppose that the contour of the eroded system at scale d_L, represented by the dark dashed line $\overline{IJ} \equiv P(d_L)$ and the blue dashed line $\overline{AH}$ are almost parallel to one another (Fig. 4.31). Moreover, it can be seen that some parts of the liquid

system's circumference such as $\overline{AB}$, $\overline{DE}$ and $\overline{GH}$ lay on $\overline{AH}$. Clearly, the following equality is verified, explaining (4.26).

$$P_L = \widehat{BCD} + \widehat{EFG} \tag{4.27}$$

Also, the ligaments' surface area in Fig. 4.31 can be estimated as

$$S_L = E_2(d_L) \times S_T - \frac{d_L}{2} \times P(d_L) = E_2(d_L) \times S_T - d_L \times e_2(d_L) \times S_T \tag{4.28}$$

As previously assumed, $\overline{IJ}$ is parallel to $\overline{AH}$ permitting the surface area delimited by these two curves to be expressed by

$$S_{AHIJ} \approx P(d_L) \times \frac{d_L}{2} \tag{4.29}$$

Since the outer surface bounded by the black dashed line $\overline{IJ}$ is the lost area after the erosion at scale d_L and by using (4.24), we obtain the following relationship, explaining (4.28).

$$S_L = E_2(d_L) \times S_T - S_{AHIJ} \tag{4.30}$$

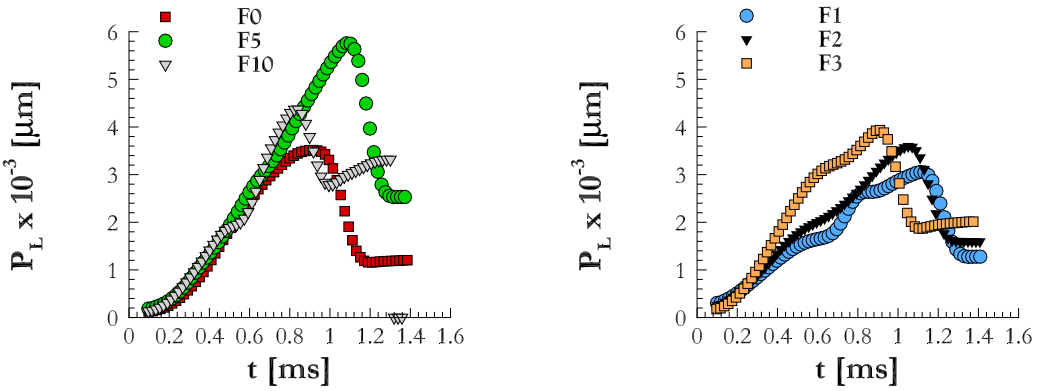

(a) F0, F5 and F10 (b) F1, F2 and F3

Figure 4.34: Ligaments' perimeter

The perimeter and surface area of the ligaments for six fluids are shown in Figs. 4.34 and 4.35, respectively. The ligaments' perimeter and surface area increase to reach their peak almost at the same moment. Additionally, one can notice great likelihood between the surface area and the perimeter curves for each fluid. The peak of the perimeter and surface area indicates the beginning of the breakdown

of the liquid threads. It occurs more early for F3 and F10 than other fluids. In particular, for F10 after the instant corresponding to the maximum value of P_L and S_L, the ligaments' length and surface tend to increase lightly. This can be explained by the development of the threads on the left edge of the liquid film (see Figs. 4.16 and 4.17).

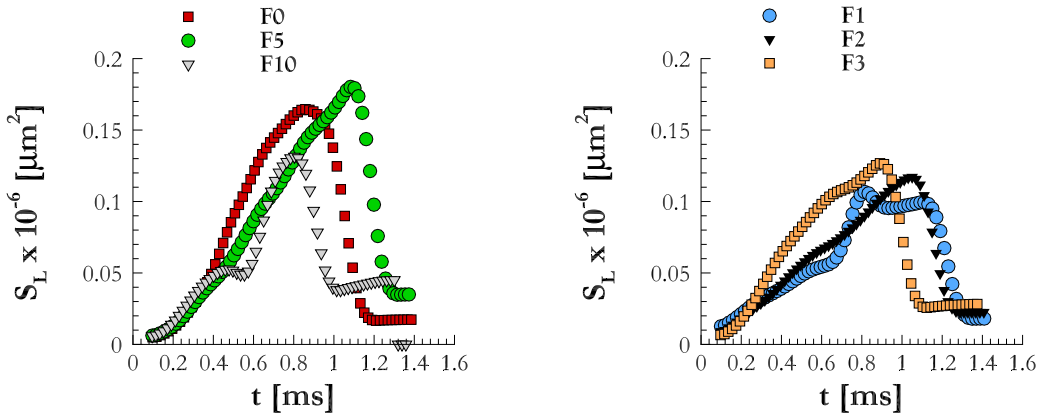

(a) F0, F5 and F10

(b) F1, F2 and F3

Figure 4.35: Ligaments' surface area

The previous measurement of two geometrical properties of the liquid threads allows their specific length to be determined in the same way as the surface-based scale distribution.

$$e_2^L = \frac{P_L}{2 \times S_L} \tag{4.31}$$

The temporal evolution of e_2^L for six liquids is depicted in Fig. 4.36. Remark that the specific length of F5 and F10 is higher than that of F0 during the whole process. e_2^L for F0 stays almost constant during the first part of the atomization, saying that the ligaments' diameter does not vary significantly. The evolution of the specific length for the mixture F10 is pronounced. It increases from the beginning of the process until reaching a peak around 0.6 ms. This indicates that the diameter of the liquid threads is reduced. In general, the specific length at the end of the breakup process depend on the surface tension.

4.3.2.2 *Deformation dynamics*

We are now interested in how the ligaments deform during the breakup process. Remember that they are delimited from the liquid system by the scale d_L. Inspired by the analysis of an individual liquid thread in § 4.1.1, the variation rates of the filaments' perimeter and specific length are computed as below.

$$\tau_P^L = \frac{\dot{P}_L}{P_L} \text{ and } \tau_e^L = 2\frac{\dot{e}_2^L}{e_2^L} \tag{4.32}$$

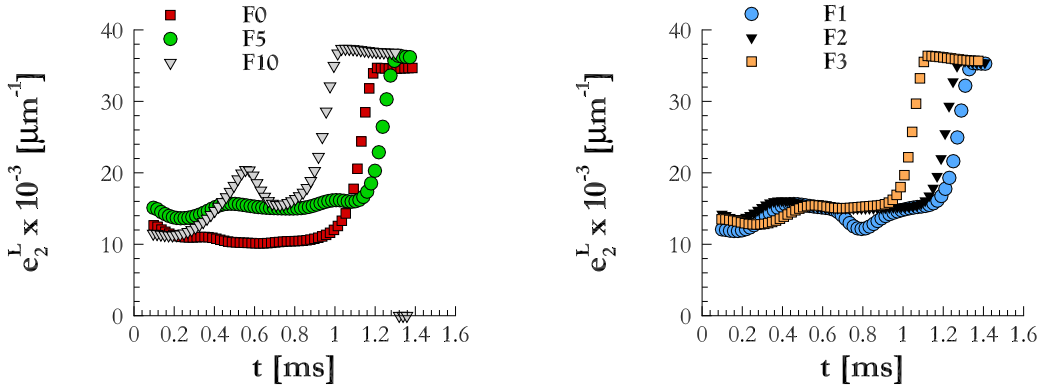

(a) F0, F5 and F10 (b) F1, F2 and F3

Figure 4.36: Specific length of the ligaments

These variation rates are displayed in Fig. 4.37, from which several remarks relative to the behaviours of six fluids can be drawn.

At the beginning of the process, i.e. before 0.2 ms, the elongation rate of the ligaments, represented by τ_P^L, is positive for all fluids. This means that the liquid threads are produced at the sheet borders. At the same time, τ_e^L is negative and close to zero. One can explain the inequality $\tau_e^L < 0$ by the reduction of e_2^L (Fig. 4.36). The latter happens during the formation of the ligaments where their diameter grows from zero to a certain positive value. Inversely linked to the ligaments' diameter, e_2^L thus decreases and leads to negative τ_e^L.

In the next period, the specific length variation rate τ_e^L changes its direction, except for F0. It increases rapidly until a maximum value then shrinks to nil. Positive values of τ_e^L signify a thinning of the threads. Notice that the ligaments' length continues to grow for all fluids but less and less rapidly since τ_P^L, while remaining

positive, declines to reach zero. This time interval lasts shorter for F1 and F2 than for F5 and F10, stopping at around 0.4 ms for the former versus 0.5 ms for the latter. On the other hand, the thinning of the F3 ligaments is delayed and τ_e^L keeps staying above zero even at 0.6 ms.

Later on, the two variation rates approach one another then intersect when both of them attain zero or when the ligaments start to break down into droplets. The duration of this period differs across liquids with the end point ranging from 0.6 ms for F3 to 1 ms for F2 and F5. The intersection between the two curves τ_p^L and τ_e^L for F1 and F10, however, occurs twice because τ_p^L starts to increase again from 0.6 ms for F1 and from 0.5 ms for F10. This is due to the existence of the ligaments on the left edge of the liquid sheet.

Towards the end of the process, the diminution of τ_p^L is registered together with the escalation of τ_e^L, suggesting an interface loss and a reduction in size of the liquid structures, respectively. In effect, the fragmentation of the ligaments takes place in this stage. Moreover, the peak of τ_e^L coincides with the trough of τ_p^L, at the same moment as the rupture of the liquid threads (refer to Figs. 4.34 and 4.35).

Interestingly, the comparison of τ_p^L and τ_e^L can result in the division of the fluids into three subgroups. The first one contains Fo whose τ_e^L always stays around zero. Although its ligaments increase in length while remaining constant in diameter. Near-zero τ_e^L implies that the threads are not stretched at all during the whole process. In the second group, one can find F2, F3 and F5 because their behaviours are much alike in terms of τ_p^L and τ_e^L. The ligaments lengthen from their formation until their fragmentation and the liquid thread stretching is recorded as $\tau_e^L > 0$. Finally, F1 and F10 are classified in the last group. Their τ_p^L and τ_e^L curves intersect twice, proving that the ligaments appear on the left border of the liquid sheet.

Marmottant & Villermaux [58] and Dumouchel 2017 [27] scrutinize the resultant sprays formed by the division of the stretched ligaments. It is claimed that if the elongation rate is high or the characteristic time of the stretching is small compared to that of the capillary instability, the thread breaks down into drops with large size distribution and numerous small droplets are formed. In contrast, sprays of narrow diameter spectrum are obtained when the capillary instability is dominant. In the next subsection, we shall examine if there is a link between the deformation of the ligaments on the drop-size distribution of the resulting sprays.

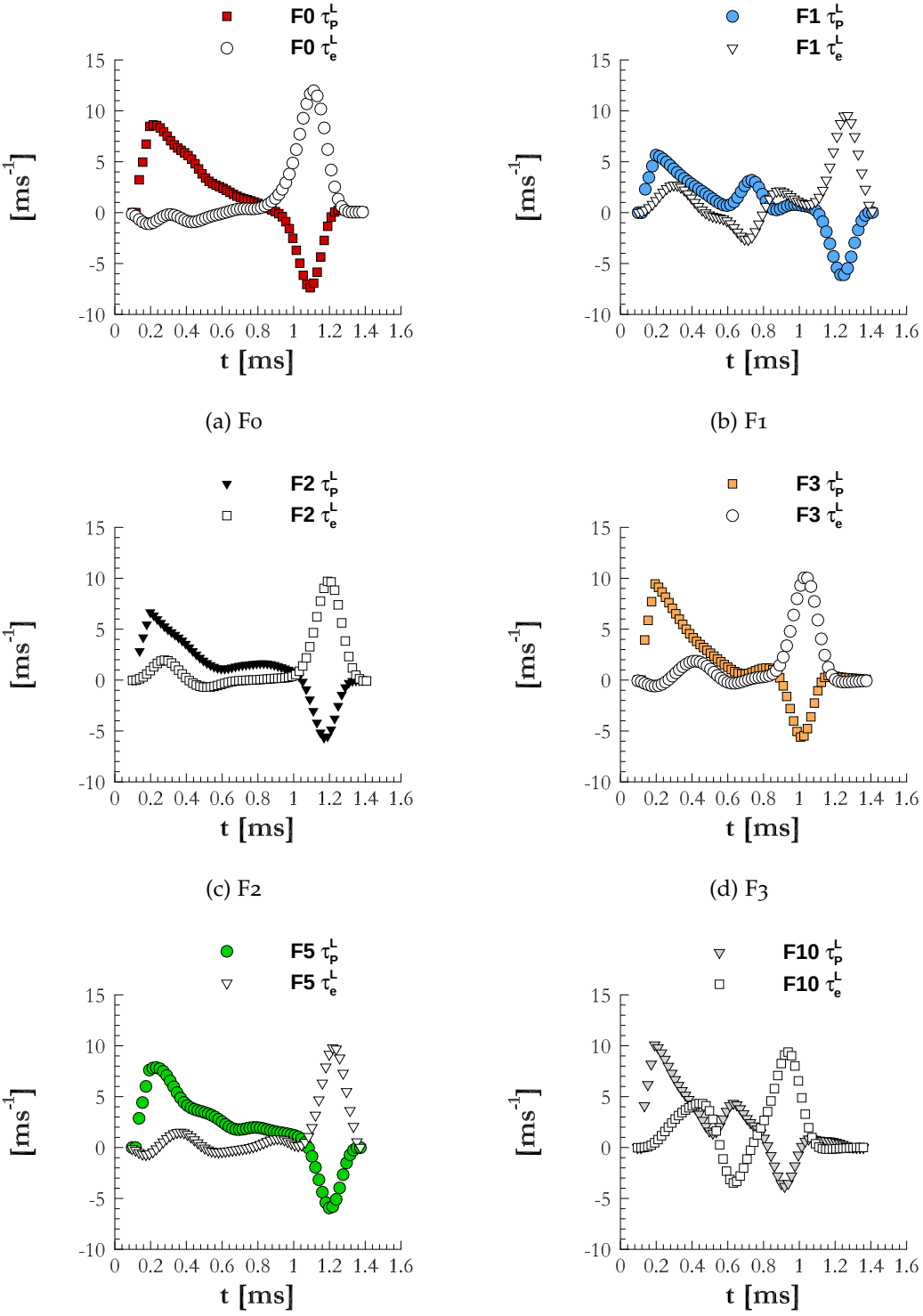

(a) F0

(b) F1

(c) F2

(d) F3

(e) F5

(f) F10

Figure 4.37: Variation rates based on the perimeter and specific length of the ligaments

4.3.3 *Characteristics of the sprays*

This subsection investigates the spray produced from the breakup of the ligaments, which is presented in § 4.3.2. Remember the pronounced elongation of the F10 ligaments in opposition with those of Fo that are not stretched at all during the whole process. We examine the effects of the liquid thread stretching on the polydispersion of the resulting drops as well as the formation of the small droplets. The analysis of the spray is carried out in two following steps.

We first extract all detached liquid objects from the binary images. Their diameter-distribution is built, showing two distinct size-intervals. This enables a threshold to be detected. Since we are interested only in the fine droplets formed from the rupture of the liquid threads, drops of diameter lower than that threshold are retained for further analysis.

In the second step, we establish for the selected droplets their scale distribution. Indeed, the latter can be in turn fitted by the scale distribution of a set of circles. Put it differently, the droplets and these circles are equivalent in terms of scale distribution. The diameter spectrum of these circles can be represented by a Gamma function whose parameters allow for a quantitative comparison of the sprays among six fluids.

4.3.3.1 *Extraction of the small droplets*

To extract the droplets from the entire system, we remove the liquid sheet which is the biggest object in the binary pictures. Examples of resultant images for Fo at postion "up" and "down" are shown in Figs. 4.38 and 4.39, respectively. It can be seen that some large liquid structures still remain.

Thanks to different image processing programs, the size-histogram of all remaining liquid elements is built as follows. The surface area S_i of a drop i is first measured, useful to calculate the diameter D_i of an equivalent sphere having the same projected area. In other words, D_i satisfies the equality $\frac{\pi D_i^2}{4} = S_i$. The volume of the sphere is thus derived from its diameter as $\frac{\pi D_i^3}{6}$, allowing to establish the volume-based drop-size distribution (Fig. 4.40a). Notice that the size of the de-

tached liquid structures is below 1300 µm. Moreover, they can be divided into two distinct intervals by a diameter threshold of 600 µm. Aiming to choose the small drops issued from the ligaments' breakup, only droplets with size lower than this limit are kept for further analysis. Their diameter-distributions are depicted in Fig. 4.40b.

It is clear from Fig. 4.40a that more small droplets are formed for F10 than other fluids. Furthermore, it has few large liquid elements since the maximum diameter is around 800 µm. Inversely, for the fluid Fo, only few small-size drops together with many large liquid objects are found.

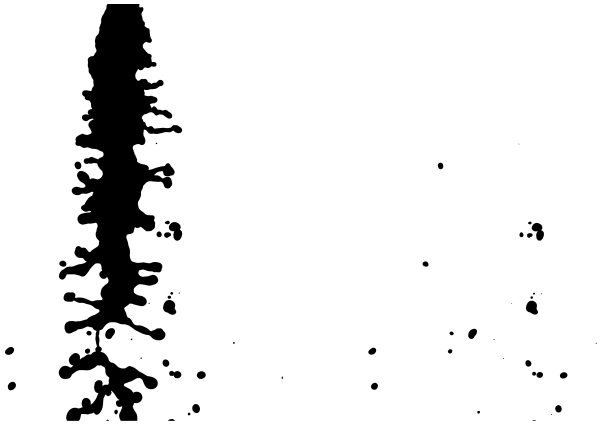

(a) Liquid system (b) Droplets

Figure 4.38: Extraction of drops from a snapshot Fo - Position "up"

(a) Liquid system (b) Droplets

Figure 4.39: Extraction of drops from a snapshot Fo - Position "down"

4.3.3.2 *Drop-scale distribution*

Procedures as described in § 4.1 are applied to the images of the drops having their diameter smaller than 600 µm at position "up" and "down" to obtain the drop-scale distributions of the sprays. The measurement of the cumulative scale distribution is carried out in the whole euclidean distance maps. This is to say that a large analysing window is used to completely cover each image. Figure 4.41 shows the surface-based scale distribution for six fluids. Remark that $e_2(d)$ decreases gradually while the scale d increases. The scale distribution approaches zero for the scales larger than 200 µm. Moreover, $e_2(d)$ at the scale zero for Fo is small, indicating lower interface created per surface unity compared to the other fluids. A poor atomization efficiency is thus expected for Fo, with few small droplets and a narrow drop size-distribution.

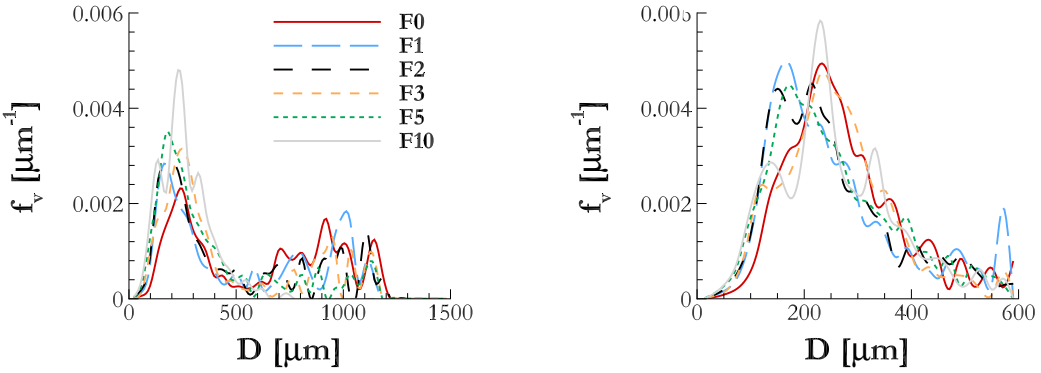

(a) Drop-size distribution of the sprays

(b) Drop-size distribution with the diameter threshold of 600 µm

Figure 4.40: Volume-based drop-size distribution

We employ the findings of Dumouchel et al. 2008 [21] who introduce the scale distribution of a set of circles.

$$e_2(d) = \frac{2\nu}{D_{10}} \frac{\Gamma\left(\nu+1, \frac{\nu d}{D_{10}}\right) - \frac{\nu d}{D_{10}}\Gamma\left(\nu, \frac{\nu d}{D_{10}}\right)}{\Gamma(\nu+2)} \tag{4.33}$$

$\Gamma(x, y)$ is the incomplete Gamma function with ν characterizing the size dispersion of the spray. The larger the parameter ν, the narrower the drop-size spectrum. D_{10} is the arithmetic mean diameter of the spray, defined as the average diameter of a set of equivalent spheres. Concretely, D_{10} can be calculated as $\sum_{i=1}^{N} D_i/N$ where N is the total number of objects (see § 4.3.3.1). The formula (4.33) is applied

to the droplets issued from the fragmentation of the ligaments which appear during the breakup of the liquid sheets produced by a triple-disk injector (Dumouchel et al. 2015 [26]). It is said that when the stretched ligaments break down, they form drops whose number-based diameter distribution can be well represented by a Gamma function (Marmottant & Villermaux 2004 [58]).

$$f_n(D) = \frac{\nu^\nu}{\Gamma(\nu)} \frac{D^{\nu-1}}{D_{10}^\nu} exp\left(-\nu \frac{D}{D_{10}}\right) \tag{4.34}$$

We fit the scale distributions issued from the experimental dataset to the function (4.33), as shown in Fig. 4.41. The agreement between $e_2(d)$ of the droplets and the formula (4.33) is satisfactory. Remark that instead of a direct fitting by the Gamma function of the diameter-distribution of a set of equivalent circles (Fig. 4.40), we fit the scale distribution by the formula (4.33). The reason for this lies in the fact that in the fitting of the drop-size spectrum by the Gamma function, the circular objects are built based on equivalent surface; whereas for the scale distribution, a set of circles with similar scale distribution is found, giving more importance to the liquid-gas interface. Moreover, the shape of the liquid structures are taken into account since the scale distribution is shape-dependent.

	F0	F1	F2	F3	F5	F10
ν [–]	1.62	1.60	1.62	1.41	1.04	1.01
D_{10} [µm]	82	69	68	68	52	51

Table 4.2: Parameters of the Gamma function

The fitting parameters are exhibited in Tab. 4.2. Some remarks can be made from these results.

For the F5 and F10 sprays, the arithmetic mean diameters D_{10} are small, meaning that fine droplets are produced. Moreover, low values in their dispersion parameters ν point out broader drop-size distributions compared to other mixtures. Remember that the ligaments of F5 and F10 undergo marked elongation which delays their division into droplets. As stated in Marmottant & Villermaux 2004 [58] and Dumouchel et al. 2015 [26], the fragmentation of the stretched ligaments results in wide drop-size distribution with numerous small droplets, which enhances the atomization efficiency.

Note that even the behaviour of F5 is different to F10, its droplets are much dispersed in size, similar to those of F10. This can be explained by a high snapshot-to-snapshot fluctuations of the liquid F5, proven by its backlit images. The F5 ligaments vary from one image to another and are continuously stretched during the process. They thus disrupt into drops of different diameters, increasing the poly-dispersion of the spray. A detailed analysis should be done, based on the root-mean-square-deviation of the cumulative scale distribution (4.18). Moreover, the specific length of the ligaments for F5 are higher than other fluids (Fig. 4.36). These threads are more deformed and corrugated, giving irregular droplets.

As regards F0, both D_{10} and ν are high so the resultant drops are large and of equal size. It is shown in § 4.3.2.2 that the F0 ligaments are not stretched and their diameter is unvarying during the whole process. The poly-dispersion of the drops formed by the breakup of these ligaments is rather due to their snapshot-to-snapshot fluctuations (see Fig. 4.23). In other words, these liquid threads are divided into droplets of different diameters due to the variations of their form and size from one image to another.

With reference to the last three fluids F1, F2 and F3, their drop-size dispersions are not as pronounced as F5 and F10 but more marked than F0. For each liquid, the behaviour above can be explained differently. The F2 ligaments are stretched during long time but at a lower elongation rate than F5 and F10. In case of F3, its threads increase in length at a high τ_p^L but within a short time interval of approximately 0.6 ms. For the liquid F1, one can notice small values of τ_p^L together with a short duration of the elongation process. Moreover, the fact that τ_p^L becomes positive from 0.6 to 0.8 ms signifies the development of the ligaments of large diameter on the left border of the liquid film. These threads are not stretched because τ_e^L is negative in this period. Their diameter is thus higher than those appear earlier on the other side of the sheet. In consequence, large droplets are formed from the breakdown of the F1 ligaments.

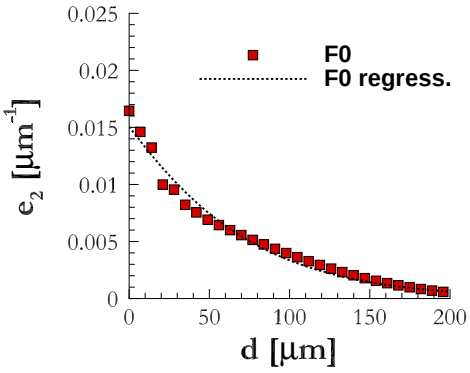

(a) F0

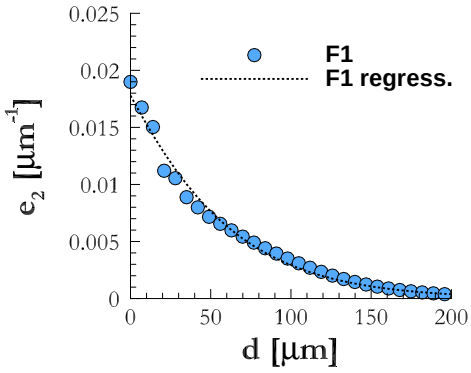

(b) F1

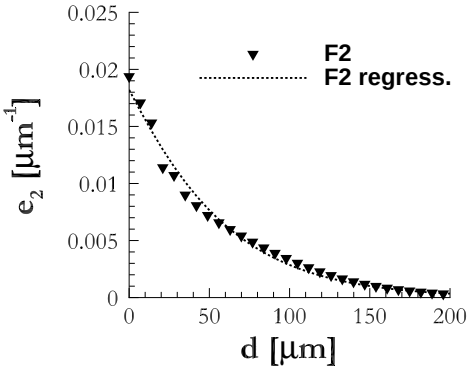

(c) F2

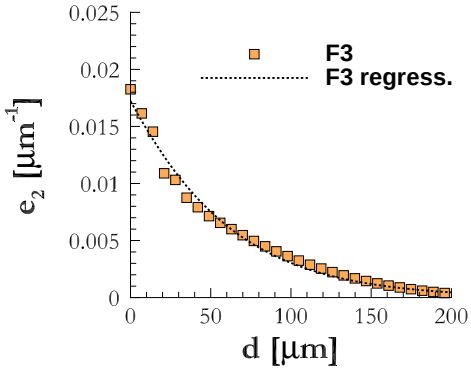

(d) F3

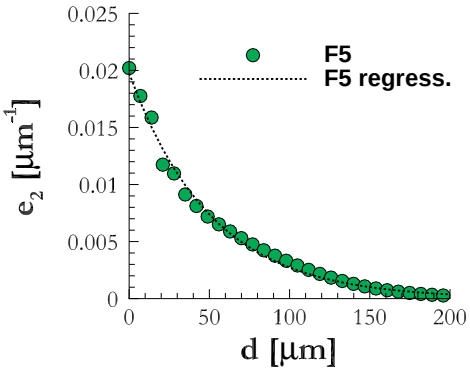

(e) F5

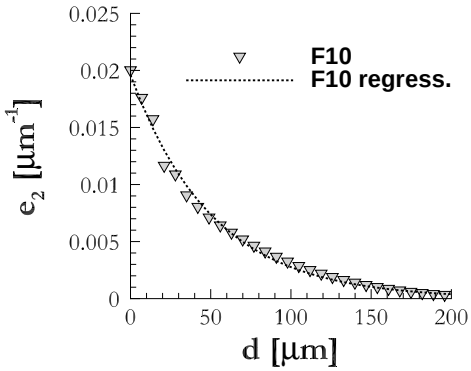

(f) F10

Figure 4.41: Fitting of the drop-scale distribution

5

IMMERSED BOUNDARY METHOD

As we have seen in chapters 2 and 4, both secondary flow and turbulence are highly influential to the spray formation. Therefore, to numerically solve the atomization process, including both internal and external flows is necessary.

We now present how to realize such a connection. Essential features of ARCHER^{TM} – our home-made 3D incompressible Navier-Stokes solver are first recalled, based on Tanguy 2004 [93], Ménard 2007 [59], Noël 2012 [66], Duret 2013 [29] and Vaudor 2015 [98]. Then, the coupled level-set, volume-of-fluid and ghost-fluid method, available in these studies is combined with two relevant immersed boundary methods to take into account the fixed solid frontier. For validation purpose, tests and comparisons to analytical solutions are performed. At the end of this chapter, a numerical simulation of a liquid jet issued by a cylindrical nozzle is carried out. We equally perform an other application on a planar film emanating from the triple-disk injector.

The objective of our numerical work is to solve a liquid-gas flow in a rectangular computational domain Ω with irregular solid boundaries (Fig. 5.1). Ω is comprised of a solid region Ω_s and a fluid region which is formed by a liquid region Ω_l and a gas region Ω_g. The liquid-gas interface and its normal towards the liquid phase are denoted by Γ and $\mathbf{n}_\Gamma$, respectively. Similarly, Γ^{ib} is the solid frontier and $\mathbf{n}^{ib}$ its outward normal. $\partial\Omega$ indicates the boundary of Ω.

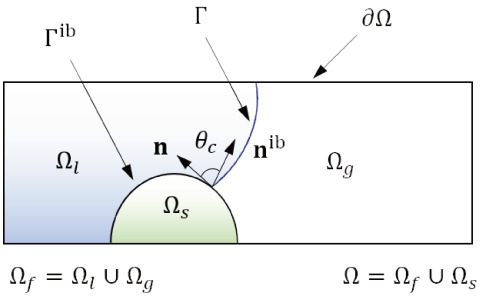

Figure 5.1: Set-up of a rectangular computational domain for a liquid-gas flow with irregular solid boundaries

To numerically simulate such a two-phase flow with solid boundaries in the domain Ω, the latter is discretized into a grid. Continuous fluid dynamics equations are converted into a discrete linear system of algebraic equations, able to be solved by classical methods. In this way, the problem of searching the exact and continuous solution is replaced by another to find out the approximate and discrete values. Each of these discrete values should obviously be located in a given space. In the framework of the marker-and-cell (MAC) method (Harlow & Welch 1965 [46]), we store in the center of a grid-cell the pressure p and the level-set and volume-of-fluid functions indicating the position of the liquid-gas interface and the solid frontier (Fig. 5.2). Their details will be summarized in § 5.4 and § 5.5.

For incompressible flows, the pressure is monitored to force the free-divergence of the velocity field. In fact, it is raised or lowered depending on whether net inflow or outflow enters the control volume (Tryggvason et al. 2011 [95]). To compute inflow or outflow, one needs horizontal velocity components u at the vertical boundaries and their perpendicular counterparts v on the horizontal borders. These two velocity components are therefore placed in the middle of the corresponding boundaries. Hence, the grid for u is shifted half a mesh to the right

from the pressure point and the grid for v is moved upward by the same distance.

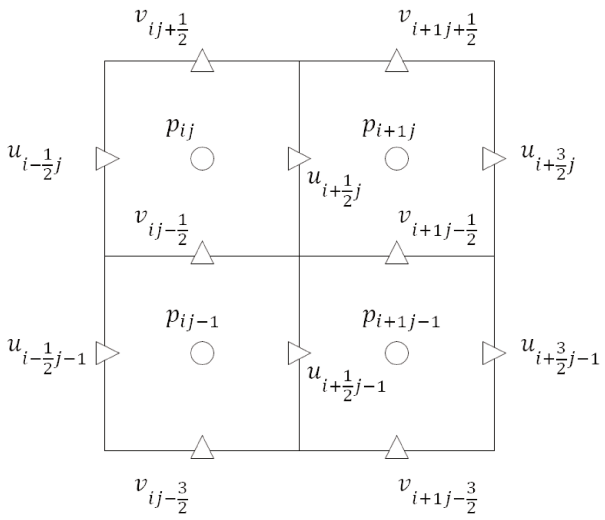

Figure 5.2: A standard MAC grid configuration

5.2 NAVIER-STOKES EQUATIONS, JUMP CONDITIONS ACROSS THE LIQUID-GAS INTERFACE AND BOUNDARY CONDITIONS ON THE SOLID FRONTIER

5.2.1 *Navier-Stokes equations*

To model a fluid flow in our computational domain Ω, one might start with the incompressible Navier-Stokes equations.

$$\frac{\partial(\rho\mathbf{U})}{\partial t} + (\mathbf{U}\cdot\nabla)\,\rho\mathbf{U} = -\nabla p + \nabla\cdot(2\mu\mathbf{D}) + \sigma\kappa\mathbf{n}_\Gamma\delta_\Gamma \tag{5.1a}$$

$$\frac{\partial\rho}{\partial t} + \nabla\cdot(\rho\mathbf{U}) = 0 \tag{5.1b}$$

where $\mathbf{U}$ is the velocity field, p the pressure, t the time, ρ the mass density, μ the dynamic viscosity, σ the surface tension coefficient, κ the liquid-gas interface local mean curvature, δ_Γ the multidimensional Dirac distribution localized at the interface and $\mathbf{D} = \frac{1}{2}(\nabla\mathbf{U} + \nabla\mathbf{U}^T)$ the rate-of-deformation tensor.

The mass conservation equation (5.1b) can be developed as

$$\underbrace{\frac{\partial \rho}{\partial t} + (\nabla \cdot \mathbf{U})\,\rho}_{\frac{D\rho}{Dt} = 0 \text{ due to the incompressibility}} + (\mathbf{U} \cdot \nabla)\,\rho = 0 \tag{5.2}$$

to obtain

$$\nabla \cdot \mathbf{U} = 0 \tag{5.3}$$

We now have a set of two equations: the momentum equation (5.1a) and the continuity equation (5.3).

5.2.2 *Jump conditions across the liquid-gas interface*

Across the liquid-gas interface, the jump conditions for density, viscosity and pressure read

$$\begin{aligned} [\rho]_\Gamma &= \rho_l - \rho_g \\ [\mu]_\Gamma &= \mu_l - \mu_g \\ [\mathbf{n} \cdot (p\mathbf{I} - 2\mu\mathbf{D}) \cdot \mathbf{n}]_\Gamma &= \sigma\kappa \end{aligned} \tag{5.4}$$

where $[\cdot]$ the jump of the variable $\cdot$ across the interface, $\mathbf{I}$ the identity matrix, ρ_l, ρ_g the mass density and μ_l, μ_g the dynamic viscosity of the liquid and the gas, respectively.

5.2.3 *Boundary conditions on the fixed solid frontier*

Since we restrict ourself to fixed solid boundaries, the no-slip condition applied for the velocity is given by

$$\mathbf{U}|_{\Gamma^{ib}} = \mathbf{U}_s|_{\Gamma^{ib}} = \mathbf{O} \tag{5.5}$$

and by using scale analysis inside the boundary layer, it can be shown that the pressure gradient satisfies

$$\left(\mathbf{n}^{ib} \cdot \nabla p\right)\Big|_{\Gamma^{ib}} = 0 \tag{5.6}$$

5.3 PROJECTION METHOD

So as to solve the incompressible Navier-Stokes equations, a projection method (Chorin 1968 [13]) is adopted which proceeds in three steps.

Step 1 From the solution $\mathbf{U}^n$ at time $t^n = n\Delta t$, where Δt is the time step, we calculate an intermediate velocity via the momentum equation (5.1a). The pressure gradient is ignored here.

$$\mathbf{U}^* = \mathbf{U}^n + \frac{\Delta t}{\rho^{n+1}}\left[(-\mathbf{U}^n \cdot \nabla)\,\rho^n \mathbf{U}^n + \nabla \cdot \left(2\mu^{n+1}\mathbf{D}^*\right) + \sigma\kappa^{n+1}\mathbf{n}_\Gamma \delta_\Gamma\right] \tag{5.7}$$

The convection term $(\mathbf{U}^n \cdot \nabla)\,\rho^n \mathbf{U}^n$ and the diffusion term $\nabla \cdot \left(2\mu^{n+1}\mathbf{D}^*\right)$ are approximated by different numerical schemes depending on which approach among the finite difference method (§ 5.6) or the finite volume method (§ 5.7). In addition, since the transport of the liquid-gas interface is performed before solving (5.7), ρ^{n+1}, μ^{n+1} and κ^{n+1} are known. The treatment of the diffusion term, as shown in (5.7), is implicit. We enforce the no-slip condition even for the intermediate velocity.

$$\mathbf{U}^*|_{\Gamma^{ib}} = \mathbf{O} \tag{5.8}$$

Step 2 We derive the Poisson equation for pressure by using the continuity equation (5.3).

$$\nabla \cdot \left(\frac{\nabla p^{n+1}}{\rho^{n+1}}\right) = \frac{\nabla \cdot \mathbf{U}^*}{\Delta t} \tag{5.9}$$

with homogeneous and non-homogeneous Neumann boundary conditions on $\partial\Omega$ and Γ^{ib}, respectively.

$$\mathbf{n}^{ib} \cdot \frac{\nabla p^{n+1}}{\rho^{n+1}}\bigg|_{\Gamma^{ib}} = \mathbf{n}^{ib} \cdot \frac{\mathbf{U}^*}{\Delta t}\bigg|_{\Gamma^{ib}} \tag{5.10}$$

Like the convection and diffusion terms in (5.7), (5.9) on irregular domains is discretized differently within each of the two approaches - the finite difference method (§ 5.6) or the finite volume method (§ 5.7).

Step 3 Once p^{n+1} is obtained, we compute the final solution at time t^{n+1}.

$$\mathbf{U}^{n+1} = \mathbf{U}^{*} + \Delta t \, \frac{\nabla p^{n+1}}{\rho^{n+1}} \tag{5.11}$$

Note that the Neumann condition (5.10) is deduced from the no-slip boundary condition (5.5) for the final solution (5.11).

$$\mathbf{U}^{n+1}\Big|_{\Gamma^{ib}} = \mathbf{O} \tag{5.12}$$

Moreover, the combination of the no-slip condition for the intermediate velocity (5.8) and the Neumann condition (5.10) fulfils the condition for the pressure gradient on the solid frontier (5.13).

$$\left(\mathbf{n}^{ib} \cdot \nabla p^{n+1}\right)\Big|_{\Gamma^{ib}} = 0 \tag{5.13}$$

5.4 LIQUID-GAS INTERFACE TRACKING

An important part of the flow numerical study consists in tracking the liquid-gas interface. The level-set and volume-of-fluid methods are traditionally used to accomplish this task. Fortunately, due to their complementarity, a combination of these two approaches is possible and has indeed proven its efficiency. In this section, we recall some essential features of the two techniques before presenting the joined one namely the coupled level-set, volume-of-fluid (CLSVOF) method.

5.4.1 *Level-set method*

The level-set method is based on the implicit definition of the interface as the zero-level of a continuous function $\phi(\mathbf{x}, t)$ (Osher & Sethian 1988 [69]). To guarantee that $\phi(\mathbf{x}, t)$ is the distance of a given point $\mathbf{x}$ from the interface, with positive sign

in liquid and negative sign in gas, $|\nabla\phi(\mathbf{x},t)| = 1$. The motion of the interface $\phi(\mathbf{x},t) = 0$ by the velocity field $\mathbf{U}$ is given by

$$\frac{\partial\phi(\mathbf{x},t)}{\partial t} + (\mathbf{U}\cdot\nabla)\,\phi(\mathbf{x},t) = 0 \tag{5.14}$$

The level-set function can no longer be a distance function when $|\nabla\phi(\mathbf{x},t)| \neq 1$ due to high velocity gradients. A re-distancing algorithm is thus applied to reorganize the level-set field without modification of the zero-level curve (Sussman et al. 1998 [89]). The reinitialization equation

$$\frac{\partial d(\mathbf{x},\tau)}{\partial\tau} = \mathrm{sign}(\phi(\mathbf{x},t))\,(1 - |\nabla d(\mathbf{x},\tau)|) \tag{5.15}$$

is iterated in virtual time τ with the sign function being smoothed in the vicinity of the interface.

$$\mathrm{sign}(\phi(\mathbf{x},t)) = \frac{\phi(\mathbf{x},t)}{\sqrt{\phi^2(\mathbf{x},t) + \Delta x^2}} \tag{5.16}$$

In each time step, (5.14) is first solved to initialize $d(\mathbf{x},\tau=0) = \phi(\mathbf{x},t)$. Then, we iterate (5.15) until a steady state is attained, i.e. either $\mathrm{sign}(\phi(\mathbf{x},t)) = 0$, meaning that the interface is preserved, or $|\nabla d(\mathbf{x},\tau_{steady})| = 1$ which is a distance function. Finally, the equality $\phi(\mathbf{x},t) = d(x,\tau_{steady})$ is imposed. In practice, we run three iterations by the 3^{th} order Runge-Kutta method to solve (5.15).

5.4.2 *Volume-of-fluid method*

Another way to track the interface is the volume-of-fluid method (Hirt & Nichols 1981 [48]). Inside a computational grid-cell Ω_{ij} at an instant t, a color function is defined as

$$c(\mathbf{x}) = \begin{cases} 0 & \text{if } \mathbf{x} \in \text{ gas} \\ 1 & \text{if } \mathbf{x} \in \text{ liquid} \end{cases} \tag{5.17}$$

The marker function $F\left(\Omega_{ij}, t\right)$ is the volume fraction of liquid.

$$F\left(\Omega_{ij}, t\right) = \frac{\int_{\Omega_{ij}} c\left(\mathbf{x}\right) dV}{V_{ij}} \tag{5.18}$$

where V_{ij} the volume of the grid-cell Ω_{ij}.

The scalar function $F\left(\Omega_{ij}, t\right)$ takes a value of 0 in a gas cell, 1 when a cell is filled by liquid, and in-between $0 < F\left(\Omega_{ij}, t\right) < 1$ if an interface exists. Moreover, $F\left(\Omega_{ij}, t\right)$ is a discontinuous function since its value jumps from 0 to 1 when the argument moves from gas to liquid.

From the following connection between the mass density and the color function

$$\rho\left(\mathbf{x}\right) = \rho_l c\left(\mathbf{x}\right) + \rho_g\left(1 - c\left(\mathbf{x}\right)\right) \tag{5.19}$$

combined with (5.1b), one can easily derive the transport equation of the color function c as

$$\frac{\partial c}{\partial t} + \left(\mathbf{U} \cdot \nabla\right) c = 0 \tag{5.20}$$

5.4.3 *Coupled level-set, volume-of-fluid method*

Although the level-set function gives precisely interface position and geometries parameters, its main drawback is the mass loss (or gain) in under-resolved regions. In contrast, the volume-of-fluid is mass-conserving but unable to easily describe the liquid-gas interface. A coupled level-set, volume-of-fluid method (Sussman & Puckett 2000 [88], Ménard et al. 2007 [60] for instance) is thus integrated in ARCHER^{TM}. It consists of three principal elements.

Element 1 The use of the piecewise linear interface calculation (PLIC) method (Lopez et al. 2005 [55]) is the first element. In each cell, the interface is approximated by a planar surface. Its normal vector is easily computed from the level-set function. Then, the liquid-gas surface, originally put at the cell center, is translated so as the liquid volume fraction that it determines is equal to $F\left(\Omega_{ij}, t\right)$. The adjusted value of the distance is set to be $\phi\left(\Omega_{ij}, t\right)$.

Element 2 The second element is the transport of ϕ and F. Let's consider the transport of ϕ by re-writing (5.14) in 2D.

$$\frac{\partial \phi}{\partial t} + \frac{\partial u\phi}{\partial x} + \frac{\partial v\phi}{\partial y} = 0 \tag{5.21}$$

The Strang splitting algorithm, with improvements in Puckett et al. 1997 [75] and Sussman & Puckett 2000 [88], avoids the transport of the same volume in both directions.

$$\frac{\partial \phi}{\partial t} + \frac{\partial u\phi}{\partial x} = \phi \frac{\partial u}{\partial x} \tag{5.22a}$$

$$\frac{\partial \phi}{\partial t} + \frac{\partial v\phi}{\partial y} = \phi \frac{\partial v}{\partial y} \tag{5.22b}$$

One resolves (5.22a) explicitly for the transport in $x-$direction.

$$\widetilde{\phi}_{ij} = \frac{\phi^n_{ij} + \frac{\Delta t}{\Delta x}\left(G^{\phi}_{i-\frac{1}{2}j} - G^{\phi}_{i+\frac{1}{2}j}\right)}{1 - \frac{\Delta t}{\Delta x}\left(u_{i+\frac{1}{2}j} - u_{i-\frac{1}{2}j}\right)} \tag{5.23}$$

where $G^{\phi}_{i-\frac{1}{2}j}$, for example, is the flux from the left face of the grid-cell Ω_{ij} which is left for the upcoming paragraph.

Then (5.22b) is considered implicitly in $y-$direction.

$$\widehat{\phi}_{ij} = \frac{\widetilde{\phi}_{ij} + \frac{\Delta t}{\Delta y}\left(\widetilde{G}^{\phi}_{i-\frac{1}{2}j} - \widetilde{G}^{\phi}_{i+\frac{1}{2}j}\right)}{1 - \frac{\Delta t}{\Delta y}\left(v_{ij+\frac{1}{2}} - v_{ij-\frac{1}{2}}\right)} \tag{5.24}$$

The level-set in the next time step becomes

$$\phi^{n+1}_{ij} = \widehat{\phi}_{ij} - \widetilde{\phi}_{ij}\frac{\Delta t}{\Delta x}\left(u_{i+\frac{1}{2}j} - u_{i-\frac{1}{2}j}\right) - \widehat{\phi}_{ij}\frac{\Delta t}{\Delta y}\left(v_{ij+\frac{1}{2}} - v_{ij-\frac{1}{2}}\right) \tag{5.25}$$

The algorithm is valid for zero-divergence velocity fields (Sussman & Puckett 2000 [88]). The direction switch is necessary to obtain second-order accuracy (Pilliod et al. 2004 [72]).

We now turn to the transport of F. Re-write (5.20) in a control volume Ω_{ij}, as suggested by Weymouth & Yue 2010 [102].

$$\frac{\partial}{\partial t}\int_{\Omega_{ij}} c\,dV + \int_{\Omega_{ij}} \left(\nabla\cdot(c\mathbf{U}) - c\nabla\cdot\mathbf{U}\right) dV = 0 \tag{5.26}$$

With help of the Ostrograski-Gauss theorem, we have

$$\frac{\partial}{\partial t}\int_{\Omega_{ij}} c\,dV + \oint_{\Gamma_{ij}} c\mathbf{U}\cdot\mathbf{n}\,dS = \int_{\Omega_{ij}} c\nabla\cdot\mathbf{U}\,dV \tag{5.27}$$

where Γ_{ij} is the surface of Ω_{ij}.

Hence, the transport equation of the volume-of-fluid function F is

$$\frac{\partial F\left(\Omega_{ij},t\right)}{\partial t}V_{ij} + G^{F}_{net} = \int_{\Omega_{ij}} c\nabla\cdot\mathbf{U}\,dV = \int_{\Gamma_{ij}} c\mathbf{U}\cdot\mathbf{n}\,dS \tag{5.28}$$

where G^{F}_{net} is the net flux of liquid out of the grid-cell Ω_{ij}.

The split version of (5.28) is written as

$$\Delta F'_{ij}\frac{V_{ij}}{\Delta t} \equiv \left(F'_{ij} - F^{n}_{ij}\right)\frac{V_{ij}}{\Delta t} = G^{F}_{i+\frac{1}{2}j} - G^{F}_{i-\frac{1}{2}j} + \int_{\Gamma_{ij}} c^{n}u\,dy \tag{5.29a}$$

$$\Delta F''_{ij}\frac{V_{ij}}{\Delta t} \equiv \left(F^{n+1}_{ij} - F'_{ij}\right)\frac{V_{ij}}{\Delta t} = G^{F'}_{ij+\frac{1}{2}} - G^{F'}_{ij-\frac{1}{2}} + \int_{\Gamma_{ij}} c^{n}v\,dx \tag{5.29b}$$

where $G^{F}_{i-\frac{1}{2}j}$, for example, is the flux from the left face of the grid-cell Ω_{ij}. Its calculation is discussed in the next paragraph. The integrals are approximated as

$$\int_{\Gamma_{ij}} cu\,dy \cong c_{ij}\Delta y\left(u_{i+\frac{1}{2}j} - u_{i-\frac{1}{2}j}\right) \tag{5.30a}$$

$$\int_{\Gamma_{ij}} cv\,dx \cong c_{ij}\Delta x\left(v_{ij+\frac{1}{2}} - v_{ij-\frac{1}{2}}\right) \tag{5.30b}$$

where c_{ij} is the cell center value of the color function c.

$$c_{ij} = \begin{cases} 0 & \text{if } F\left(\Omega_{ij},t\right) < 0.5 \\ 1 & \text{otherwise} \end{cases} \tag{5.31}$$

Element 3 The third element in the coupled level-set, volume-of-fluid method of ARCHER^{TM} is the flux calculation. The flux $G^{\phi}_{i-\frac{1}{2}j}$ in (5.23), for example, is calculated by

$$G^{\phi}_{i-\frac{1}{2}j} = \phi_{i-\frac{1}{2}j} u_{i-\frac{1}{2}j} \tag{5.32}$$

where $\phi_{i-\frac{1}{2}j}$ is deduced from the following interpolation.

$$\phi_{i-\frac{1}{2}j} = \begin{cases} \phi^n_{ij} + \frac{\Delta x}{\Delta t}\left(1 - u_{i-\frac{1}{2}j}\frac{\Delta t}{\Delta x}\right)\frac{\phi^n_{ij} - \phi^n_{i-2j}}{2\Delta x} & \text{if } u_{i-\frac{1}{2}j} > 0 \\ \phi^n_{ij} + \frac{\Delta x}{\Delta t}\left(1 + u_{i-\frac{1}{2}j}\frac{\Delta t}{\Delta x}\right)\frac{\phi^n_{i+1j} - \phi^n_{i-1j}}{2\Delta x} & \text{if } u_{i-\frac{1}{2}j} < 0 \end{cases} \tag{5.33}$$

We employ the open source VOFTOOLS^{TM} (Lopez & Hernandez 2008 [54]) to derive fluid volume to be transported. For illustration purpose, let's consider the flux $G^{F}_{i-\frac{1}{2}j}$ in (5.29a) which is deduced from the liquid volume in the adjacent cell on the left when $u_{i-\frac{1}{2}j} > 0$ (Fig. 5.3). In the liquid region of the cell $i-1j$ (spotted surface), only the part limited by the dotted rectangular is taken into account. Its area equals A while the rectangular measures $\Delta y \times u_{i-\frac{1}{2}j}\Delta t$ where Δy is the spatial resolution in $y-$axis and $u_{i-\frac{1}{2}j}\Delta t$ corresponds to the travelling path of a fluid particle of a velocity $u_{i-\frac{1}{2}j}$ during a time interval Δt. The flux $G^{F}_{i-\frac{1}{2}j}$ is hence given by

$$G^{F}_{i-\frac{1}{2}j} = \Delta y \times u_{i-\frac{1}{2}j}\left(\frac{A}{|\Delta y \times u_{i-\frac{1}{2}j}\Delta t|}\right) \tag{5.34}$$

VOFTOOLS^{TM} provides the value of the dimensionless term inside the brackets.

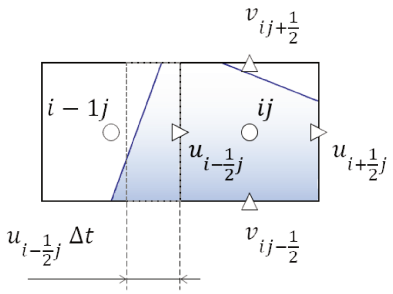

Figure 5.3: Calculation of the flux from the left-hand-side face

5.5.1 *Representation of the solid frontier by a coupled level-set, volume-of-fluid method*

Within a computational domain having irregular solid boundaries, much attention needs to be paid to the solid frontier tracking. Like the liquid-gas interface, the CLSVOF method is in operation to reconstitute the solid borderline. The latter is represented implicitly by the zero-contour of the level-set function $\phi_s(\mathbf{x}, t)$. And the marker function $F_s(\Omega_{ij}, t)$ is defined by the solid volume fraction in a grid-cell Ω_{ij}.

5.5.2 *Fluid-fraction function over cell face*

Related to the solid frontier tracking, the fluid fraction function θ is indispensable for later calculations. θ is defined as the aperture opened for the fluid to enter or leave a grid-cell. Its value is equal to the ratio between the fluid portion over a cell face and the cell face area (Fig. 5.4). Below is the approximation of the fluid fraction over the left face of the grid-cell in 2D. One can of course effortlessly derive θ for the other faces of the cell.

$$\theta_{i+\frac{1}{2}j} = \frac{|\phi_s^B|}{|\phi_s^A| + |\phi_s^B|} \tag{5.35}$$

where ϕ_s^A and ϕ_s^B the level-set function of the solid at A and B, respectively.

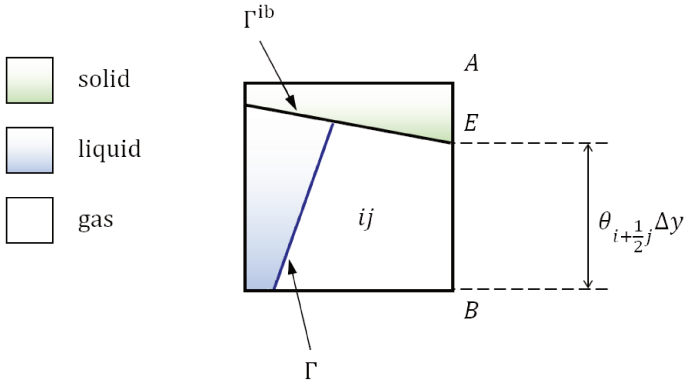

Figure 5.4: Fluid-fraction function over cell face

Up to now, we have outlined the principal steps of a typical numerical simulation of a two-phase flow with irregular solid boundaries. In the next sections, detailed calculations will be displayed, especially those concerning the numerical schemes to approximate the convection and diffusion terms, the resolution of the Poisson equation and the transport of the liquid-gas interface inside the cut-cells, i.e. the grid-cells intersected by the solid frontier. As previously stated, it depends on which immersed boundary method is in use. In § 5.6, the finite difference method is first presented (Ng et al. 2009 [65], Gibou & Min 2012 [38], Lepilliez et al. 2015 [52] for instance). Next, in § 5.7 we adapt the finite volume method (Verstappen & Veldman 2003 [100], Cheny & Botella 2010 [10] among others) for two-phase flows with irregular boundaries.

This section is dedicated to the finite difference method (Ng et al. 2009 [65], Gibou & Min 2012 [38], Lepilliez et al. 2015 [52] for instance) to complete our simulation, i.e. approximating the convection and diffusion terms, solving the Poisson equation and moving the liquid-gas interface inside the cut-cells.

5.6.1 *Discretization of irregular domains*

In the framework of the finite difference method, scalar variables such as the pressure, the level-set and volume-of-fluid functions are stored at the cell centre. We sample x and y-components of the velocity on the vertical and horizontal faces, respectively. An example of a cut-cell $\Omega_{ij} = \left[i - \frac{1}{2}, i + \frac{1}{2}\right] \times \left[j - \frac{1}{2}, j + \frac{1}{2}\right]$ partially covered by the fluid is plotted in Fig. 5.5.

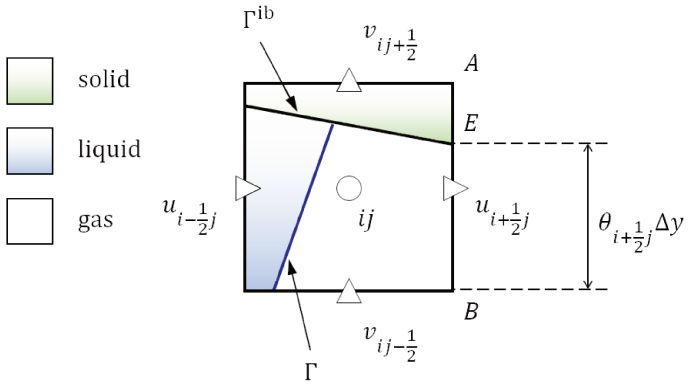

Figure 5.5: A cut-cell in a standard MAC grid configuration – Finite difference method

5.6.2 *Approximation of the convection term*

The convection term $(\mathbf{U}^n \cdot \nabla)\,\rho^n \mathbf{U}^n$ can be approximated by the 5^{th} order weighted essentially non-oscillatory (WENO) scheme. Alternatively, it is first written as $\nabla \cdot (\rho^n \mathbf{U}^n \mathbf{U}^n)$ before being calculated a method guaranteeing the consistence between the transport of mass and momentum in two-phase flows (Rudman 1998

[81], Vaudor et al. 2017 [99] for instance). The second approach is justified especially when the ratio between the liquid and gas mass density is high.

5.6.3 *Implicit treatment of the diffusion term*

As written in § 5.3, to enforce the no-slip condition even for the intermediate velocity, the diffusion term is implicitly treated (Sussman et al. 1999 [90], Gibou et al. 2002 [39], Lepilliez et al. 2015 [52] for instance). In effect, the intermediate velocity $\mathbf{U}^*$ is updated by (5.7) that we re-write below.

$$\mathbf{U}^* = \mathbf{U}^n - \frac{\Delta t}{\rho^{n+1}}\left[(\mathbf{U}^n \cdot \nabla)\,\rho^n \mathbf{U}^n + \nabla \cdot \left(2\mu^{n+1}\mathbf{D}^*\right) + \sigma\kappa^{n+1}\mathbf{n}\delta_\Gamma\right] \tag{5.36}$$

The pressure jump $\sigma\kappa^{n+1}\mathbf{n}\delta_\Gamma$ is treated using the ghost fluid method (Fedkiw et al. 1999 [36], Liu et al. 2000 [53], Tanguy 2004 [93], Ménard 2007 [59], Lepilliez et al. 2015 [52] for instance). (5.36) is solved at each time step to obtain the intermediate velocity $\mathbf{U}^*$. For a better readability we ignore the superscript * in the following formulae although the latter are written for the intermediate velocity $\mathbf{U}^*$. Consider a 2D configuration, for simplicity. The viscous tensor can be expressed as

$$2\mu(\phi)\,\mathbf{D} = \begin{pmatrix} 2\mu(\phi)\,\frac{\partial u}{\partial x} & \mu(\phi)\left(\frac{\partial v}{\partial x} + \frac{\partial u}{\partial y}\right) \\ \mu(\phi)\left(\frac{\partial v}{\partial x} + \frac{\partial u}{\partial y}\right) & 2\mu(\phi)\,\frac{\partial v}{\partial y} \end{pmatrix} \tag{5.37}$$

The projection in x-direction of the viscous term $\nabla \cdot (2\mu\mathbf{D})$ in (5.36) is estimated at point $i + \frac{1}{2}j$ (5.38). Its projection in y-direction at point $ij + \frac{1}{2}$ is alike.

$$\begin{aligned}(\nabla \cdot (2\mu\mathbf{D})) \cdot \mathbf{e}_x|_{i+\frac{1}{2}j} = &\frac{\partial}{\partial x}\left(2\mu(\phi)\,\frac{\partial u}{\partial x}\right)\Bigg|_{i+\frac{1}{2}j} + \\ &\frac{\partial}{\partial y}\left(\mu(\phi)\left(\frac{\partial u}{\partial y} + \frac{\partial v}{\partial x}\right)\right)\Bigg|_{i+\frac{1}{2}j}\end{aligned} \tag{5.38}$$

(5.38) is discretized by adopting Sussman et al. 1999 [90], Vaudor 2015 [98] among others as follows. Remark that the diffusion term is computed with help of the level-set method in the framework of two phase flows.

$$
\begin{aligned}
(\nabla \cdot (2\ \mu\ \mathbf{D})) \cdot \mathbf{e}_x|_{i+\frac{1}{2}j} \approx & \\
& \frac{2\mu(\phi)_{i+1j}\left(\frac{\partial u}{\partial x}\right)\big|_{i+1j} - 2\mu(\phi)_{ij}\left(\frac{\partial u}{\partial x}\right)\big|_{ij}}{\Delta x} \\
& + \frac{\mu(\phi)_{i+\frac{1}{2}j+\frac{1}{2}}\left(\frac{\partial u}{\partial y}\right)\Big|_{i+\frac{1}{2}j+\frac{1}{2}} - \mu(\phi)_{i+\frac{1}{2}j-\frac{1}{2}}\left(\frac{\partial u}{\partial y}\right)\Big|_{i+\frac{1}{2}j-\frac{1}{2}}}{\Delta y} \\
& + \frac{\mu(\phi)_{i+\frac{1}{2}j+\frac{1}{2}}\left(\frac{\partial v}{\partial x}\right)\big|_{i+\frac{1}{2}j+\frac{1}{2}} - \mu(\phi)_{i+\frac{1}{2}j-\frac{1}{2}}\left(\frac{\partial v}{\partial x}\right)\big|_{i+\frac{1}{2}j-\frac{1}{2}}}{\Delta y} \\
& \approx \frac{2\mu(\phi)_{i+1j}\left(\frac{u_{i+\frac{3}{2}j} - u_{i+\frac{1}{2}j}}{\Delta x}\right) - 2\mu(\phi)_{ij}\left(\frac{u_{i+\frac{1}{2}j} - u_{i-\frac{1}{2}j}}{\Delta x}\right)}{\Delta x} \\
& + \frac{\mu(\phi)_{i+\frac{1}{2}j+\frac{1}{2}}\left(\frac{u_{i+\frac{1}{2}j+1} - u_{i+\frac{1}{2}j}}{\Delta y}\right) - \mu(\phi)_{i+\frac{1}{2}j-\frac{1}{2}}\left(\frac{u_{i+\frac{1}{2}j} - u_{i+\frac{1}{2}j-1}}{\Delta y}\right)}{\Delta y} \\
& + \frac{\mu(\phi)_{i+\frac{1}{2}j+\frac{1}{2}}\left(\frac{v_{i+1j+\frac{1}{2}} - v_{ij+\frac{1}{2}}}{\Delta x}\right) - \mu(\phi)_{i+\frac{1}{2}j-\frac{1}{2}}\left(\frac{v_{i+1j-\frac{1}{2}} - v_{ij-\frac{1}{2}}}{\Delta x}\right)}{\Delta y}
\end{aligned}
\tag{5.39}
$$

where

$$
\mu(\phi)_{ij} = \frac{\mu_g \mu_l}{\mu_g \xi(\phi)_{ij} + \mu_l\left(1 - \xi(\phi)_{ij}\right)}
$$

with

$$
\xi(\phi)_{ij} = \begin{cases} 0 & \text{if } \phi_{i-\frac{1}{2}j} < 0 \text{ and } \phi_{i+\frac{1}{2}j} < 0 \\ 1 & \text{if } \phi_{i-\frac{1}{2}j} > 0 \text{ and } \phi_{i+\frac{1}{2}j} > 0 \\ \frac{\phi^+_{i-\frac{1}{2}j} + \phi^+_{i+\frac{1}{2}j}}{|\phi_{ij}| + |\phi_{i+1j}|} & \text{otherwise} \end{cases}
$$

$$
a^+ = \max(0, a)
$$

$$
\phi_{i-\frac{1}{2}j} = \frac{\phi_{i-1j} + \phi_{ij}}{2}
$$

$$
\phi_{i+\frac{1}{2}j} = \frac{\phi_{ij} + \phi_{i+1j}}{2}
$$

and

$$\mu(\phi)_{i+\frac{1}{2}j+\frac{1}{2}} = \frac{\mu_g \mu_l}{\mu_g \xi(\phi)_{i+\frac{1}{2}j+\frac{1}{2}} + \mu_l \left(1 - \xi(\phi)_{i+\frac{1}{2}j+\frac{1}{2}}\right)}$$

with

$$\xi(\phi)_{i+\frac{1}{2}j+\frac{1}{2}} = \begin{cases} 0 & \text{if } \phi_{ij} < 0,\ \phi_{i+1j} < 0,\ \phi_{ij+1} < 0,\ \phi_{i+1j+1} < 0 \\ 1 & \text{if } \phi_{ij} > 0,\ \phi_{i+1j} > 0,\ \phi_{ij+1} > 0,\ \phi_{i+1j+1} > 0 \\ \frac{\phi^+_{ij}+\phi^+_{i+1j}+\phi^+_{ij+1}+\phi^+_{i+1j+1}}{|\phi^+_{ij}|+|\phi^+_{i+1j}|+|\phi^+_{ij+1}|+|\phi^+_{i+1j+1}|} & \text{otherwise} \end{cases}$$

When the solid boundaries are present, the method suggested by Gibou et al. 2002 [39], Lepilliez 2015 [52] is applied to discretize each term in (5.39). Take $\frac{\partial u}{\partial x}\big|_{ij}$ as example. Three cases can be distinguished when discretize the term.

Case 1 If $\phi^s_{i+\frac{1}{2}j} < 0$ and $\phi^s_{i-\frac{1}{2}j} < 0$, the cell $\left[i-\frac{1}{2}, i+\frac{1}{2}\right] \times [j]$ is entirely covered by the fluid. Thus, the approximation is

$$\left.\frac{\partial u}{\partial x}\right|_{ij} = \frac{u_{i+\frac{1}{2}j} - u_{i-\frac{1}{2}j}}{\Delta x}$$

Case 2 If $\phi^s_{i+\frac{1}{2}j} > 0$ and $\phi^s_{i-\frac{1}{2}j} < 0$, the cell point $(i+\frac{1}{2}j)$ is in the solid and the cell point $(i-\frac{1}{2}j)$ is in the fluid, so we have

$$u_{i+\frac{1}{2}j} = 0$$

Case 3 If $\phi^s_{i+\frac{1}{2}j} < 0$ and $\phi^s_{i-\frac{1}{2}j} > 0$, the cell point $(i+\frac{1}{2}j)$ is in the fluid and the cell point $(i-\frac{1}{2}j)$ is in the solid. We approximate the derivative by

$$\left.\frac{\partial u}{\partial x}\right|_{ij} = \frac{u_{i+\frac{1}{2}j}}{\theta \Delta x}$$

where $\theta\Delta x$ the length of the cell covered by the fluid. Hence

$$\theta = \frac{|\phi^s_{i+\frac{1}{2}j}|}{|\phi^s_{i+\frac{1}{2}j}| + |\phi^s_{i-\frac{1}{2}j}|}$$

Finally, we obtain a system of linear equations involving three velocity components localized at the center of the cell faces. It should be reminded that these variables are the components of the intermediate velocity $\mathbf{U}^*$ and the superscript * is removed to improve the readability. The left-hand side of (5.36) is a 9-diagonal matrix per velocity component, which becomes a 15-diagonal matrix per velocity component in 3D. The linear system is solved by the Gauss-Seidel algorithm.

5.6.4 *Discretization of the pressure Poisson equation on irregular domains*

With the discretized convection and diffusion terms available, $\mathbf{U}^*$ is known from (5.7), allowing the Poisson equation (5.9) for pressure can be solved. Ng et al. 2009 [65], Gibou & Min 2012 [38], Lepilliez et al. 2015 [52] discretize (5.9) for all grid-cells, even for the cut-cells where the Neumann condition is satisfied.

By a finite volume approach, let's integrate the left-hand side of (5.9) and apply the divergence theorem.

$$\oiint_{\Omega_{ij}\cup\Omega_f} \nabla\cdot\left(\frac{\nabla p}{\rho}\right) dA = \oint_{\partial(\Omega_{ij}\cup\Omega_f)} \mathbf{n}\cdot\left(\frac{\nabla p}{\rho}\right) dl \tag{5.40}$$

with dA and dl are the differential area and length, respectively. Likewise, for the right-hand side of (5.9), we have

$$\oiint_{\Omega_{ij}\cup\Omega_f} \nabla\cdot\mathbf{U}^* dA = \oint_{\partial(\Omega_{ij}\cup\Omega_f)} \mathbf{n}\cdot\mathbf{U}^* dl \tag{5.41}$$

To estimate each component of $\partial\left(\Omega_{ij} \cap \Omega_f\right)$ in (5.40) and (5.41), the fluid fraction function θ is required. Simply, θ is the ratio between the fluid portion over a cell face and the cell face area (Fig. 5.5). Refer to § 5.5.2 for its approximation. We obtain

$$
\begin{aligned}
-\oint_{\partial(\Omega_{ij}\cup\Omega_f)} \mathbf{n}\cdot\left(\frac{\nabla p}{\rho}\right) dl \approx -\boxed{\oint_{\Gamma^{ib}\cup\Omega_f} \mathbf{n}\cdot\left(\frac{\nabla p}{\rho}\right) dl} \\
+\frac{\theta^u_{i-\frac{1}{2}j}}{\rho_{i-\frac{1}{2}j}}\left(\frac{p_{ij}-p_{i-1j}}{\Delta x}\right)+\frac{\theta^u_{i+\frac{1}{2}j}}{\rho_{i+\frac{1}{2}j}}\left(\frac{p_{ij}-p_{i+1j}}{\Delta x}\right) \\
+\frac{\theta^v_{ij-\frac{1}{2}}}{\rho_{ij-\frac{1}{2}}}\left(\frac{p_{ij}-p_{ij-1}}{\Delta y}\right)+\frac{\theta^v_{ij+\frac{1}{2}}}{\rho_{ij+\frac{1}{2}}}\left(\frac{p_{ij}-p_{ij+1}}{\Delta y}\right)
\end{aligned}
\tag{5.42}
$$

where $\rho_{i-\frac{1}{2}j}$, for example, is the mass density of the volume which consists of the left half of the grid-cell Ω_{ij} and the right half of the grid-cell Ω_{i-1j}.

Similarly,

$$
\begin{aligned}
-\oint_{\partial(\Omega_{ij}\cup\Omega_f)} \mathbf{n}\cdot\mathbf{U}^* dl = -\boxed{\oint_{\Gamma^{ib}\cup\Omega_f} \mathbf{n}\cdot\mathbf{U}^* dl} \\
+\theta^u_{i-\frac{1}{2}j}u^*_{i-\frac{1}{2}j}-\theta^u_{i+\frac{1}{2}j}u^*_{i+\frac{1}{2}j} \\
+\theta^v_{ij-\frac{1}{2}}v^*_{ij-\frac{1}{2}}-\theta^v_{ij+\frac{1}{2}}v^*_{ij+\frac{1}{2}}
\end{aligned}
\tag{5.43}
$$

We combine (5.42) and (5.43) and use the Neumann condition (5.10) to simplify the terms in boxes.

$$
\begin{aligned}
&\frac{\theta^u_{i-\frac{1}{2}j}}{\rho_{i-\frac{1}{2}j}}\left(\frac{p_{ij}-p_{i-1j}}{\Delta x}\right)+\frac{\theta^u_{i+\frac{1}{2}j}}{\rho_{i+\frac{1}{2}j}}\left(\frac{p_{ij}-p_{i+1j}}{\Delta x}\right)+ \\
&\frac{\theta^v_{ij-\frac{1}{2}}}{\rho_{ij-\frac{1}{2}}}\left(\frac{p_{ij}-p_{ij-1}}{\Delta y}\right)+\frac{\theta^v_{ij+\frac{1}{2}}}{\rho_{ij+\frac{1}{2}}}\left(\frac{p_{ij}-p_{ij+1}}{\Delta y}\right)= \\
&\qquad\qquad \theta^u_{i-\frac{1}{2}j}u^*_{i-\frac{1}{2}j}-\theta^u_{i+\frac{1}{2}j}u^*_{i+\frac{1}{2}j} \\
&\qquad\qquad +\theta^v_{ij-\frac{1}{2}}v^*_{ij-\frac{1}{2}}-\theta^v_{ij+\frac{1}{2}}v^*_{ij+\frac{1}{2}}
\end{aligned}
\tag{5.44}
$$

According to Ng et al. 2009 [65], Gibou & Min 2012 [38], Lepilliez et al. 2015 [52], the above linear system is symmetric positive definite and therefore can be inverted efficiently by classical methods.

5.6.5 *Contact angle*

Section § 5.6.3 points out that the surface tension term needs to be discretized (5.36) to deduce the intermediate velocity field. When both fluid interface and wall boundaries are found in the same cell, a contact angle, which is the angle between Γ and Γ^{ib}, is enforced to calculate the value the level-set function inside the cut-cells and in the solid media in order to know $\mathbf{n}_\Gamma$ and κ. In addition, in § 5.6.6, the level-set function is extrapolated inside the cut-cells to transport the liquid-gas interface. Within this purpose, we extrapolate the level-set function ϕ into not only the cut-cells but also the solid media, thus impose its gradient. The extension procedure is conducted as follows. When the equilibrium state is reached, a static contact angle θ_c is enforced to obtain a Neumann boundary condition on the fluid level-set function.

$$\mathbf{n}^{ib} \cdot \nabla\phi = \cos(\theta_c) \tag{5.45}$$

θ_c depends on the interactions between the fluid flow and the solid wall and is supposed to be known *a priori*. The multidimensional extrapolation proposed in Aslam 2004 [2] allows to extend ϕ into the solid and to impose a gradient of ϕ near the solid boundary, i.e. to fulfil the condition (5.45).

$$\frac{\partial\phi}{\partial\tau} + H(\phi_s)\,\mathbf{n}_s \cdot \nabla\phi = \cos(\theta_c) \tag{5.46}$$

where τ a fictitious time step and $H(\phi_s)$ a Heaviside function. (5.46) is applied only on solid cells. We implement a 3^{rd} order Total Variation Diminishing (TVD) Runge-Kutta for the temporal discretization. The gradient term is treated by a 2^{nd} order upwind scheme.

Notice that a dynamic contact angle should be imposed to account for the physics of the contact point (in 2D) or the contact line (in 3D) between the three phases. However, due to its dependence on the flow, the properties of liquid, gas and solid, modelling of dynamic contact angles is complex and thus out of the scope of our study.

5.6.6 *Transport of the liquid-gas interface inside cut-cells*

Remark that within the framework of the finite difference method, the velocity components are located in the center of the cell faces. Therefore, they do not exist when more than a half of the cell face is covered by the solid (Fig. 5.5). Two cases can be distinguished while transporting the liquid-gas interface inside the cut-cells.

When the solid covers more than a half of the cell volume, we first use (5.21) to transport only the level-set function inside the grid-cells which are adjacent to the cut-cells. After that, the level-set function is then extrapolated to the cut-cells following Aslam 2004 [2] (refer to § 5.6.5). Finally, the value of the volume-of-fluid function inside the cut-cells is derived from the level-set function thanks to the open source VOFTOOLS^{TM} (Lopez & Hernandez 2008 [54]).

On the other hand, when the solid covers less than a half of the cell volume, the volume-of-fluid function is transported as usual.

5.7 IMMERSED BOUNDARY METHOD FOR TWO-PHASE FLOWS FINITE VOLUME METHOD

The essential feature of the immersed boundary method presented within the framework of the finite difference method in the previous section is the implicit resolution of the diffusion term to ensure the no-slip boundary condition on the solid frontier as well as the symmetric, positive and definite discretization of the Poisson equation able to be rapidly solved by the classical methods. However, while transporting the liquid-gas interface inside the cut-cells in $x-$direction, for example, the color function or the volume-of-fluid function can not be moved by the velocity component u if the center of the cell face which contains u is located inside the solid region. As mentioned above, in this case, the level-set function of the adjacent cells is first transported as usual. Then, the level-set value of the cut-cell is derived from the Aslam's extrapolation. And finally, the color function and the volume-of-fluid function inside the cut-cell is computed from the level-set value.

To enable the transport of the liquid-gas interface inside the cut-cells and more importantly, to ensure good conservation properties of the numerical schemes, we adopted the immersed boundary method introduced in Verstappen & Veldman 2003 [100], Cheny & Botella 2010 [10] among others. Note that unlike the last section where the finite difference method is used for discretizing the Navier-Stokes, the finite volume approach of Cheny & Botella 2010 [10] is faithfully presented here, with some modifications for two-phase flows with irregular solid boundaries. It should be underlined that we also cite concerning papers as do Cheny & Botella 2010 [10] in their article.

5.7.1 *Discretization of irregular domains*

While applying the finite volume method, scalar variables, i.e. the pressure, the level-set and volume-of-fluid functions are stored everywhere inside the grid-cell. x and y-components of the velocity are respectively sampled in the center of the fluid part of the vertical and horizontal faces. Only one part of the cut-cell $\Omega_{ij} = \left[i-\frac{1}{2}, i+\frac{1}{2}\right] \times \left[j-\frac{1}{2}, j+\frac{1}{2}\right]$ is covered by the fluid, as shown in Fig. 5.6.

To model a fluid flow in the computational domain Ω enclosed by a surface Γ (Fig. 5.1) by the finite volume method, one makes approximations of the incompressible Navier-Stokes equations in integral form. Remember that for an arbitrary control volume Ω_{ij} with its surface Γ_{ij}, the finite-volume discretization of the continuity equation writes

$$\int_{\Omega_{ij}} \nabla \cdot \mathbf{U} dV = \int_{\Gamma_{ij}} \mathbf{U} \cdot \mathbf{n} dS = 0 \tag{5.47}$$

And that of the momentum equations in the x- and y-directions is

$$\begin{aligned} \frac{d}{dt}\int_{\Omega_{ij}} \rho u dV = &- \int_{\Gamma_{ij}} (\mathbf{U}\cdot\mathbf{n})\,\rho u dS + \int_{\Gamma_{ij}} 2\mu \mathbf{D}\ \mathbf{e}_x \cdot \mathbf{n} dS \\ &- \int_{\Gamma_{ij}} p\mathbf{e}_x \cdot \mathbf{n} dS + \int_{\Omega_{ij}} \delta_\Gamma \sigma\kappa\ \mathbf{n}_\Gamma \cdot \mathbf{e}_x dV \end{aligned} \tag{5.48a}$$

$$\begin{aligned} \frac{d}{dt}\int_{\Omega_{ij}} \rho v dV = &- \int_{\Gamma_{ij}} (\mathbf{U}\cdot\mathbf{n})\,\rho v dS + \int_{\Gamma_{ij}} 2\mu \mathbf{D}\ \mathbf{e}_y \cdot \mathbf{n} dS \\ &- \int_{\Gamma_{ij}} p\mathbf{e}_y \cdot \mathbf{n} dS + \int_{\Omega_{ij}} \delta_\Gamma \sigma\kappa\ \mathbf{n}_\Gamma \cdot \mathbf{e}_y dV \end{aligned} \tag{5.48b}$$

where $\mathbf{U} = (u, v)$ is the velocity field, p the pressure, t the time, ρ the mass density, μ the dynamic viscosity, $\mathbf{D}$ the viscous tensor (5.37), σ the surface tension coefficient and κ the liquid-gas interface local mean curvature. Remark that $\delta_\Gamma \mathbf{n}_\Gamma$ can be replaced by ∇F where F the volume-of-fluid function.

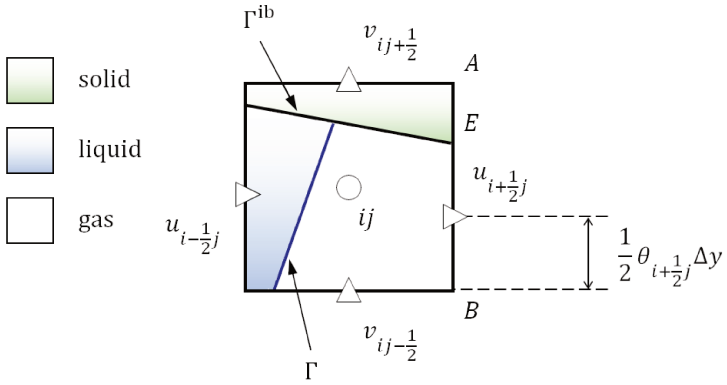

Figure 5.6: A cut-cell in a standard MAC grid configuration – Finite volume method

5.7.3 *Discretization for fixed immersed geometries*

5.7.3.1 *Global conservation laws for viscous incompressible flows*

Solving any flow problem consists firstly in using numerical schemes to approximate continuous fluid dynamics equations. It is required that the former should conserve the invariants of the latter to physically represent the flow (Arakawa 1966 [1]). To put it more precisely, three invariants are present in (5.47) and (5.48).

- the total mass $\int_{\Omega_f} \nabla \cdot \mathbf{U} dV$;
- the total momentum $\mathbf{P}(t) = \int_{\Omega_f} \rho \mathbf{U} dV$;
- and the kinetic energy $E_c(t) = \int_{\Omega_f} \frac{\rho |\mathbf{U}|^2}{2} dV$ in the limit of one-phase inviscid fluid flows.

The conservation equations of these invariants can be established from (5.47) and (5.48). We have for the total mass,

$$\int_{\Gamma^{ib}} \mathbf{U} \cdot \mathbf{n} dS = 0 \tag{5.49a}$$

for the total momentum,

$$\frac{d\mathbf{P}}{dt} = -\int_{\Gamma^{ib}} \rho \mathbf{U}\mathbf{U} \cdot \mathbf{n} dS - \mathbf{F} - \mathbf{F}_\Gamma^{ib} \tag{5.49b}$$

and for the kinetic energy,

$$\begin{aligned} \frac{dE_c}{dt} = & \int_{\Omega_f} \left[\left(\frac{\rho |\mathbf{U}|^2}{2} + p \right) \nabla \cdot \mathbf{U} - \mu |\nabla \mathbf{U}|^2 \right] dV \\ & + \int_{\Omega_f} \delta_\Gamma \sigma \kappa \ \mathbf{n}_\Gamma \cdot \mathbf{U} dV \\ & - \int_{\Gamma^{ib}} \left(\frac{\rho |\mathbf{U}|^2}{2} + p - \mu \nabla \mathbf{U} \right) \mathbf{U} \cdot \mathbf{n} dS \end{aligned} \tag{5.50}$$

where $\mathbf{F} = (F_x, F_y)$ are the hydrodynamic force acting on the immersed boundary

$$F_x = \int_{\Gamma^{ib}} \left[p - 2\mu \frac{\partial u}{\partial x} \right] \mathbf{e}_x \cdot \mathbf{n} dS - \int_{\Gamma^{ib}} \mu \left(\frac{\partial v}{\partial x} + \frac{\partial u}{\partial y} \right) \mathbf{e}_y \cdot \mathbf{n} dS \tag{5.51a}$$

$$F_y = \int_{\Gamma^{ib}} \left[p - 2\mu \frac{\partial v}{\partial y} \right] \mathbf{e}_y \cdot \mathbf{n} dS - \int_{\Gamma^{ib}} \mu \left(\frac{\partial u}{\partial y} + \frac{\partial v}{\partial x} \right) \mathbf{e}_x \cdot \mathbf{n} dS \tag{5.51b}$$

and $\mathbf{F}_\Gamma^{ib}$ the force representing the interactions between the liquid-gas interface and the solid wall. It is implicitly modelled by the contact angle (refer to § 5.6.5) and ignored hereafter.

In (5.50), all terms of the first volume integral except the viscous dissipation disappear because of (5.47). The total energy of the flow can thus only decrease due to viscous effects and the surface tension. Moreover, the surface integral in (5.50) can be discarded. While it expresses the influence of the pressure and convective terms on the energy budget via their action on the solid frontier only, the latter is fixed in our case.

The next subsections address the discretization of each term in (5.47) and (5.48) to verify the conditions (5.49a), (5.49b) and (5.50).

5.7.3.2 *Discretization of the continuity equation*

We are first interested in the discretization of the continuity equation (5.47) is discretized. In any fluid cell Ω_{ij} whose face is decomposed into $\Gamma_{ij} = \Gamma_{ij}^w \cup \Gamma_{ij}^e \cup \Gamma_{ij}^s \cup \Gamma_{ij}^n \cup \Gamma_{ij}^{ib}$, (5.47) can be regarded as the net fluxes through these faces (Fig. 5.7).

$$\dot{q}_{ij} \equiv -\overline{u}_{i-\frac{1}{2}j} + \overline{u}_{i+\frac{1}{2}j} - \overline{v}_{ij-\frac{1}{2}} + \overline{v}_{ij+\frac{1}{2}} = 0 \tag{5.52}$$

The face-integrated quantity $\overline{u}_{i+\frac{1}{2}j}$ through Γ_{ij}^e is related to the discrete unknown $u_{i+\frac{1}{2}j}$ at the center the fluid part of the face via the midpoint rule.

$$\overline{u}_{i+\frac{1}{2}j} \widehat{=} \theta^u_{i+\frac{1}{2}j} \Delta y \;\; u_{i+\frac{1}{2}j} \tag{5.53}$$

Similar discretization is applied for the other faces and (5.52) becomes

$$\begin{aligned} \dot{q}_{ij} \;&\equiv\; \Delta y \left(\theta^{u}_{i+\frac{1}{2}j} u_{i+\frac{1}{2}j} - \theta^{u}_{i-\frac{1}{2}j} u_{i-\frac{1}{2}j} \right) \\ &+\; \Delta x \left(\theta^{v}_{ij+\frac{1}{2}} v_{ij+\frac{1}{2}} - \theta^{v}_{ij-\frac{1}{2}} v_{ij-\frac{1}{2}} \right) \;=\; 0 \end{aligned} \tag{5.54}$$

Notice the likelihood between the divergence operator in (5.54) and that on the right-hand side of (5.44).

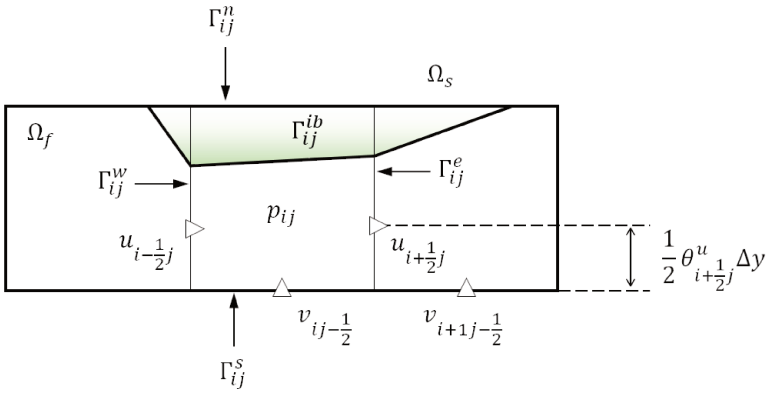

Figure 5.7: Net fluxes through cell faces

(5.54) is the discrete continuity equation and can be written in matrix form as

$$\mathcal{D}\mathcal{U} = \mathcal{O} \tag{5.55}$$

where each line (ij) of (5.55) simply corresponds to (5.54) written in Ω_{ij}. The vector $\mathcal{U}$ contains the velocity unknowns and the matrix $\mathcal{D}$ the divergence operator.

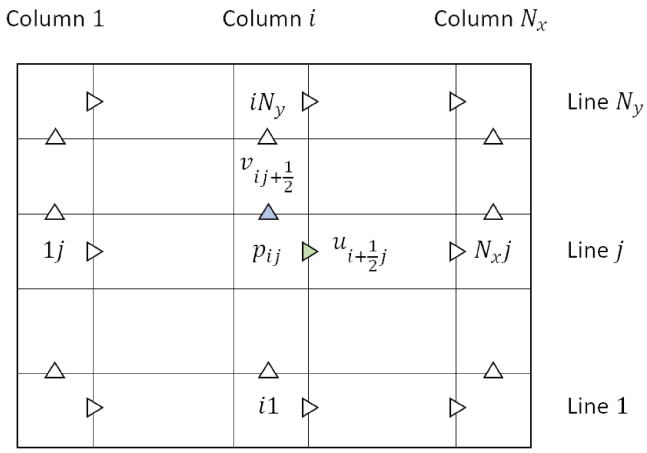

Figure 5.8: Location of the velocity components and the pressure in a standard MAC grid

Let's illustrate the arrangement of the velocity unknowns in $\mathcal{U}$ and the divergence operator in $\mathcal{D}$. Remember that in the MAC grid representation, the horizontal com-

ponent $u_{i+\frac{1}{2}j}$ and vertical component $v_{ij+\frac{1}{2}}$ of the discrete velocity are positioned respectively in the center of the right edge and the upper edge of the grid-cell Ω_{ij} (Fig. 5.8). p_{ij} is the discrete pressure everywhere inside Ω_{ij}.

Vector $\mathbb{U}$ is filled by discrete values $u_{i+\frac{1}{2}j}$ which are collected by sweeping the MAC grid in Fig. 5.8 firstly column by column and then line by line. For vector $\mathbb{V}$, one keeps the same order of the gliding operation to collect the discrete values $v_{ij+\frac{1}{2}}$. The vectors $\mathbb{U}$ and $\mathbb{V}$ can be seen in Figs. 5.9 and 5.10, respectively.

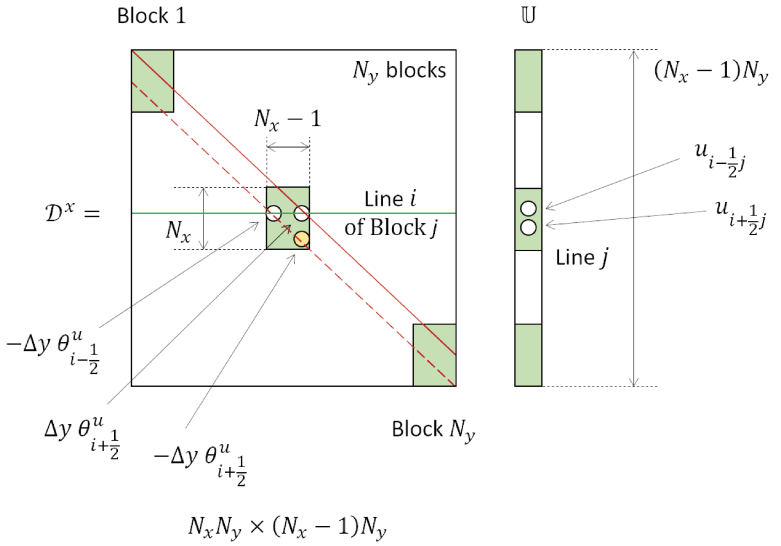

Figure 5.9: Divergence operation for x- velocity component $\mathcal{D}^x\mathbb{U}$

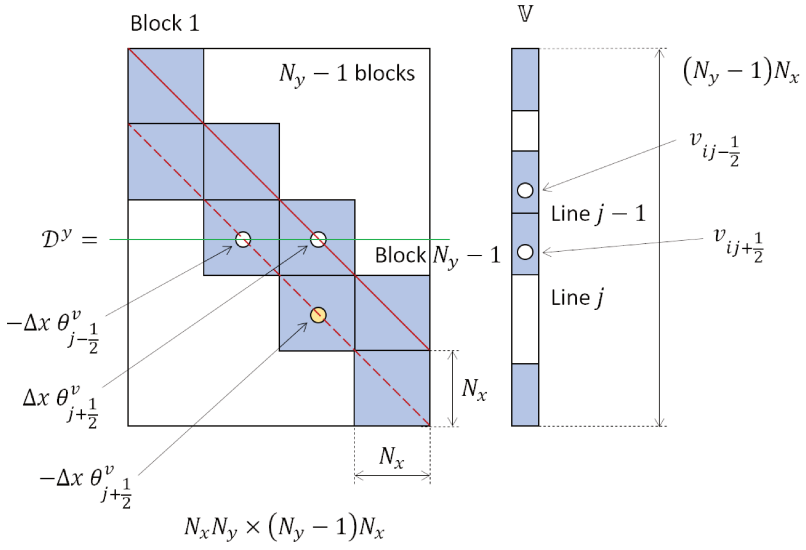

Figure 5.10: Divergence operation for y- velocity component $\mathcal{D}^y\mathbb{V}$

With the organization of vectors $\mathbb{U}$ and $\mathbb{V}$ in mind, one can transform $\mathcal{DU}$ in (5.55) into a sum of two component-wise products as

$$\mathcal{D}^x\mathbb{U} + \mathcal{D}^y\mathbb{V} = \mathcal{DU} = \mathcal{O} \tag{5.56}$$

$\mathcal{D}^x$ and $\mathcal{D}^y$ are the matrices containing the divergence operator applying in x- and y- velocity components. Both of them are sparse in which the divergence coefficients are arranged along two red lines as in Figs. 5.9 and 5.10. One can think of $\mathcal{D}^x$ as a set of blocks, counting from 1 to N_y. $\mathcal{D}^y$ has two lines of blocks numbered from 1 to $N_y - 1$. In a grid-cell ij, the two divergence coefficients for the component u result simply from the intersection of a horizontal green line along row i of block j with the two diagonal red lines, which are $-\Delta y\theta^u_{i-\frac{1}{2}j}$ and $\Delta y\theta^u_{i+\frac{1}{2}j}$. The divergence coefficients for the component v can be obtained in a similar way provided that the divergence coefficients of the discrete values $v_{ij+\frac{1}{2}}$ and $v_{ij-\frac{1}{2}}$ are located in the diagonal of block j and that of its left neighbouring, respectively. The velocity unknowns are assembled in a unique vector $\mathcal{U}$ and the divergence operator $\mathcal{D}$ is built from $\mathcal{D}^x$ and $\mathcal{D}^y$.

We now examine if the above discretization of the continuity equation conserves the total mass. Note that the discrete counterpart of the left-hand side of the total mass conservation condition (5.49a) is equivalent to the sum across all fluid cells of the discrete continuity equation (5.54).

$$\dot{q} \cong \dot{q}^h \equiv \sum_{\text{Control volumes}\ \ \Omega_{ij}} \dot{q}_{ij} \equiv \mathbb{1}^T\mathcal{DU} \tag{5.57}$$

where $\mathbb{1}^T$ is the constant vector. Thanks to (5.54), the discrete total mass is

$$\dot{q}^h \equiv \sum_{\text{Control volumes}\ \ \Omega_{ij}} \Big[\Delta y\left(\theta^u_{i+\frac{1}{2}j}u_{i+\frac{1}{2}j} - \theta^u_{i-\frac{1}{2}j}u_{i-\frac{1}{2}j}\right) + \Delta x\left(\theta^v_{ij+\frac{1}{2}}v_{ij+\frac{1}{2}} - \theta^v_{ij-\frac{1}{2}}v_{ij-\frac{1}{2}}\right)\Big]$$

By using the local conservation of the mass fluxes at fluid faces, it is easy to prove that $\dot{q}^h = 0$, meaning that the total mass is discretely conserved through the above discretization.

5.7.3.3 *Discretization of the momentum equation based on the conservation of kinetic energy – Pressure gradient and convective fluxes*

Let's turn to the discretization of the momentum equation (5.48). This is equivalent to dicretize three terms, i.e. the pressure gradient, the convective and viscous fluxes. While the task for the first two terms has to be done based on the conservation of the kinetic energy, one has to use the total momentum conservation condition to treat the third term. This subsection is intended to takes care of the pressure gradient and convection terms discretization and leaves the discretization of the diffusion term for the next part.

We begin by rewriting (5.48) in a semi-discrete matrix form.

$$\frac{d}{dt}\left(\mathcal{M}\mathcal{U}\right) = -\mathcal{C}\left[\overline{\mathcal{U}}\right]\mathcal{U} - \mathcal{G}\mathcal{P} + \mathcal{F}_\Gamma + \mathcal{K}\mathcal{U} - \mathcal{S}^{ib,c} + \mathcal{S}^{ib,\nu} \tag{5.58}$$

where $\mathcal{M}$ is the diagonal mass matrix, built from the volume of the fluid cells, $\mathcal{C}\left[\overline{\mathcal{U}}\right]$ the matrix representing the discretization of the convective fluxes, $\mathcal{G}$ the discrete pressure gradient, $\mathcal{K}$ the matrix representing the discretization of the viscous fluxes, $\mathcal{F}_\Gamma$ the pressure jump across the liquid-gas interface, $\mathcal{S}^{ib,c}$ and $\mathcal{S}^{ib,\nu}$ the source terms arising from the boundary conditions of the convective and viscous terms, respectively. These terms will be constructed such that the total momentum and kinetic energy are discretely conserved. We restrict ourselves to fixed immersed boundaries where $\mathcal{S}^{ib,c} = \mathcal{O}$ and $\mathcal{S}^{ib,\nu} = \mathcal{O}$.

The first step is to build $\mathcal{M}$. Applying the trapezoidal rule to each line of (5.58), one gets the diagonal coefficients in the horizontal and vertical directions.

$$\left[\mathcal{M}^x\right]_P\left(i+\frac{1}{2}j\right) = \frac{1}{2}\rho_{ij}V_{ij} + \frac{1}{2}\rho_{i+1j}V_{i+1j} \tag{5.59a}$$

$$\left[\mathcal{M}^y\right]_P\left(ij+\frac{1}{2}\right) = \frac{1}{2}\rho_{ij}V_{ij} + \frac{1}{2}\rho_{ij+1}V_{ij+1} \tag{5.59b}$$

where the subscript P refers to the main diagonal elements. Remark that from (5.59), in the cut-cells at least, the mass matrix for $u_{i+\frac{1}{2}j}$ and $v_{ij+\frac{1}{2}}$ is not constructed from the actual areas of $\Omega^u_{i+\frac{1}{2}j}$ and $\Omega^v_{ij+\frac{1}{2}}$.

Next, we establish the constrains on $\mathcal{C}\left[\overline{\mathcal{U}}\right]$, $\mathcal{G}$ and $\mathcal{K}$ based on the conservation of the kinetic energy $E_c(t) = \int_{\Omega_f} \frac{\rho|\mathbf{U}|^2}{2} dV$. The latter is discretized by the trapezoidal rule in each fluid cell Ω_{ij}.

$$\begin{aligned} E_c(t) &\equiv \frac{1}{2} \sum_{\text{Control volumes}} \int_{\Omega_{ij}} \rho|\mathbf{U}|^2 dV \\ &\cong \frac{1}{2} \sum_{\text{Control volumes}} \left[\frac{1}{2} \left(\rho_{ij} u^2_{i+\frac{1}{2}j} V_{ij} + \rho_{i-1j} u^2_{i-\frac{1}{2}j} V_{i-1j} \right) \right. \\ &\qquad \left. + \frac{1}{2} \left(\rho_{ij+1} v^2_{ij+\frac{1}{2}} V_{ij+1} + \rho_{ij-1} v^2_{ij-\frac{1}{2}} V_{ij-1} \right) \right] \end{aligned} \tag{5.60}$$

In matrix form, (5.60) reads

$$E_c(t) \cong E_c^h(t) = \frac{1}{2} \mathcal{U}^T \mathcal{M} \mathcal{U} \tag{5.61}$$

To obtain the conservation equation for $E_c^h(t)$, one first multiply on the left-hand-side of (5.58) by $\mathcal{U}^T$ to have

$$\mathcal{U}^T \frac{d}{dt} (\mathcal{M}\mathcal{U}) = -\mathcal{U}^T \mathcal{C}\left[\overline{\mathcal{U}}\right] \mathcal{U} - \mathcal{U}^T \mathcal{G}\mathcal{P} + \mathcal{U}^T \mathcal{F}_\Gamma - \mathcal{U}^T \mathcal{K}\mathcal{U} \tag{5.62}$$

Remark that the transpose of a product of two matrices equals the product of their transposes in reverse order. The transpose of (5.58) thus becomes

$$\frac{d}{dt} \left(\mathcal{U}^T \mathcal{M}^T \right) = -\mathcal{U}^T \mathcal{C}\left[\overline{\mathcal{U}}\right]^T - \mathcal{P}^T \mathcal{G}^T + \mathcal{F}_\Gamma^T - \mathcal{U}^T \mathcal{K}^T \tag{5.63}$$

Multiplying $\mathcal{U}$ on the right-hand-side of (5.63), we get

$$\frac{d}{dt} \left(\mathcal{U}^T \mathcal{M}^T \right) \mathcal{U} = -\mathcal{U}^T \mathcal{C}\left[\overline{\mathcal{U}}\right]^T \mathcal{U} - \mathcal{P}^T \mathcal{G}^T \mathcal{U} + \mathcal{F}_\Gamma^T \mathcal{U} - \mathcal{U}^T \mathcal{K}^T \mathcal{U} \tag{5.64}$$

The above-mentioned property of transposed matrices applies once again to give us

$$\mathcal{U}^T \mathcal{G}\mathcal{P} = \mathcal{U}^T \left[(\mathcal{G}\mathcal{P})^T \right]^T = \mathcal{U}^T \left[\mathcal{P}^T \mathcal{G}^T \right]^T = \mathcal{P}^T \mathcal{G}^T \mathcal{U} \tag{5.65}$$

Adding (5.62) to (5.64) and using (5.65), we obtain at last

$$\begin{aligned} \frac{dE_c^h}{dt} = &- \mathcal{U}^T \frac{\mathcal{C}\left[\overline{\mathcal{U}}\right]^T + \mathcal{C}\left[\overline{\mathcal{U}}\right]}{2} \mathcal{U} - \mathcal{P}^T \mathcal{G}^T \mathcal{U} \\ &+ \frac{\mathcal{F}_\Gamma^T \mathcal{U} + \mathcal{U}^T \mathcal{F}_\Gamma}{2} - \mathcal{U}^T \frac{\mathcal{K}^T + \mathcal{K}}{2} \mathcal{U} \end{aligned} \tag{5.66}$$

(5.66) must be similar to (5.50) to conserve the kinetic energy. To this end, two requirements should be satisfied. First, the viscous term $-\mathcal{U}^T\left(\mathcal{K}^T+\mathcal{K}\right)\mathcal{U}$ should mimic the viscous dissipation of the kinetic energy budget. Thus, it must be negative and the matrix $\mathcal{K}^T+\mathcal{K}$ positive definite. In the finite-volume method framework, this can be obtained if the discrete diffusive flux is stable and consistent (Eymard et al. 2000 [34]). Note that the symmetry of $\mathcal{K}$ is not necessary. The second condition imposes the discretized convective terms to be a skew-symmetric matrix.

$$\mathcal{C}\left[\mathcal{U}\right]=-\mathcal{C}\left[\mathcal{U}\right]^T \quad \Rightarrow \quad -\mathcal{U}^T\frac{\mathcal{C}\left[\mathcal{U}\right]^T+\mathcal{C}\left[\mathcal{U}\right]}{2}\mathcal{U}=0 \tag{5.67}$$

and the pressure gradient to be dual to the divergence operator (5.55).

$$\mathcal{G}=-\mathcal{D}^T \quad \Rightarrow \quad -\mathcal{P}^T\mathcal{G}^T\mathcal{U}=\mathcal{P}^T\mathcal{D}\mathcal{U}=0 \tag{5.68}$$

Under these constrains and when the viscosity and the surface tension disappear, the kinetic energy budget (5.66) becomes

$$\begin{aligned}\frac{dE_c^h}{dt}=&\frac{\mathcal{F}_\Gamma^T\mathcal{U}+\mathcal{U}^T\mathcal{F}_\Gamma}{2}-\mathcal{U}^T\frac{\mathcal{K}^T+\mathcal{K}}{2}\mathcal{U}\\ &\xrightarrow{\mu\to 0} \quad \frac{\mathcal{F}_\Gamma^T\mathcal{U}+\mathcal{U}^T\mathcal{F}_\Gamma}{2} \quad \xrightarrow{\sigma\to 0} \quad 0\end{aligned} \tag{5.69}$$

It will be seen that the constrains established here enable the discretization of the pressure gradient and the convective fluxes in the next paragraphs.

Discretization of the pressure gradient

Thanks to (5.54) and (5.55), one can write the divergence operator in x-contribution as in Fig 5.9. (5.68) indicates that the x- and y-components of the discrete pressure gradient in $\Omega^u_{i+\frac{1}{2}j}$ and in $\Omega^v_{ij+\frac{1}{2}}$ should be

$$\int_{\Gamma^u_{i+\frac{1}{2}j}} p\mathbf{e}_x\cdot\mathbf{n}dS \cong \left[\mathcal{G}^x\mathcal{P}\right]_{i+\frac{1}{2}j}=\theta^u_{i+\frac{1}{2}j}\Delta y\left(p_{i+1j}-p_{ij}\right) \tag{5.70a}$$

$$\int_{\Gamma^v_{ij+\frac{1}{2}}} p\mathbf{e}_y\cdot\mathbf{n}dS \cong \left[\mathcal{G}^y\mathcal{P}\right]_{ij+\frac{1}{2}}=\theta^v_{ij+\frac{1}{2}}\Delta x\left(p_{ij+1}-p_{ij}\right) \tag{5.70b}$$

Two cases should be distinguished while examining (5.70a).

In a Cartesian fluid cell far from the immersed boundary ($\theta^{u}_{i+\frac{1}{2}j} = 1$), one could find again the finite-difference gradient of the MAC method.

$$[\mathcal{G}^{x}\mathcal{P}]_{i+\frac{1}{2}j} = \frac{p_{i+1j} - p_{ij}}{\Delta x} [\mathcal{M}^{x}]_{P} \left(i + \frac{1}{2}j\right)$$

where $[\mathcal{M}^{x}]_{P} \left(i + \frac{1}{2}j\right) = \Delta x \times \Delta y$ for the Cartesian control volume $\Omega^{u}_{i+\frac{1}{2}j}$.

Meanwhile, in a cut-cell, it is not possible to interpret (5.70) as finite-difference quotients for p_{ij} located at the centroids of the cut-cells. Instead, p_{ij} is an approximation of the pressure everywhere inside the control volume Ω_{ij}, even on its solid face. This is equivalent to the zero pressure gradient boundary condition on solid frontier. We shall see later that the normal viscous stresses are discretized in the same manner (§ 5.7.3.4).

As with discrete velocity components, the discrete values p_{ij} are stored in a vector $\mathcal{P}$. Like $\mathbb{U}$ for the $x-$ velocity components, $\mathcal{P}$ is built by sweeping the MAC grid in 5.8 horizontally followed by vertically. In consequence, one gets the discrete pressure gradient expressed by the matrix $\mathcal{GP}$. Similar to $\mathcal{DU}$, it can be rewritten as the sum of $\mathcal{G}^{x}\mathcal{P}$ and $\mathcal{G}^{y}\mathcal{P}$ with $\mathcal{G}^{x}$ and $\mathcal{G}^{y}$ in comparable structure to that of $\mathcal{D}^{x}$ and $\mathcal{D}^{y}$.

Skew-symmetric discretization of the convective fluxes

We have stated lately that the discretized convective term should be a skew-symmetric matrix so as to satisfy (5.72). For this to be done, we first discretize the momentum equation, then impose a skew-symmetric properties to the discretization of the convective term.

The first step is carried out by the five-point scheme, chosen because of its simplicity. We present hereafter the discretization of (5.48a) in the x-direction but that in y-direction should be analogous. Cartesian fluid cells are also distinguished from cut-cells.

For a fluid control volume far from the immersed boundary, the five-point scheme gives

$$\begin{aligned}\int_{\Gamma^u_{i+\frac{1}{2}j}} (\mathbf{U}\cdot\mathbf{n})\,\rho u dS \cong\ & c\,[\overline{u}]_W\left(i+\frac{1}{2}j\right)u_{i-\frac{1}{2}j} + c\,[\overline{u}]_E\left(i+\frac{1}{2}j\right)u_{i+\frac{3}{2}j} \\ & + c\,[\overline{u}]_S\left(i+\frac{1}{2}j\right)u_{i+\frac{1}{2}j-1} + c\,[\overline{u}]_N\left(i+\frac{1}{2}j\right)u_{i+\frac{1}{2}j+1} \\ & + c\,[\overline{u}]_P\left(i+\frac{1}{2}j\right)u_{i+\frac{1}{2}j}\end{aligned} \tag{5.71}$$

which in combination with (5.67) yields

$$c\,[\overline{u}]_P\left(i+\frac{1}{2}j\right) = 0 \tag{5.72a}$$

$$c\,[\overline{u}]_E\left(i+\frac{1}{2}j\right) = -c\,[\overline{u}]_W\left(i+\frac{3}{2}j\right) \tag{5.72b}$$

$$c\,[\overline{u}]_N\left(i+\frac{1}{2}j\right) = -c\,[\overline{u}]_S\left(i+\frac{1}{2}j+1\right) \tag{5.72c}$$

which is the skew-symmetric condition for this type of cells.

On uniform meshes, (5.72) is verified by the central discretization of the MAC method. Other popular discretization, such as discretizations of upwind type, are known to violate (5.72). On non-uniform meshes, a skew-symmetric discretization is proposed by Verstappen & Veldman 2003 [100] to enforce (5.72).

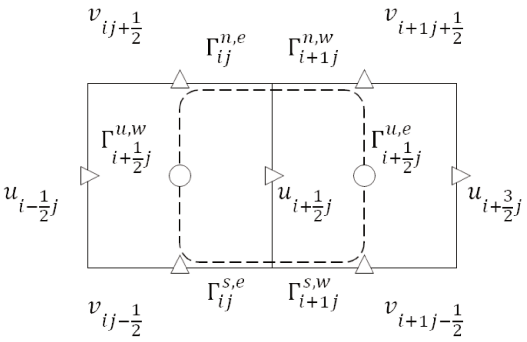

Figure 5.11: Control volume $\Gamma^u_{i+\frac{1}{2}j}$

To explain the method of Verstappen & Veldman 2003 [100], consider a Cartesian control volume $\Omega^u_{i+\frac{1}{2}j}$ exhibited in Fig. 5.11. The skew-symmetric discretization

consists in decomposing the convective term into net fluxes through four elementary faces of the cell.

$$\begin{aligned}\int_{\Gamma^{u}_{i+\frac{1}{2}j}} (\mathbf{U}\cdot\mathbf{n})\,\rho u dS = &-\int_{\Gamma^{u,w}_{i+\frac{1}{2}j}} (\mathbf{U}\cdot\mathbf{e}_x)\,\rho u dy + \int_{\Gamma^{u,e}_{i+\frac{1}{2}j}} (\mathbf{U}\cdot\mathbf{e}_x)\,\rho u dy \\ &-\int_{\Gamma^{s,e}_{ij}\cup\Gamma^{s,w}_{i+1j}} (\mathbf{U}\cdot\mathbf{e}_y)\,\rho u dx + \int_{\Gamma^{n,e}_{ij}\cup\Gamma^{n,w}_{i+1j}} (\mathbf{U}\cdot\mathbf{e}_y)\,\rho u dx\end{aligned} \tag{5.73}$$

Each term in (5.73) is discretized with help of the discrete fluxes (5.53). Through the east face, for example, it reads

$$\int_{\Gamma^{u,e}_{i+\frac{1}{2}j}} (\mathbf{U}\cdot\mathbf{e}_x)\,\rho u dy \cong \frac{\rho_{i+\frac{1}{2}j}\overline{u}_{i+\frac{1}{2}j} + \rho_{i+\frac{3}{2}j}\overline{u}_{i+\frac{3}{2}j}}{2} u_e \tag{5.74}$$

where u_e is a characteristic value of u on $\Gamma^{u,e}_{i+\frac{1}{2}j}$, derived from the interpolation of the discrete velocity unknowns. Verstappen & Veldman [100] cite that the only possible way to verify the skew-symmetric conditions of (5.72) is the central interpolation with equal weighting as

$$u_e = \frac{u_{i+\frac{1}{2}j} + u_{i+\frac{3}{2}j}}{2} \tag{5.75}$$

Proceeding in the same way for the other faces, one should get for instance on the south face

$$\int_{\Gamma^{s,e}_{ij}\cup\Gamma^{s,w}_{i+1j}} (\mathbf{U}\cdot\mathbf{e}_y)\,\rho u dx \cong \frac{\rho_{ij-\frac{1}{2}}\overline{v}_{ij-\frac{1}{2}} + \rho_{i+1j-\frac{1}{2}}\overline{v}_{i+1j-\frac{1}{2}}}{2} u_s \tag{5.76}$$

with $u_s = \frac{u_{i+\frac{1}{2}j-1} + u_{i+\frac{1}{2}j}}{2}$. The local conservation of the fluxes through fluid faces leads to

$$\int_{\Gamma^{u,w}_{i+\frac{1}{2}j}} (\mathbf{U}\cdot\mathbf{e}_x)\,\rho u dy = \int_{\Gamma^{u,e}_{i-\frac{1}{2}j}} (\mathbf{U}\cdot\mathbf{e}_x)\,\rho u dy \tag{5.77a}$$

$$\int_{\Gamma^{n,e}_{ij}} (\mathbf{U}\cdot\mathbf{e}_y)\,\rho u dx = \int_{\Gamma^{s,e}_{ij+1}} (\mathbf{U}\cdot\mathbf{e}_y)\,\rho u dx \tag{5.77b}$$

By comparing (5.77) to (5.71), we have

$$\mathcal{C}\left[\overline{u}\right]_P\left(i+\frac{1}{2}j\right)=\frac{1}{4}\rho_{ij}\dot{q}_{ij}+\frac{1}{4}\rho_{i+j}\dot{q}_{i+1j} \tag{5.78a}$$

$$\mathcal{C}\left[\overline{u}\right]_E\left(i+\frac{1}{2}j\right)=\frac{1}{4}\rho_{i+\frac{1}{2}j}\overline{u}_{i+\frac{1}{2}j}+\frac{1}{4}\rho_{i+\frac{3}{2}j}\overline{u}_{i+\frac{3}{2}j} \tag{5.78b}$$

$$\mathcal{C}\left[\overline{u}\right]_W\left(i+\frac{1}{2}j\right)=-\frac{1}{4}\rho_{i-\frac{1}{2}j}\overline{u}_{i-\frac{1}{2}j}-\frac{1}{4}\rho_{i+\frac{1}{2}j}\overline{u}_{i+\frac{1}{2}j} \tag{5.78c}$$

$$\mathcal{C}\left[\overline{u}\right]_N\left(i+\frac{1}{2}j\right)=\frac{1}{4}\rho_{ij+\frac{1}{2}}\overline{v}_{ij+\frac{1}{2}}+\frac{1}{4}\rho_{i+\frac{3}{2}j}\overline{v}_{i+\frac{3}{2}j} \tag{5.78d}$$

$$\mathcal{C}\left[\overline{u}\right]_S\left(i+\frac{1}{2}j\right)=-\frac{1}{4}\rho_{ij-\frac{1}{2}}\overline{v}_{ij-\frac{1}{2}}-\frac{1}{4}\rho_{i+1j-\frac{1}{2}}\overline{v}_{i+1j-\frac{1}{2}} \tag{5.78e}$$

The above discretization coefficients satisfy the skew-symmetry conditions (5.72) because the discrete continuity equation is verified in Ω_{ij} and Ω_{i+1j}, i.e. $\dot{q}_{ij}=0$ and $\dot{q}_{i+1j}=0$, respectively (refer to (5.52) or (5.54)).

The skew-symmetry discretization (5.71) and (5.78) are for the Cartesian control volume $\Omega^u_{i+\frac{1}{2}j}$ in Fig. 5.11. With regard to a cut-cell, attention needs to be paid to the boundary conditions on the solid frontier. Unlike the pressure gradient where a unique formula is valid for all cut-cells (5.70), the discretization here should be constructed in each of the half generic control volumes such as (5.67) be verified for any combinations of these half control volumes.

Let's consider, for example, the control volume $\Omega^u_{i+\frac{1}{2}j}$ in Fig. 5.7, whose north solid boundary $\Gamma^{ib,e}_{ij}\cup\Gamma^{ib,w}_{i+1j}$ is built from two halves of trapezoidal cut-cells. The discretization of the convective term in $\Omega^u_{i+\frac{1}{2}j}$ is

$$\begin{aligned}\int_{\Gamma^u_{i+\frac{1}{2}j}}(\mathbf{U}\cdot\mathbf{n})\,\rho u dS \cong\ & \mathcal{C}\left[\overline{u}\right]_W\left(i+\frac{1}{2}j\right)u_{i-\frac{1}{2}j}+\mathcal{C}\left[\overline{u}\right]_E\left(i+\frac{1}{2}j\right)u_{i+\frac{3}{2}j}\\ &+\mathcal{C}\left[\overline{u}\right]_S\left(i+\frac{1}{2}j\right)u_{i+\frac{1}{2}j-1}\\ &+\mathcal{C}\left[\overline{u}\right]_P\left(i+\frac{1}{2}j\right)u_{i+\frac{1}{2}j}\end{aligned} \tag{5.79}$$

where $\mathcal{C}\left[\overline{u}\right]_N\left(i+\frac{1}{2}j\right)$ is discarded since the velocity unknown $u_{i+\frac{1}{2}j+1}$ does not exist. In this case, (5.67) becomes

$$\mathcal{C}\left[\overline{u}\right]_P\left(i+\frac{1}{2}j\right)=0,\quad \mathcal{C}\left[\overline{u}\right]_E\left(i+\frac{1}{2}j\right)=-\mathcal{C}\left[\overline{u}\right]_W\left(i+\frac{3}{2}j\right) \tag{5.80}$$

To obtain the discretization satisfying (5.80), we decompose the boundary of the control volume as

$$\Gamma^{u}_{i+\frac{1}{2}j} = \Gamma^{u,w}_{i+\frac{1}{2}j} \cup \Gamma^{u,e}_{i+\frac{1}{2}j} \cup \left(\Gamma^{s,e}_{ij} \cup \Gamma^{s,w}_{i+1j}\right) \cup \left(\Gamma^{ib,e}_{ij} \cup \Gamma^{ib,w}_{i+1j}\right) \tag{5.81}$$

and write the convective term as the net flux through each of these faces.

$$\begin{aligned}\int_{\Gamma^{u}_{i+\frac{1}{2}j}} (\mathbf{U}\cdot\mathbf{n})\,\rho u dS = &-\int_{\Gamma^{u,w}_{i+\frac{1}{2}j}} (\mathbf{U}\cdot\mathbf{e}_x)\,\rho u dy + \int_{\Gamma^{u,e}_{i+\frac{1}{2}j}} (\mathbf{U}\cdot\mathbf{e}_x)\,\rho u dy \\ &- \int_{\Gamma^{s,e}_{ij}\cup\Gamma^{s,w}_{i+1j}} (\mathbf{U}\cdot\mathbf{e}_y)\,\rho u dx + \int_{\Gamma^{ib,e}_{ij}\cup\Gamma^{ib,w}_{i+1j}} \left(\mathbf{U}\cdot\mathbf{n}^{ib}\right)\rho u dS\end{aligned} \tag{5.82}$$

The fluxes through each of the fluid faces are given by (5.74), (5.76) and (5.77), whereas those through each half of solid face $\Gamma^{ib,e}_{ij}$ and $\Gamma^{ib,w}_{i+1j}$ are nil. We thus have

$$\int_{\Gamma^{ib,e}_{ij}} \left(\mathbf{U}\cdot\mathbf{n}^{ib}_{ij}\right)\rho u dS = 0, \quad \int_{\Gamma^{ib,w}_{i+1j}} \left(\mathbf{U}\cdot\mathbf{n}^{ib}_{i+1j}\right)\rho u dS = 0 \tag{5.83}$$

The discretization of the convective term in this control volume is also given by (5.78), with the exception that

$$\mathcal{C}\left[\overline{u}\right]_N \left(i+\frac{1}{2}j\right) = 0 \tag{5.84}$$

The skew-symmetry conditions (5.80) for cut-cells are therefore verified. Similar processes are applied for the other types of half control volumes.

5.7.3.4 *Discretization of the momentum equation based on the conservation of total momentum – Viscous fluxes*

The third term of the momentum equation (5.48) to be discretized is the viscous fluxes. Unlike the discretization of the pressure gradient and the convection term which is based on the kinetic energy conservation, that of the viscous fluxes is carried out thanks to the conservation of the total momentum.

Let's consider, for example, the x-momentum equation (5.48a) in which the viscous terms for a control volume $\Omega^u_{i+\frac{1}{2}j}$ are made up of normal stress fluxes and shear stress fluxes as follows

$$\begin{aligned}\int_{\Gamma^u_{i+\frac{1}{2}j}} 2\mu \mathbf{D}\ \mathbf{e}_x \cdot \mathbf{n} dS = &\int_{\Gamma^u_{i+\frac{1}{2}j}} 2\mu \frac{\partial u}{\partial x}\ \mathbf{e}_x \cdot \mathbf{n} dS \\ &+ \int_{\Gamma^u_{i+\frac{1}{2}j}} \mu \left(\frac{\partial v}{\partial x} + \frac{\partial u}{\partial y}\right)\ \mathbf{e}_y \cdot \mathbf{n} dS\end{aligned} \tag{5.85}$$

Our aim is to discretize these terms in the cut-cells by the nine-point scheme. The discretization is built by enforcing the conservation of the total momentum (5.49b) at the discrete level. This is equivalent to stating that in the cut-cells the discretization of the viscous fluxes should be consistent with that of the hydrodynamic forces (5.51).

It will be shown that these two types of stress fluxes, i.e. the normal stress fluxes $\int_{\Gamma^u_{i+\frac{1}{2}j}} 2\mu \frac{\partial u}{\partial x}\ \mathbf{e}_x \cdot \mathbf{n} dS$ and the shear stress fluxes $\int_{\Gamma^u_{i+\frac{1}{2}j}} \mu \left(\frac{\partial v}{\partial x} + \frac{\partial u}{\partial y}\right)\ \mathbf{e}_y \cdot \mathbf{n} dS$ are discretized differently. The viscosity is calculated by (5.39). There is also a distinction between Cartesian fluid cells and cut-cells as previously implementing.

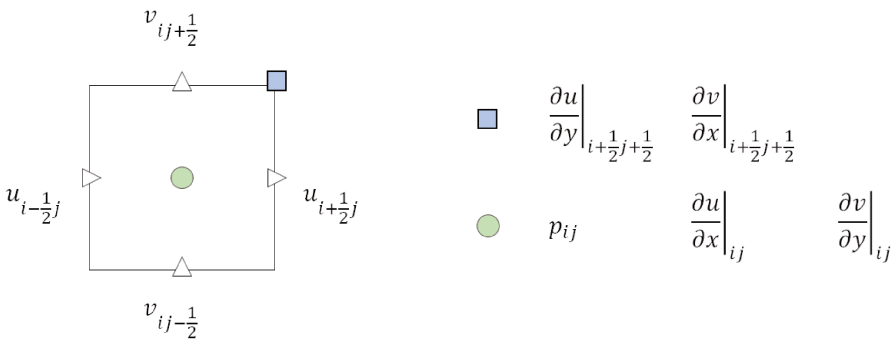

Figure 5.12: Location of pressure and viscous stresses in a Cartesian grid-cell Ω_{ij}

In Cartesian fluid cells, due to the staggering of the velocity unknowns, one can locate on the MAC mesh, the normal stresses (5.86) at the center of the cell Ω_{ij} (see Fig. 5.12).

$$\left.\frac{\partial u}{\partial x}\right|_{ij} = \frac{u_{i+\frac{1}{2}j} - u_{i-\frac{1}{2}j}}{\Delta x}, \qquad \left.\frac{\partial v}{\partial y}\right|_{ij} = \frac{v_{ij+\frac{1}{2}} - v_{ij-\frac{1}{2}}}{\Delta y} \tag{5.86}$$

Meanwhile, the shear stresses are located at the upper right corner of the cell.

$$\left.\frac{\partial u}{\partial y}\right|_{i+\frac{1}{2}j+\frac{1}{2}} = \frac{u_{i+\frac{1}{2}j+1} - u_{i+\frac{1}{2}j}}{\Delta y}, \qquad \left.\frac{\partial v}{\partial x}\right|_{i+\frac{1}{2}j+\frac{1}{2}} = \frac{v_{i+1j+\frac{1}{2}} - v_{ij+\frac{1}{2}}}{\Delta x} \tag{5.87}$$

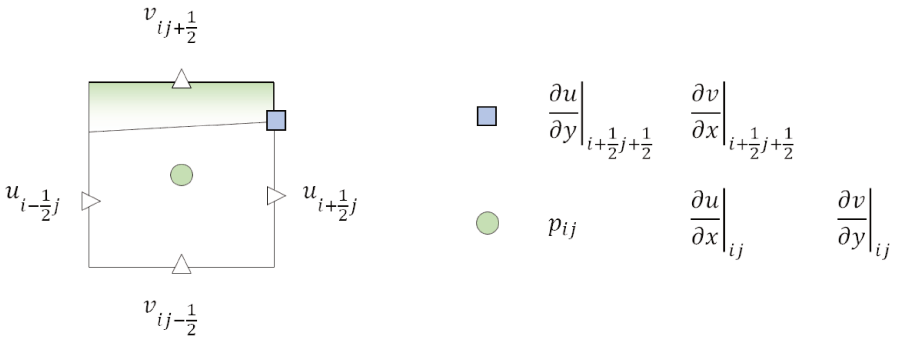

Figure 5.13: Location of pressure and viscous stresses in a cut-cell Ω_{ij}

In the cut-cells, in the presence of the solid frontier, the shear stresses are located at the vertices of the cell (Fig. 5.13). Meanwhile, the normal stresses, having a physical origin (diagonal part of the Cauchy stress tensor) and a mathematical regularity similar to that of the pressure, should be consistent with the latter. Therefore, they are assumed to be homogeneous everywhere inside the cut-cell, and it is unnecessary to precisely describe their position in the cell. For simplicity, we put $\left.\frac{\partial u}{\partial x}\right|_{ij}$ and $\left.\frac{\partial v}{\partial y}\right|_{ij}$ at the same location as p_{ij} in the cut-cell Ω_{ij} in Fig. 5.13.

In the following paragraphs, the discretization of the two stress terms are subsequently presented. A nine-point scheme is adopted to dicretize them, with the imposed consistency with the pressure for the discretization of the normal stresses and the total momentum conservation at discrete level for that of the shear stresses. In other words, the discretization of the viscous fluxes in the cut-cells in particular is supposed to be consistent with that of hydrodynamic forces (5.51).

Discretization of the normal stress fluxes

Presented below is the discretization technique for the normal stresses in a cut-cell, which is a general case. The method obviously works well for any Cartesian fluid cells.

To discretize the normal stress flux $\int_{\Gamma^u_{i+\frac{1}{2}j}} 2\mu\frac{\partial u}{\partial x}\ \mathbf{e}_x \cdot \mathbf{n} dS$ in a cut-cell, for example, one might expect to transform the term into the net flux through the east $\Gamma^{u,e}_{i+\frac{1}{2}j}$ and west $\Gamma^{u,w}_{i+\frac{1}{2}j}$ faces, then discretize them with a differential quotient.

From Fig. 5.13, we have

$$\int_{\Gamma^{u,w}_{i+\frac{1}{2}j}} 2\mu \frac{\partial u}{\partial x}\ \mathbf{e}_x \cdot \mathbf{n} dS \cong 2\mu\ \Delta y^{u,w}_{i+\frac{1}{2}j} \frac{u_{i+\frac{1}{2}j} - u_{i-\frac{1}{2}j}}{\Delta x} \tag{5.88}$$

where the area $\Delta y^{u,w}_{i+\frac{1}{2}j}$ is yet to be defined. According to Cheny & Botella 2010 [10] and Eymard et al. 2000 [34], since the line joining the location of $u_{i-\frac{1}{2}j}$ and $u_{i+\frac{1}{2}j}$ is not orthogonal to the west face $\Gamma^{u,w}_{i+\frac{1}{2}j}$ in the trapezoidal cut-cell of Fig. 5.13, our mesh is not admissible for the normal stresses in the cut-cells and therefore make (5.88) inconsistent and yields large numerical errors.

Based on the requirement that the discrete normal stresses should be consistent with the discrete pressure, one can improve the consistency of the discretization of $\int_{\Gamma^u_{i+\frac{1}{2}j}} 2\mu \frac{\partial u}{\partial x}\ \mathbf{e}_x \cdot \mathbf{n} dS$ by discretizing the normal stress fluxes in a similar way to the pressure gradient as in (5.70a). We then have

$$\int_{\Gamma^u_{i+\frac{1}{2}j}} 2\mu \frac{\partial u}{\partial x}\ \mathbf{e}_x \cdot \mathbf{n} dS \cong \theta^u_{i+\frac{1}{2}j} \Delta y \left(2\mu\,(\phi)_{i+1j} \left.\frac{\partial u}{\partial x}\right|_{i+1j} - 2\mu\,(\phi)_{ij} \left.\frac{\partial u}{\partial x}\right|_{ij} \right) \tag{5.89}$$

All terms in (5.89) are directly available except a differential quotient for $\left.\frac{\partial u}{\partial x}\right|_{ij}$ which need to be calculated. To this end, the Green's theorem has to be valid at the discrete level in a cut-cell.

$$\int_{\Omega_{ij}} \left(\frac{\partial u}{\partial x} + \frac{\partial v}{\partial y} \right) dV = \int_{\Gamma_{ij}} \mathbf{U} \cdot \mathbf{n} dS \tag{5.90}$$

Next, we discretize the left-hand side of (5.90) to get

$$\int_{\Omega_{ij}} \left(\frac{\partial u}{\partial x} + \frac{\partial v}{\partial y} \right) dV = \left(\left.\frac{\partial u}{\partial x}\right|_{ij} + \left.\frac{\partial v}{\partial y}\right|_{ij} \right) V_{ij} \tag{5.91}$$

Finally, by combining (5.91) with the continuity equations (5.47), (5.52) and (5.54), we obtain

$$\left.\frac{\partial u}{\partial x}\right|_{ij} \cong \frac{\theta^u_{i+\frac{1}{2}j} u_{i+\frac{1}{2}j} - \theta^u_{i-\frac{1}{2}j} u_{i-\frac{1}{2}j}}{V_{ij}/\Delta y} \tag{5.92a}$$

An analogous expression holds for $\left.\frac{\partial v}{\partial y}\right|_{ij}$.

$$\left.\frac{\partial v}{\partial y}\right|_{ij} \cong \frac{\theta^{v}_{ij+\frac{1}{2}} v_{ij+\frac{1}{2}} - \theta^{v}_{ij-\frac{1}{2}} v_{ij-\frac{1}{2}}}{V_{ij}/\Delta x} \tag{5.92b}$$

(5.92) formulae are valid for any cut-cells, with the boundary conditions naturally embedded. They also become the standard finite-difference quotients for all Cartesian fluid cells (Okajima 1982 [68]).

A first discretization of the shear stress fluxes

As stated by Cheny & Botella 2010 [10], unlike the normal stress flux, our mesh is admissible for the shear stress flux $\int_{\Gamma^{u}_{i+\frac{1}{2}j}} \mu \left(\frac{\partial v}{\partial x} + \frac{\partial u}{\partial y}\right) \mathbf{e}_y \cdot \mathbf{n} dS$ (see Fig. 5.7), allowing to write its discretization as the net flux through the north and south faces. Again, we separate fluid cells from cut-cells in our consideration.

For a Cartesian fluid cell far from the immersed boundary, we have

$$\begin{aligned}\int_{\Gamma^{u}_{i+\frac{1}{2}j}} \mu \left(\frac{\partial v}{\partial x} + \frac{\partial u}{\partial y}\right) \mathbf{e}_y \cdot \mathbf{n} dS = &\int_{\Gamma^{n,e}_{ij} \cup \Gamma^{n,w}_{i+1j}} \mu \left(\frac{\partial v}{\partial x} + \frac{\partial u}{\partial y}\right) dx \\ &- \int_{\Gamma^{s,e}_{ij} \cup \Gamma^{s,w}_{i+1j}} \mu \left(\frac{\partial v}{\partial x} + \frac{\partial u}{\partial y}\right) dx\end{aligned} \tag{5.93}$$

Applying the midpoint rule for the north face, for instance, one gets

$$\begin{aligned}&\int_{\Gamma^{n,e}_{ij} \cup \Gamma^{n,w}_{i+1j}} \mu \left(\frac{\partial v}{\partial x} + \frac{\partial u}{\partial y}\right) dx \cong \\ &\qquad \left(\Delta x^{n,e}_{ij} + \Delta x^{n,w}_{i+1j}\right) \mu(\phi)_{i+\frac{1}{2}j+\frac{1}{2}} \left(\left.\frac{\partial v}{\partial x}\right|_{i+\frac{1}{2}j+\frac{1}{2}} + \left.\frac{\partial u}{\partial y}\right|_{i+\frac{1}{2}j+\frac{1}{2}}\right)\end{aligned} \tag{5.94}$$

where the areas $\Delta x^{n,e}_{ij}$ and $\Delta x^{n,w}_{i+1j}$ represent only the fluid part of the faces to ensure the local conservation of the fluxes.

$$\Delta x^{n,e}_{ij} = \frac{1}{2}\theta^{v}_{ij+\frac{1}{2}} \Delta x, \qquad \Delta x^{n,w}_{i+1j} = \frac{1}{2}\theta^{v}_{i+1j+\frac{1}{2}} \Delta x \tag{5.95}$$

The quotients $\left.\frac{\partial v}{\partial x}\right|_{i+\frac{1}{2}j+\frac{1}{2}}$ and $\left.\frac{\partial u}{\partial y}\right|_{i+\frac{1}{2}j+\frac{1}{2}}$, located at the upper right corner of cell Ω_{ij} (see Fig. 5.12), are computed by differentiating the interpolation polynomial

of $v\left(\cdot, y_{j+\frac{1}{2}}\right)$ and $u\left(x_{i+\frac{1}{2}}, \cdot\right)$ in the horizontal and vertical directions, respectively. This results in

$$\begin{aligned}\left.\frac{\partial v}{\partial x}\right|_{i+\frac{1}{2}j+\frac{1}{2}} &= \frac{v_{i+1j+\frac{1}{2}} - v_{ij+\frac{1}{2}}}{\frac{1}{2}\theta^{v}_{i+1j+\frac{1}{2}}\Delta x + \frac{1}{2}\theta^{v}_{ij+\frac{1}{2}}\Delta x} \\ \left.\frac{\partial u}{\partial y}\right|_{i+\frac{1}{2}j+\frac{1}{2}} &= \frac{u_{i+\frac{1}{2}j+1} - u_{i+\frac{1}{2}j}}{\frac{1}{2}\theta^{u}_{i+\frac{1}{2}j+1}\Delta y + \frac{1}{2}\theta^{u}_{i+\frac{1}{2}j}\Delta y}\end{aligned} \tag{5.96}$$

which is similar to the usual one (5.87). The last three expressions (5.94), (5.95) and (5.96) are for the Cartesian cell of Fig. 5.12, but still valid when $u_{i+\frac{1}{2}j+1}$ is present in the fluid domain or when $\theta^{u}_{i+\frac{1}{2}j+1} > 0$.

The properties of a cut-cell like the one in Fig. 5.13, having its solid north face or $u_{i+\frac{1}{2}j+1}$ does not exist or $\theta^{u}_{i+\frac{1}{2}j+1} = 0$, requires us to take into account the boundary conditions. (5.94), (5.95) and (5.96) are thus adapted based on the ghost fluid method for elliptic equations (Gibou et al. 2002 [39]). On the north face of the above cut-cell, one should get

$$\begin{aligned}&\int_{\Gamma^{ib,e}_{ij}\cup\Gamma^{ib,w}_{i+1j}} \mu\left(\frac{\partial v}{\partial x} + \frac{\partial u}{\partial y}\right) dx \cong \\ &\qquad \left(\Delta x^{ib,e}_{ij} + \Delta x^{ib,w}_{i+1j}\right)\mu\left(\phi\right)_{i+\frac{1}{2}j+\frac{1}{2}}\left(\left.\frac{\partial v}{\partial x}\right|_{i+\frac{1}{2}j+\frac{1}{2}} + \left.\frac{\partial u}{\partial y}\right|_{i+\frac{1}{2}j+\frac{1}{2}}\right)\end{aligned} \tag{5.97}$$

with $\left.\frac{\partial v}{\partial x}\right|_{i+\frac{1}{2}j+\frac{1}{2}}$ as in (5.96) and $\left.\frac{\partial u}{\partial y}\right|_{i+\frac{1}{2}j+\frac{1}{2}}$ calculated by the one-sided differential quotient as

$$\left.\frac{\partial u}{\partial y}\right|_{i+\frac{1}{2}j+\frac{1}{2}} = \frac{-u_{i+\frac{1}{2}j}}{\frac{1}{2}\theta^{u}_{i+\frac{1}{2}j}\Delta y} \tag{5.98}$$

Note that in (5.97), the integration areas $\Delta x^{ib,e}_{ij}$ and $\Delta x^{ib,w}_{i+1j}$ on the solid face are yet to be defined.

The discretization of the viscous term has a nine-point structure. For the cut-cell in Fig. 5.14 whose north face is solid or $u_{i+\frac{1}{2}j+1}$ does not exist or $\theta^{u}_{i+\frac{1}{2}j+1} = 0$,

it is similar to (5.79). The discretization of the diffusion term for other types of cut-cells is given in Cheny & Botella 2010 [10].

$$\begin{aligned}\int_{\Gamma^u_{i+\frac{1}{2}j}} 2\mu \mathbf{D}\ \mathbf{e}_x \cdot \mathbf{n} dS \cong\ & \mathcal{K}_W\left(i+\frac{1}{2}j\right) u_{i-\frac{1}{2}j} + \mathcal{K}_E\left(i+\frac{1}{2}j\right) u_{i+\frac{3}{2}j} \\ & + \mathcal{K}_S\left(i+\frac{1}{2}j\right) u_{i+\frac{1}{2}j-1} \\ & + \mathcal{K}_P\left(i+\frac{1}{2}j\right) u_{i+\frac{1}{2}j} \\ & + \mathcal{K}_{SW}\left(i+\frac{1}{2}j\right) v_{ij-\frac{1}{2}} + \mathcal{K}_{SE}\left(i+\frac{1}{2}j\right) v_{i+1j-\frac{1}{2}} \\ & + \mathcal{K}_{NW}\left(i+\frac{1}{2}j\right) v_{ij+\frac{1}{2}} + \mathcal{K}_{NE}\left(i+\frac{1}{2}j\right) v_{i+1j+\frac{1}{2}}\end{aligned} \tag{5.99}$$

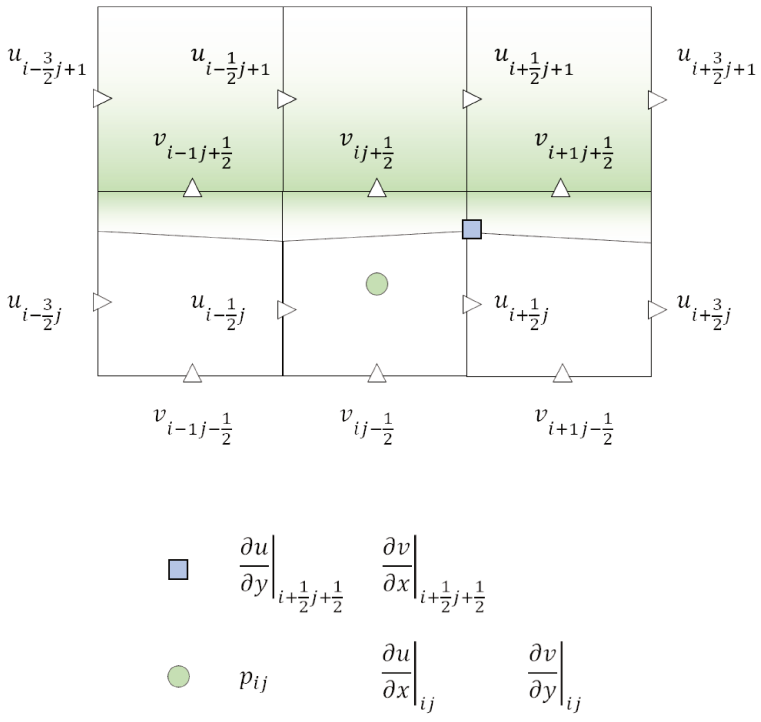

Figure 5.14: Viscous stresses in a cut-cell Ω_{ij}

with

$$\mathcal{K}_W\left(i+\frac{1}{2}j\right) = 2\mu(\phi)_{ij}\,\frac{\theta^u_{i+\frac{1}{2}j}\theta^u_{i-\frac{1}{2}j}\Delta y}{V_{ij}/\Delta y} \tag{5.100a}$$

$$\mathcal{K}_E\left(i+\frac{1}{2}j\right) = 2\mu(\phi)_{i+1j}\,\frac{\theta^u_{i+\frac{1}{2}j}\theta^u_{i+\frac{3}{2}j}\Delta y}{V_{i+1j}/\Delta y} \tag{5.100b}$$

$$\mathcal{K}_S\left(i+\frac{1}{2}j\right) = \mu(\phi)_{i+\frac{1}{2}j-\frac{1}{2}}\,\frac{2\Delta x}{\theta^u_{i+\frac{1}{2}j}\Delta y + \theta^u_{i+\frac{1}{2}j-1}\Delta y} \tag{5.100c}$$

$$\begin{aligned}\mathcal{K}_P\left(i+\frac{1}{2}j\right) = &-2\mu(\phi)_{ij}\,\frac{\left(\theta^u_{i+\frac{1}{2}j}\right)^2\Delta y}{V_{ij}/\Delta y} - 2\mu(\phi)_{i+1j}\,\frac{\left(\theta^u_{i+\frac{1}{2}j}\right)^2\Delta y}{V_{i+1j}/\Delta y}\\ &-\mathcal{K}_S\left(i+\frac{1}{2}j\right)\\ &-\mu(\phi)_{i+\frac{1}{2}j+\frac{1}{2}}\,\frac{\Delta x^{ib,e}_{ij}+\Delta x^{ib,w}_{i+1j}}{\frac{1}{2}\theta^u_{i+\frac{1}{2}j}\Delta y}\end{aligned} \tag{5.100d}$$

$$\mathcal{K}_{SW}\left(i+\frac{1}{2}j\right) = \mu(\phi)_{i+\frac{1}{2}j-\frac{1}{2}} \tag{5.100e}$$

$$\mathcal{K}_{SE}\left(i+\frac{1}{2}j\right) = -\mathcal{K}_{SW}\left(i+\frac{1}{2}j\right) \tag{5.100f}$$

$$\mathcal{K}_{NW}\left(i+\frac{1}{2}j\right) = 0 \tag{5.100g}$$

$$\mathcal{K}_{NE}\left(i+\frac{1}{2}j\right) = -\mathcal{K}_{NW}\left(i+\frac{1}{2}j\right) \tag{5.100h}$$

Remark that the discretization is symmetric, i.e. $\mathcal{K}_W\left(i+\frac{3}{2}j\right) = \mathcal{K}_E\left(i+\frac{1}{2}j\right)$, similar to the MAC method.

We finish the discretization of the shear stresses in cut-cells by the determination of the integration areas $\Delta x^{ib,e}_{ij}$ and $\Delta x^{ib,w}_{i+1j}$ in (5.97). Remember that their determination is based on the fact that the shear stress fluxes at the immersed boundary must correspond to the discretization of the shear part of the hydrodynamic forces (5.51). More specifically, this is equivalent to the discrete conservation of the total momentum. Detail to follow.

Discrete conservation of total momentum and computation of hydrodynamic forces

Like the kinetic energy (refer to § 5.7.3.3), the total momentum $\mathbf{P}(t) = \int_{\Omega_f} \rho \mathbf{U} dV$ is discretized under the trapezoidal rule as

$$\mathbf{P}(t) \widehat{=} \mathbf{P}^h(t) = \mathbb{1}^T \mathcal{M} \mathcal{U} \tag{5.101}$$

where $\mathbb{1}$ is the constant vector. Multiplying the semi-discrete scheme (5.58) with vector $\mathbb{1}$ to obtain the conservation equation for $\mathbf{P}^h(t)$ as

$$\frac{d\mathbf{P}^h}{dt} = -\mathbb{1}^T \mathcal{C}\left[\overline{\mathcal{U}}\right] \mathcal{U} - \left[\mathbb{1}^T \mathcal{G}\mathcal{P} - \mathbb{1}^T \mathcal{K}\mathcal{U}\right] - \mathbb{1}^T \mathcal{F}_\Gamma \tag{5.102}$$

which indeed is the semi-discrete version of (5.49b). Its quadratic terms in the right-hand side correspond to the summation of the convective, pressure, pressure jump and viscous fluxes across all control volumes. Since the flux local conservation holds at every fluid faces, all terms cancel out except those appearing at solid boundary faces of the cut-cells. As previously mentioned, these remaining terms should correspond to the forces acting on the immersed boundary. Therefore, the non-zero terms in the sum $\left[\mathbb{1}^T \mathcal{G}\mathcal{P} - \mathbb{1}^T \mathcal{K}\mathcal{U}\right]$ must be consistent with the discretization of the hydrodynamic force (5.51). Let's examine this condition in two steps.

First, the discretization of the hydrodynamic force is obtained by approximating the surface integrals in (5.51a) and (5.51b), respectively as

$$F_x^h = \sum_{\text{Cut-cells}\ \Omega_{ij}} [n_x \Delta S]_{ij}^{ib} \left(p_{ij} - 2\mu \left.\frac{\partial u}{\partial x}\right|_{ij} \right) - \text{Quad}_{ij}^{ib} \left(\mu \left(\frac{\partial v}{\partial x} + \frac{\partial u}{\partial y} \right) \mathbf{e}_y \cdot \mathbf{n} \right) \tag{5.103a}$$

$$F_y^h = \sum_{\text{Cut-cells}\ \Omega_{ij}} [n_y \Delta S]_{ij}^{ib} \left(p_{ij} - 2\mu \left.\frac{\partial v}{\partial y}\right|_{ij} \right) - \text{Quad}_{ij}^{ib} \left(\mu \left(\frac{\partial u}{\partial y} + \frac{\partial v}{\partial x} \right) \mathbf{e}_x \cdot \mathbf{n} \right) \tag{5.103b}$$

Here, the quadrature of the pressure and normal stress term is obtained by using the midpoint rule and based on the fact that these terms are constant in the cut-cells. As a result, the same formula is valid for all types of cut-cells. Meanwhile,

the quadrature of the shear stresses (denoted by Quad_{ij}^{ib}) has to be adapted to each type of cut-cells. This quadrature, based on the location of the shear stresses in Fig. 5.14 and the trapezoidal rule. For example, the portion of drag and lift acting on the solid part of the trapezoidal cut-cell of Fig. 5.14 is, respectively

$$\begin{aligned} F_x^h\Big|_{ij} = \sum_{\text{Cut-cells}\ \Omega_{ij}} & \left(\theta^u_{i-\frac{1}{2}j} - \theta^u_{i+\frac{1}{2}j}\right)\Delta y \left[p_{ij} - 2\mu(\phi)_{ij}\left.\frac{\partial u}{\partial x}\right|_{ij}\right] \\ & - \frac{\Delta x}{2}\left[\mu(\phi)_{i-\frac{1}{2}j+\frac{1}{2}}\left.\frac{\partial v}{\partial x}\right|_{i-\frac{1}{2}j+\frac{1}{2}} + \mu(\phi)_{i+\frac{1}{2}j+\frac{1}{2}}\left.\frac{\partial v}{\partial x}\right|_{i+\frac{1}{2}j+\frac{1}{2}}\right] \\ & - \frac{\Delta x}{2}\left[\mu(\phi)_{i-\frac{1}{2}j+\frac{1}{2}}\left.\frac{\partial u}{\partial y}\right|_{i-\frac{1}{2}j+\frac{1}{2}} + \mu(\phi)_{i+\frac{1}{2}j+\frac{1}{2}}\left.\frac{\partial u}{\partial y}\right|_{i+\frac{1}{2}j+\frac{1}{2}}\right] \end{aligned} \tag{5.104a}$$

$$\begin{aligned} F_y^h\Big|_{ij} = & \sum_{\text{Cut-cells}\ \Omega_{ij}} \Delta x\left[p_{ij} - 2\mu(\phi)_{ij}\left.\frac{\partial v}{\partial y}\right|_{ij}\right] \\ & - \frac{\left(\theta^u_{i-\frac{1}{2}j} - \theta^u_{i+\frac{1}{2}j}\right)\Delta y}{2}\left[\mu(\phi)_{i-\frac{1}{2}j+\frac{1}{2}}\left.\frac{\partial u}{\partial y}\right|_{i-\frac{1}{2}j+\frac{1}{2}} + \mu(\phi)_{i+\frac{1}{2}j+\frac{1}{2}}\left.\frac{\partial u}{\partial y}\right|_{i+\frac{1}{2}j+\frac{1}{2}}\right] \\ & - \frac{\left(\theta^u_{i-\frac{1}{2}j} - \theta^u_{i+\frac{1}{2}j}\right)\Delta y}{2}\left[\mu(\phi)_{i-\frac{1}{2}j+\frac{1}{2}}\left.\frac{\partial v}{\partial x}\right|_{i-\frac{1}{2}j+\frac{1}{2}} + \mu(\phi)_{i+\frac{1}{2}j+\frac{1}{2}}\left.\frac{\partial v}{\partial x}\right|_{i+\frac{1}{2}j+\frac{1}{2}}\right] \end{aligned} \tag{5.104b}$$

Second, return to the quadratic terms in the right-hand side of (5.102) that need to be discretized. These terms correspond to the summation of the convective, pressure and viscous fluxes from all control volumes. Their contribution in the x-direction is

$$\begin{aligned} \left[\mathbb{1}^T\mathcal{G}\mathcal{P} - \mathbb{1}^T\mathcal{K}\mathcal{U}\right]\Big|_x = \sum_{\text{Control volumes}\ \Omega^u_{i+\frac{1}{2}j}} & \int_{\Gamma^u_{i+\frac{1}{2}j}} \left[p - 2\mu\frac{\partial u}{\partial x}\right]\mathbf{e}_x\cdot\mathbf{n}\,dS \\ & - \int_{\Gamma^u_{i+\frac{1}{2}j}} \mu\left(\frac{\partial v}{\partial x} + \frac{\partial u}{\partial y}\right)\mathbf{e}_y\cdot\mathbf{n}\,dS \end{aligned} \tag{5.105}$$

which should certainly match the drag force F_x^h coming from (5.103a). We will inspect separately the normal stresses and the shear stresses.

Let's put it in more detail. Since a unique formula (5.70) and (5.92) is valid in all computational cells, the contribution of the normal stresses is

$$\sum_{\text{Control volumes}} \sum_{\Omega^u_{i+\frac{1}{2}j}} \theta^u_{i+\frac{1}{2}j} \Delta y \left[p_{i+1j} - p_{ij} - \left(2\mu(\phi)_{i+1j} \left.\frac{\partial u}{\partial x}\right|_{i+1j} - 2\mu(\phi)_{ij} \left.\frac{\partial u}{\partial x}\right|_{ij} \right) \right] \tag{5.106}$$

Re-indexing (5.106) to layout a sum across all cells, one has the pressure and normal stresses cancelled out in fluid cells such that $\theta^u_{i+\frac{1}{2}j} = \theta^u_{i-\frac{1}{2}j} = 1$, while keeping only the following terms in cut-cells

$$\sum_{\text{Cut-cells}} \sum_{\Omega_{ij}} \left(\theta^u_{i-\frac{1}{2}j} - \theta^u_{i+\frac{1}{2}j} \right) \Delta y \left(p_{ij} - 2\mu(\phi)_{ij} \left.\frac{\partial u}{\partial x}\right|_{ij} \right) \tag{5.107}$$

This is exactly the contribution of the normal stresses to the discrete drag force (5.103a). A similar inspection holds for the lift component (5.103b). Altogether, the total momentum budget is proved to be recovered.

With reference to the shear stresses, since only fluxes at the immersed boundary are maintained in (5.105) as those at all fluid faces counterbalance one another, one might write their exact expression depending on the type of cut-cell. For example, on the solid part $\Gamma^{ib,w}_{ij} \cup \Gamma^{ib,e}_{ij}$ of the cut-cell Ω_{ij} in Fig. 5.14, we use (5.97) for writing the shear stress contribution as

$$\begin{aligned} &- \left[\Delta x^{ib,w}_{ij} \mu(\phi)_{i-\frac{1}{2}j+\frac{1}{2}} \left.\frac{\partial u}{\partial y}\right|_{i-\frac{1}{2}j+\frac{1}{2}} + \Delta x^{ib,e}_{ij} \mu(\phi)_{i+\frac{1}{2}j+\frac{1}{2}} \left.\frac{\partial u}{\partial y}\right|_{i+\frac{1}{2}j+\frac{1}{2}} \right] \\ &- \left[\Delta x^{ib,w}_{ij} \mu(\phi)_{i-\frac{1}{2}j+\frac{1}{2}} \left.\frac{\partial v}{\partial x}\right|_{i-\frac{1}{2}j+\frac{1}{2}} + \Delta x^{ib,e}_{ij} \mu(\phi)_{i+\frac{1}{2}j+\frac{1}{2}} \left.\frac{\partial v}{\partial x}\right|_{i+\frac{1}{2}j+\frac{1}{2}} \right] \end{aligned} \tag{5.108}$$

A comparison with the drag force (5.104a) is enough to deduce the integration areas of the shear stress as

$$\Delta x^{ib,w}_{ij} = \Delta x^{ib,e}_{ij} = \frac{\Delta x}{2} \tag{5.109}$$

A similar inspection is possible for the other type of cut-cells for the shear stress flux $\int_{\Gamma^{ib,e}_{ij} \cup \Gamma^{ib,w}_{i+1j}} \frac{\partial u}{\partial y} dx$ and $\int_{\Gamma^{ib,n}_{ij} \cup \Gamma^{ib,s}_{ij+1}} \frac{\partial v}{\partial x} dy$.

5.7.3.5 *Pressure Poisson equation*

According to Cheny & Botella 2010 [10], the Poisson equation for pressure is:

$$\mathcal{A}\mathcal{P} = \mathcal{D}\mathcal{U}^* \tag{5.110}$$

where $\mathcal{U}^*$ is a vector containing the intermediate velocities and $\mathcal{A}$ a pentagonal and symmetric matrix with

$$\mathcal{A}_E(i,j) = \frac{\left(\theta^u_{i+\frac{1}{2}j}\Delta y\right)^2}{\frac{1}{2}\rho_{ij}V_{ij} + \frac{1}{2}\rho_{i+1j}V_{i+1j}}, \qquad \mathcal{A}_W(i,j) = \mathcal{A}_E(i-1,j) \tag{5.111a}$$

$$\mathcal{A}_N(i,j) = \frac{\left(\theta^v_{ij+\frac{1}{2}}\Delta x\right)^2}{\frac{1}{2}\rho_{ij}V_{ij} + \frac{1}{2}\rho_{ij+1}V_{ij+1}}, \qquad \mathcal{A}_S(i,j) = \mathcal{A}_N(i,j-1) \tag{5.111b}$$

$$\mathcal{A}_P(i,j) = -\mathcal{A}_E(i,j) - \mathcal{A}_W(i,j) - \mathcal{A}_N(i,j) - \mathcal{A}_S(i,j) \tag{5.111c}$$

Like the linear system (5.44) of the finite difference method in § 5.6, (5.111) can easily be solved by classical methods.

5.7.4 *Transport of the liquid-gas interface inside cut-cells*

The transport of the liquid-gas interface, as described in § 5.4.3, is not applicable for cut-cells and thus need to be modified.

To transport the level-set function ϕ, the divergence operator in (5.22) is similar to the one applied on the pressure. Hence, the transport in $x-$direction (5.22a) becomes

$$\widetilde{\phi}_{ij} = \frac{\phi^n_{ij} + \frac{\Delta t}{\Delta x}\left(G^\phi_{i-\frac{1}{2}j} - G^\phi_{i+\frac{1}{2}j}\right)}{1 - \frac{\Delta t}{\Delta x}\left(\theta^u_{i+\frac{1}{2}j}u_{i+\frac{1}{2}j} - \theta^u_{i-\frac{1}{2}j}u_{i-\frac{1}{2}j}\right)} \tag{5.112}$$

where $G^\phi_{i-\frac{1}{2}j}$, for example, is the flux from the left face of the grid-cell Ω_{ij} being calculated in the same manner as in § 5.4.3.

In $y-$direction, the transport equation (5.22b) evolves into

$$\widehat{\phi}_{ij} = \frac{\widetilde{\phi}_{ij} + \frac{\Delta t}{\Delta y}\left(\widetilde{G}^{\phi}_{i-\frac{1}{2}j} - \widetilde{G}^{\phi}_{i+\frac{1}{2}j}\right)}{1 - \frac{\Delta t}{\Delta y}\left(\theta^{v}_{ij+\frac{1}{2}} v_{ij+\frac{1}{2}} - \theta^{v}_{ij-\frac{1}{2}} v_{ij-\frac{1}{2}}\right)} \tag{5.113}$$

The level-set in the next time step is thus

$$\begin{aligned}\phi^{n+1}_{ij} = \widehat{\phi}_{ij} - \widetilde{\phi}_{ij}\frac{\Delta t}{\Delta x}\left(\theta^{u}_{i+\frac{1}{2}j} u_{i+\frac{1}{2}j} - \theta^{u}_{i-\frac{1}{2}j} u_{i-\frac{1}{2}j}\right) \\ - \widehat{\phi}_{ij}\frac{\Delta t}{\Delta y}\left(\theta^{v}_{ij+\frac{1}{2}} v_{ij+\frac{1}{2}} - \theta^{v}_{ij-\frac{1}{2}} v_{ij-\frac{1}{2}}\right)\end{aligned} \tag{5.114}$$

The advection of the volume-of-fluid function F inside the cut-cells is made possible with help of some modifications. The integrals of (5.29) are now approximated differently, containing the divergence operator similar to that of the pressure gradient, as follow

$$\int_{\Gamma_{ij}} c u dy \cong c_{ij}\Delta y\left(\theta^{u}_{i+\frac{1}{2}j} u_{i+\frac{1}{2}j} - \theta^{u}_{i-\frac{1}{2}j} u_{i-\frac{1}{2}j}\right) \tag{5.115a}$$

$$\int_{\Gamma_{ij}} c v dx \cong c_{ij}\Delta x\left(\theta^{v}_{ij+\frac{1}{2}} v_{ij+\frac{1}{2}} - \theta^{v}_{ij-\frac{1}{2}} v_{ij-\frac{1}{2}}\right) \tag{5.115b}$$

Changes involve the flux computation as well. For instance, let's consider the liquid flux $G^{F}_{i-\frac{1}{2}j}$ (5.29a) coming from the adjacent cell on the left when $u_{i-\frac{1}{2}j} > 0$ (Fig. 5.15). The liquid of the cell $i-1j$ is marked by the spotted surface. The part limited by the dotted rectangular of is solely taken into account. Its area is assumed to be A. The rectangular size is $\theta^{u}_{i-\frac{1}{2}j}\Delta y \times u_{i-\frac{1}{2}j}\Delta t$ where Δy is the spatial resolution in $y-$axis and $u_{i-\frac{1}{2}j}\Delta t$ corresponds to the travelling path of a fluid particle of a velocity $u_{i-\frac{1}{2}j}$ during a time interval Δt. However, we determine a trapeze so as its area is equal to that of the rectangular thanks to the secant algorithm. The liquid area is now $\widehat{A}$. This results in the flux $G^{F}_{i-\frac{1}{2}j}$ given by the following formula

$$G^{F}_{i-\frac{1}{2}j} = \theta^{u}_{i-\frac{1}{2}j}\Delta y \times u_{i-\frac{1}{2}j}\left(\frac{\widehat{A}}{|\theta^{u}_{i-\frac{1}{2}j}\Delta y \times u_{i-\frac{1}{2}j}\Delta t|}\right) \tag{5.116}$$

with the dimensionless term inside the brackets obtained through the open source VOFTOOLS^{TM}.

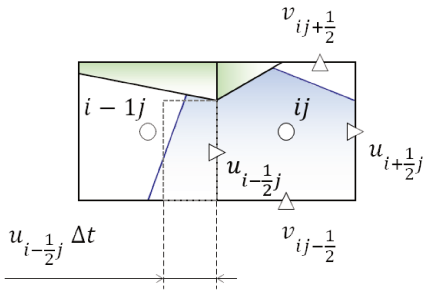

Figure 5.15: Calculation of the flux from the left-hand-side face

We aim to validate the immersed boundary methods by using two well-documented configurations. First, simulations of the flow passing a cylinder are performed to evaluate the one-phase flow solver. Second, for a two-phase flow problem, we analyse a liquid drop placed on a slanted wall. Comparisons are made with other studies found in the literature, collected from Noël 2012 [66].

5.8.1 *Flow passing a circular cylinder*

5.8.1.1 *Description of the flow*

The flow pattern around a still circular solid body is only affected by the Reynolds number, defined from three parameters: the upstream velocity U_∞, the diameter D of the obstacle, the mass density ρ and the dynamic viscosity μ of the fluid.

$$Re = \frac{\rho U_\infty D}{\mu} \tag{5.117}$$

The Reynolds number increases when one carries out each of these four actions: accelerating the flow, amplifying the fluid mass density, reducing the fluid viscosity, or using a larger body size. The change in the flow field due to such a hike in Reynolds number signifies that the latter represents a dimensionless number. Three regimes can be observed.

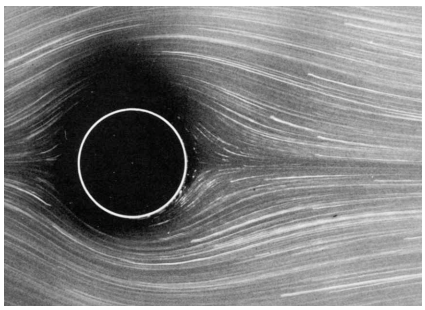

Figure 5.16: Flow passing a circular cylinder at $Re = 1.54$. Streamlines made visible by aluminium powder in water. Photograph by S. Taneda [30]

Regime A corresponds to the described flow at a very low Reynolds number (Fig. 5.16). The symmetry of the streamlines is clear not only around the cylinder's

upper to lower side but also between its front to rear. The flow does not separate at its rear.

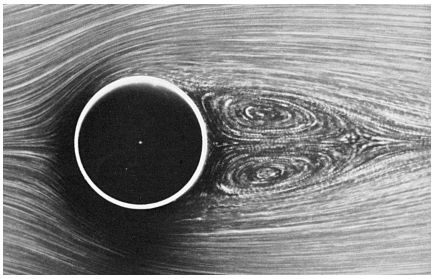

Figure 5.17: Steady vortices at the rear of the cylinder at a higher Reynolds number. Photograph from Rensselaer Polytechnic Institute [79]

Regime B As the Reynolds number increases, the front to rear symmetry disappears, and the interval of the streamlines of the cylinder's rear flow widens. Beyond a critical value of the Reynolds number, a closed region of the streamlines is generated behind the obstacle (see Figure 5.17). The fluid in the upper half of this region rotates clock-wisely while that in the lower half moves in the opposite direction. Twin-vortices are thus created and attach stably to the solid body.

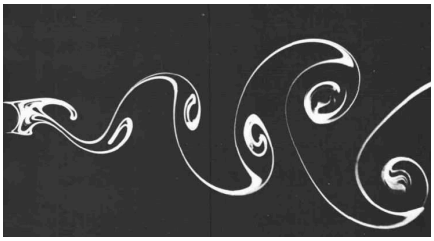

Figure 5.18: Von Karman vortex street behind a circular cylinder at $Re = 140$. Water flowing at 1.4 $cm\ s^{-1}$ past a cylinder of diameter 1 cm. Integrated streamlines shown by electrolytic precipitation of a white colloidal smoke, illuminated by a sheet of light. Photograph by S. Taneda [92]

Regime C The vortex length grows when the Reynolds number is raised further. When the latter exceeds a certain limit, the rear flow becomes unstable and the vortex begins to oscillate up and down (Fig. 5.18). The fully formed vortex is carried away, then expands on the main flow before finally dissipating and leaving the cylinder. In addition, every pair of upper and lower vortices is stored in an alternative regular array to form twin rows of vortices, usually called the von Karman vortex street.

5.8.1.2 *Characteristics of the flow*

Only two flow regimes *B* and *C* are focused on to valid the immersed boundary methods because these test-cases require reasonable computational cost. Moreover, from the experiments of Coutanceau & Bouard 1977 [16] it appears that a transition regime exists within the Reynolds number ranging from 40 to 50. Thus, we first numerically reproduce the flow fields with two moderate Reynolds numbers $Re = 20$ and $Re = 40$ (Fig. 5.17). Then, a higher value of the Reynolds number is considered ($Re = 100$); and the flow pattern should be similar to Fig. 5.18.

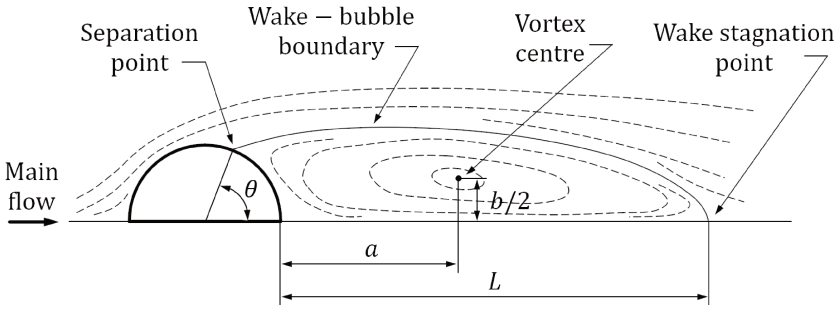

Figure 5.19: The steady separated flow past a circular cylinder (Grove et al. 1964 [44])

We also compare the drag and lift coefficients with other experimental and numerical studies, available in Noël 2012 [66].

$$C_D = \frac{F_x}{\frac{1}{2}\rho U_\infty^2 D} \tag{5.118a}$$

$$C_L = \frac{F_y}{\frac{1}{2}\rho U_\infty^2 D} \tag{5.118b}$$

where F_x and F_y are the total drag and lift, two components of the forces that the fluid acts on the solid body.

$$\mathbf{F}_{f\to s} = \frac{1}{2}\int_0^{2\pi} \sigma \mathbf{n} D \, d\theta \qquad \text{with} \quad \sigma = -p\mathbf{II} + 2\mu\mathbf{D} \tag{5.119}$$

where $\mathbf{II}$ is the identity matrix.

Main features of the vortices such as the position coordinates $(a; b)$ of their centres, the length L of the recirculation zone and the angle θ marking the separation point are equally investigated for the steady flows (Fig. 5.19).

5.8.1.3 *Set-up and results of the test cases*

Consider a solid cylinder of diameter D, placed at the center $(0;0)$ of a rectangular computational domain $[-16D;\ 16D] \times [-8D;\ 8D]$ (Fig. 5.20). For each boundary of the latter, we set the following conditions: Dirichlet on the left, i.e. $U_\infty = 1\ m\ s^{-1}$, outflow on the right and symmetry on the top and on the bottom. Three values of the Reynolds number (5.117) are considered, i.e. $Re = 20$ and $Re = 40$ which correspond to *Regime B* (Fig. 5.17) and $Re = 100$ *Regime C* (Fig. 5.18). The following parameters are fixed in this study: the mass density of the gas $\rho = 1\ kg\ m^{-3}$ and the cylinder diameter $D = 1\ m$ while variations of the dynamic viscosity of the gas $\mu\ Pa\ s$ are allowed to obtain different Reynolds numbers. Concretely, we fix three following values 0.05, 0.25 and 0.01 $Pa\ s$ for the dynamic viscosity to have $Re = 20$, 40 and 100, respectively.

Three meshes are used to discretize the computational domain. The numbers of grid-cells in $x-$ and $y-$ directions are N_x and N_y, respectively. We name the coarsest mesh M1, the intermediate one M2 and the most refined M3, having $N_x \times N_y$ equal to 256×128, 512×256 and 1024×512, respectively.

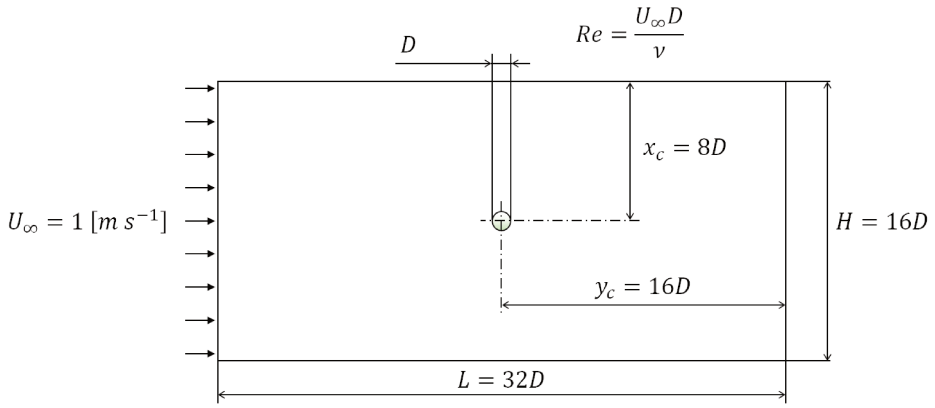

Figure 5.20: Flow around a cylinder - Set-up of the test case

The streamlines at $Re = 40$ are shown in Fig. 5.21 where the vortices can be seen. They are stable and attach to the rear of the cylinder. Figure 5.22 depicts a velocity fields at $Re = 100$. The vector color scales with the velocity magnitude. The von Karman vortex street is produced behind the solid body.

The flow structure obtained by the test cases for *Regime B* at $Re = 20$ and 40 are shown in Tabs. 5.1 and 5.2, respectively. In general, the position and size of the vortex reproduced by the two methods are comparable to the results obtained by

other authors. Furthermore, the drag and lift coefficients of two regimes B and C are close to values found in the literature (Tab. 5.3). For illustration purpose, C_D and C_L are plotted over time in Fig. 5.23. Remark that the drag coefficient at $Re = 100$ reach a stable value after a certain duration while the lift coefficient oscillates around zero.

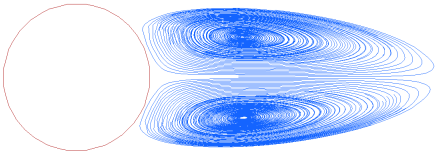

Figure 5.21: Vortices behind the cylinder at $Re = 40$ (FVM M1)

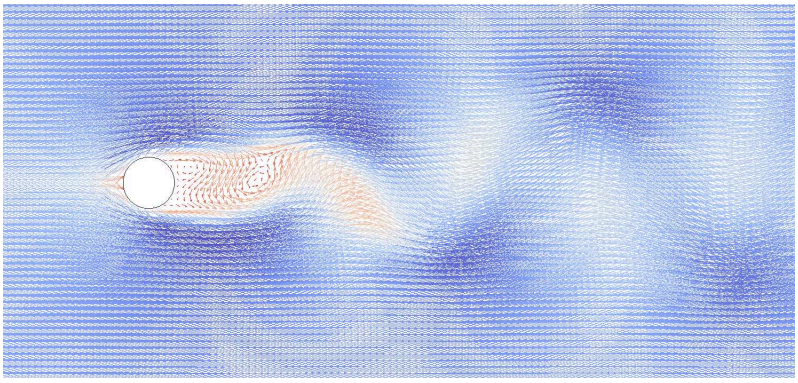

Figure 5.22: Velocity field at $Re = 100$ (FVM M1)

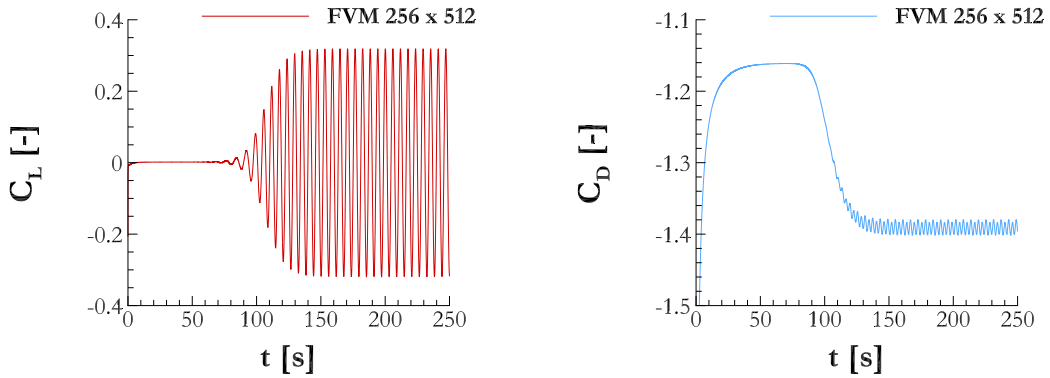

(a) C_L (b) C_D

Figure 5.23: Drag and lift coefficients at $Re = 100$ (FVM M2)

$Re = 20$	L [m]	a [m]	b [m]	θ [°]
Xu 2008 [105]	0.93	0.36	0.43	44
Ye et al. 1999 [107]	0.92	–	–	–
Xie & Desjardin 2008 [104]	1	–	–	43.9
Coutanceau & Bouard 1977 [16] †	0.93	0.33	0.46	45
Xu & Wang 2006 [106]	0.92	–	–	44.2
Choi et al. 2007 [12]	0.90	–	–	40.8
Noël 2012 [66]	0.91	0.336	0.428	45.5
FDM M1	0.90	0.21	0.35	44
FDM M2	0.91	0.25	0.38	42
FDM M3	0.90	0.31	0.40	43
FVM M1	0.90	0.33	0.39	43
FVM M2	0.94	0.32	0.43	48
FVM M3	0.92	0.34	0.42	47

Table 5.1: Flow structure at $Re = 20$ († experimental results)

$Re = 40$	L [m]	a [m]	b [m]	θ [°]
Tseng & Ferziger 2003 [96]	2.21	–	–	–
Ye et al. 1999 [107]	2.27	–	–	–
Xu 2008 [105]	2.24	0.72	0.60	53.8
Choi et al. 2007 [12]	2.25	–	–	51
Coutanceau & Bouard 1977 [16] †	2.13	0.76	0.59	53.8
Xie & Desjardin 2008 [104]	2.26	–	–	54.5
Xu & Wang 2006 [106]	2.21	–	–	53.5
Marella et al. 2005 [57]	2.3	–	–	–
Noël 2012 [66]	2.22	0.7	0.6	50
FDM M1	2.35	0.54	0.53	56
FDM M2	2.25	0.58	0.65	54
FDM M3	2.26	0.57	0.64	52
FVM M1	2.32	0.57	0.66	53
FVM M2	2.34	0.72	0.57	57
FVM M3	2.31	0.69	0.59	57

Table 5.2: Flow structure at $Re = 40$ († experimental results)

	$Re = 20$	$Re = 40$	Re=100	
	C_D	C_D	C_D	C_L
Xu 2008 [105]	2.23	1.66	1.42 ± 0.010	± 0.353
Chiu et al. 2010 [11]	–	1.52	1.35 ± 0.012	± 0.303
Xie & Desjardin 2008 [104]	2.19	1.60	–	–
Wieselsberger 1922 [103] †	2.05	1.70	–	–
Taira & Colonius 2007 [91]	2.06	1.54	–	–
Cheny & Botella 2010 [10]	–	1.50	–	–
Ye et al. 1999 [107]	2.03	1.52	–	–
Choi et al. 2007 [12]	–	–	1.34 ± 0.011	± 0.315
Noël 2012 [66]	2.08	1.54	1.355 ± 0.008	± 0.335
FDM M1	1.69	1.24	1.022 ± 0.003	± 0.2
FDM M2	2.33	1.55	1.255 ± 0.011	± 0.35
FDM M3	2.17	1.57	1.275 ± 0.010	± 0.32
FVM M1	2.12	1.57	1.244 ± 0.004	± 0.17
FVM M2	2.23	1.64	1.391 ± 0.010	± 0.32
FVM M3	2.22	1.62	1.382 ± 0.011	± 0.34

Table 5.3: Lift and drag coefficients at $Re = 20$, 40 and 100 († experimental results)

5.8.2 *Drop on a slanted wall*

In this section, we present some test-cases of a hemispherical liquid drop released at time t_0 on a solid wall without any initial velocity. The wall can be either horizontal and aligned to the mesh axes; or slanted to form with the mesh axes an angle α (Fig. 5.24). The objective of the numerical simulations of the very droplet is to obtain its expected shape at a very large time t_∞. This configuration is previously investigated by Dupont & Legendre 2010 [28]. Different values of the contact angle θ_c are set and it is observed that the contact line moves until an equilibrium state is reached at t_∞. The gravity is assumed to be zero. The final shape of the drop can be analytically obtained thanks to the geometrical consideration and mass conservation.

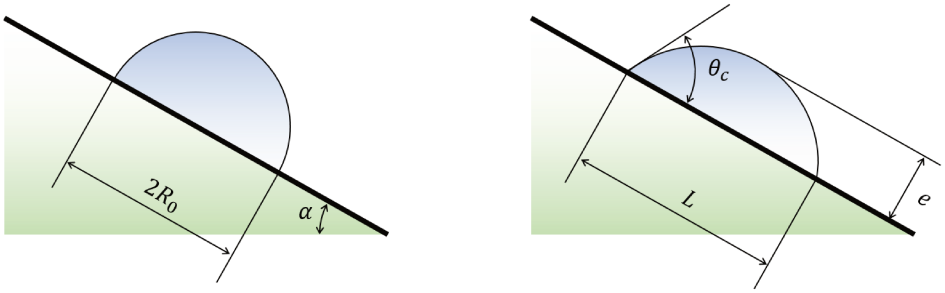

(a) Initial shape at t_0 (b) Final shape at t_∞

Figure 5.24: Drop released on a slanted wall

In our study, four values of the contact angle, i.e. $\theta_c = 30$, 60, 100 and 120 °, are considered. The physical properties of the fluids are as follow. The mass density of liquid and gas are $\rho = 1000$ kg m^{-3} and $\rho_g = 1.204$ kg m^{-3}, respectively. The dynamic viscosity of liquid and gas are $\mu = 1.0\,10^{-3}$ Pa s^{-1} and $\mu_g = 1.78\,10^{-5}$ Pa s^{-1}, respectively. The liquid surface tension is $\sigma = 7.09\,10^{-2}$ N m^{-1}. At the initial moment t_0, the radius of the droplet is $R_0 = 0.32\,10^{-3}$ m. We examine two cases: a horizontal wall ($\alpha = 0$ °) and a slanted wall ($\alpha = 0$ ° and $\alpha = 18$ °). A square computational domain of dimensions 0.004×0.004 m^2 is used. The mesh size is 128×128 with an identical spatial resolution of $\Delta x = \Delta y = 3.125\,10^{-5}$ m in both two directions. Symmetry conditions are set on all boundaries of the computational domain.

The geometrical properties of the liquid drop at its equilibrium state, i.e. its relative depth and width, are plotted with the contact angle in Fig. 5.25. The continuous and dashed lines are the analytical solutions of Dupont & Legendre 2010 [28]. Remark that the finite volume method gives better results than the finite difference method, reproducing drop geometries closer to the theoretical calculations. This can be explained by the fact that the finite volume method is mass-conserving and the theoretical calculations are based on the mass conservation.

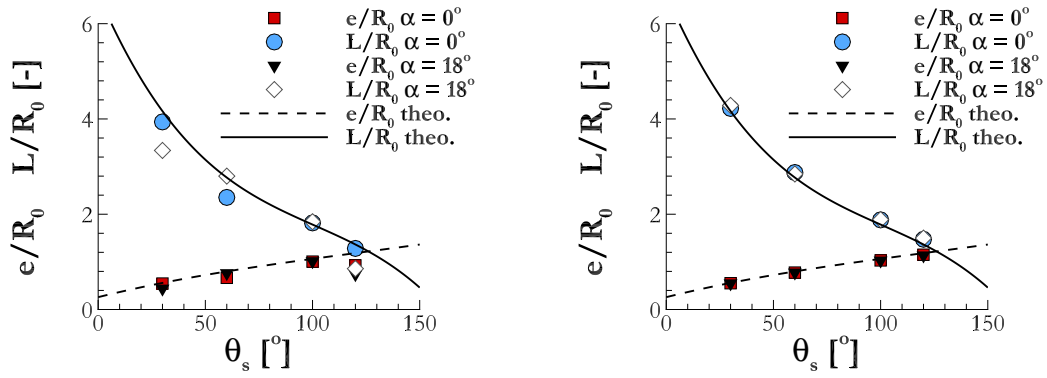

(a) FDM (b) FVM

Figure 5.25: Geometrical properties of a liquid drop deposited on a horizontal and on a slanted solid wall at equilibrium state

The application of the developed methods concerns two complex configurations. The first one is performed on a liquid jet which issued by a cylindrical injector. In the second application, the planar turbulent liquid film produced the triple-disk injector is the object of our simulation.

5.9.1 *Liquid jet emanating from a cylindrical nozzle*

Consider a liquid jet ejected by a cylindrical nozzle. The nozzle has both length and diameter equal to 2.54 mm. At the injector inlet, we impose an uniform velocity profile of 1 ms^{-1}. An outflow condition is set on the other boundaries of the domain. Unlike the treatment of the convection term in § 5.7, we use a different method able to ensure the consistence between the transport of mass and momentum in two-phase flows (Rudman 1998 [81], Vaudor et al. 2017 [99] for instance). The physical properties of the two fluids are summarized in Tab. 5.4. A $12 \times 12 \times 72$ mm^2 box is used as computational domain, which is discretized by a coarse mesh $64 \times 64 \times 384$. An identical spatial resolution in three directions is thus obtained $\Delta x = \Delta y = \Delta z = 0.1875\ 10^{-3}$ m.

	σ $[Nm^{-1}]$	ρ $[kgm^{-3}]$	μ $[Pas^{-1}]$
air	–	1.17	1.78×10^{-5}
liquid	68.51×10^{-3}	1028.54	11×10^{-3}

Table 5.4: Physical properties of the liquid and air

The results of the two methods FDM and FVM are shown in Figs. 5.26 and 5.27, respectively. In these images, the zero-level of the solid level-set function is coloured in grey, that of the liquid-gas interface in blue. The former represents the injector outer wall and the latter the jet surface. We can observe the beginning of the break up of the liquid jet where some perturbations develop on its surface. It appears that a big drop is almost formed at the end of the jet. However, the breakup does not occur at the end of our simulation due to too small computational domain.

Several profiles of the $z-$ velocity component inside and outside the injector are drawn in Figs. 5.28 and 5.29 for the FD and FV methods, respectively. In both

cases, one can notice that the velocity profile at the injector inlet is nearly flat. The value of $z-$ velocity component is very small near the solid wall. In the center of the jet, it keeps almost similar form while moving far from the injector outlet. In the vicinity of the liquid-gas interface, the $z-$ velocity component is reduced. The gas velocity at this location is increased, in particular in front of the jet tip. Notice that the results of the FD and FV methods are close one to another.

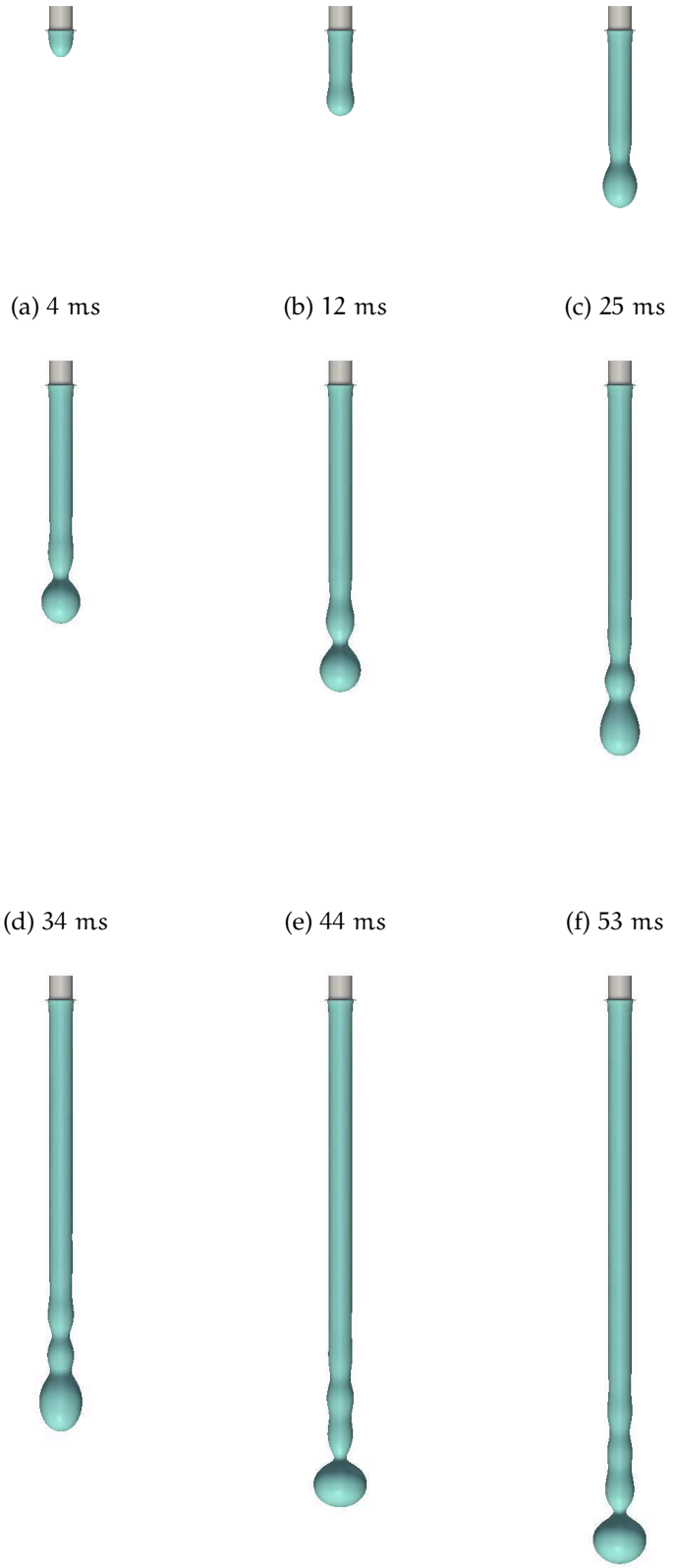

(a) 4 ms (b) 12 ms (c) 25 ms

(d) 34 ms (e) 44 ms (f) 53 ms

(g) 63 ms (h) 75 ms (i) 84 ms

Figure 5.26: Liquid jet issuing from a cylindrical injector - Finite difference method

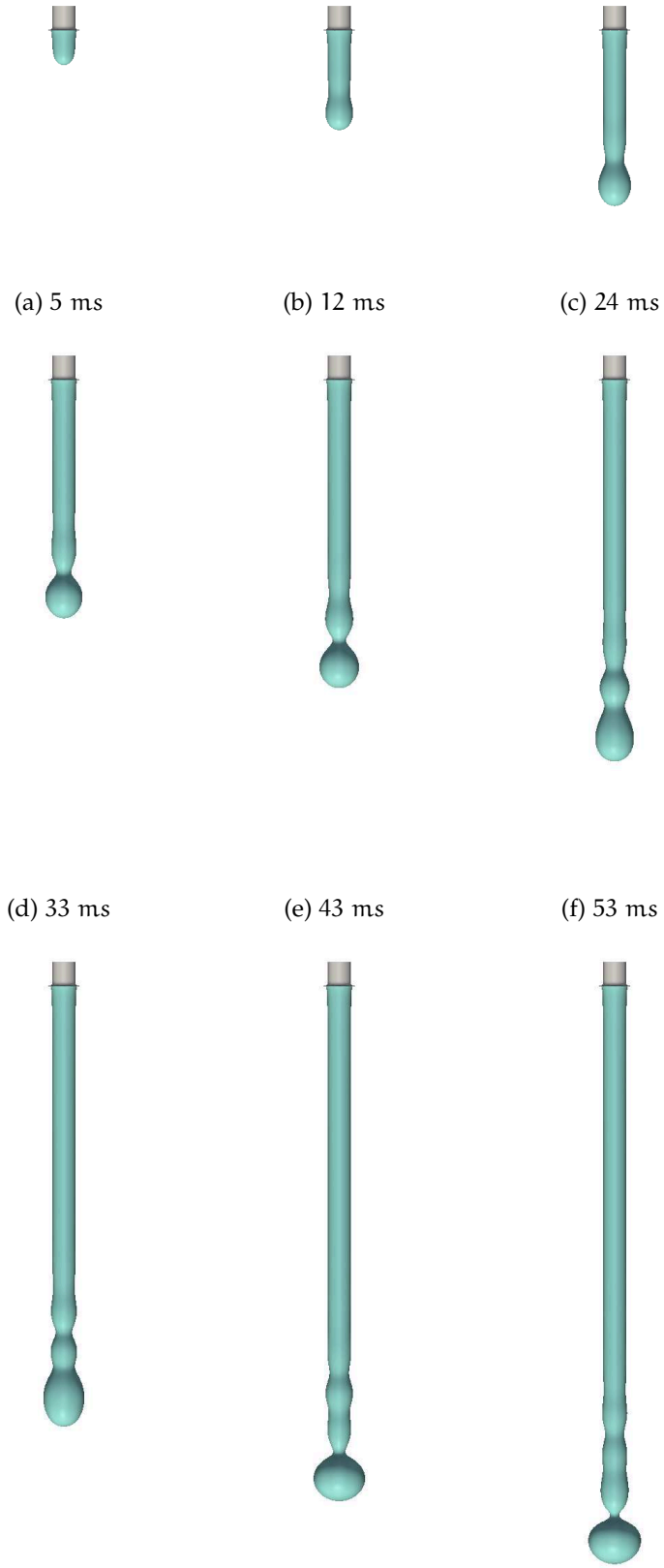

(a) 5 ms (b) 12 ms (c) 24 ms

(d) 33 ms (e) 43 ms (f) 53 ms

(g) 62 ms (h) 74 ms (i) 84 ms

Figure 5.27: Liquid jet issuing from a cylindrical injector - Finite volume method

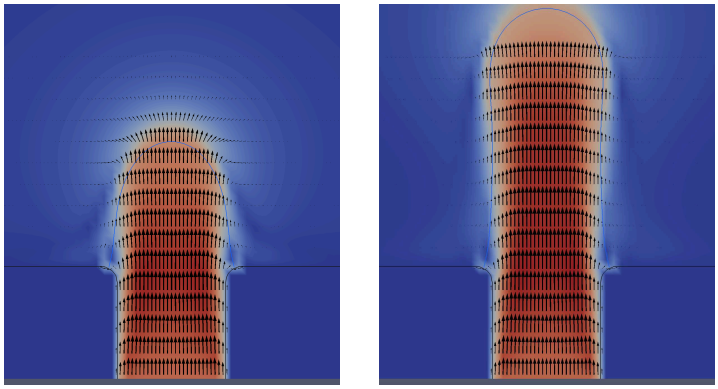

(a) 4.08 ms (b) 7.94 ms

Figure 5.28: Velocity profiles - Liquid jet issuing from a cylindrical injector - FDM

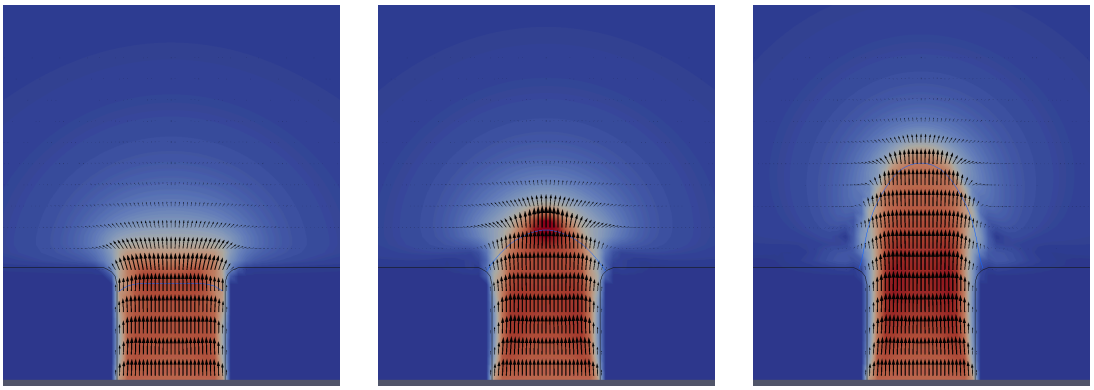

(a) 0.87 ms (b) 1.89 ms (c) 3.36 ms

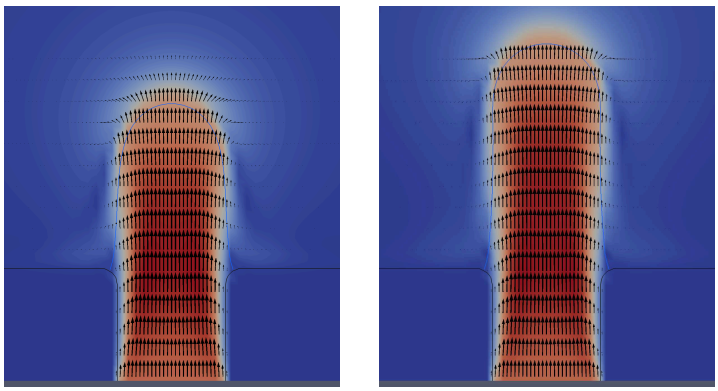

(d) 5.02 ms (e) 6.73 ms

Figure 5.29: Velocity profiles - Liquid jet issuing from a cylindrical injector - FVM

5.9.2 *Liquid sheet produced by a triple-disk injector*

An other numerical simulation is carried out for the turbulent planar liquid sheet issuing from the triple-disk injector. The injector wall is represented by the zero-contour of the solid level-set function (Fig. 5.30).

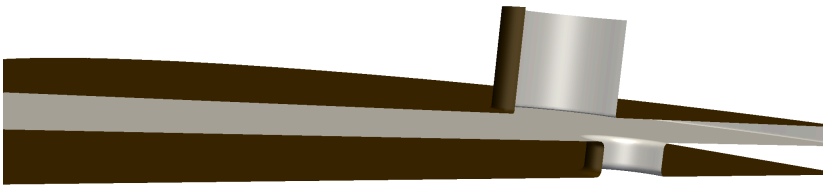

Figure 5.30: Geometry of the triple-disk injector

A difficulty is encountered while transporting the liquid-gas interface across the two borders which connect disk 2 to disk 3; and disk 3 to the outside of the nozzle. In fact, a jump in the normal to the solid boundaries occurs on these borders, provoking an obstacle while imposing the contact angle. These borders are thus rounded, as shown in Fig. 5.31.

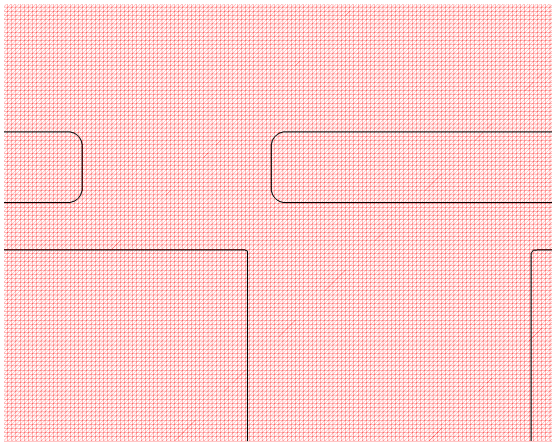

Figure 5.31: Rounded borders of the triple-disk injector

Figure 5.31 also illustrates the mesh used to compute the two-phase flow in this configuration. To put it more precisely, the computational domain is a box measuring $4.52\,10^{-3}$ m. We employ a moderate uniform mesh of $512 \times 512 \times 512$, corresponding to a unique spatial resolution of $\Delta x = \Delta y = \Delta z = 8.83\,10^{-6}$ m in all directions. The number of grid points across the injector outlet is approximately 45. Remark that the resolution is higher than the cell-size near the solid wall in Cousin et al. 2013 [15] who perform a large-eddy simulation for the flow

developing inside a smaller triple-disk injector. We execute a parallel computation with 512 processors. At the injector inlet, we impose an inflow condition with an uniform velocity which gradually increases in time as follow.

$$U_{inlet}(t) = \min(0.9\ V_q^{inlet}\, t + 0.1\, V_q^{inlet},\ V_q^{inlet}) \tag{5.120}$$

where t ms is time, $V_q^{inlet} = 3.98\ m\ s^{-1}$ the average inlet velocity of the liquid Fo (refer to Tab. 3.2 for the metering velocity at the injector outlet). The objective of this setting is to slowly increase the velocity so that the internal and external flows are well established. We set an outflow condition on the other borders of the computational domain.

Figures 5.32 and 5.33 present how the liquid-gas interface evolves at the beginning of the breakup process. A 2D sheet is formed near the outlet section. At the early instants, the liquid film is smooth, having a thin center part bounded by a thick border. Remember that the inlet velocity is kept small at these moments. Later on, the sheet spreads and some perturbations develop at both edges. The sheet is lightly deviated, similar to the experimental results (Fig. 3.6). Also, it has a rim thicker than another. Yet, holes appears in the center of the liquid film, unlike the experimental results of chapter 3. Seemingly, the sheet breaks up in the perforation mode because of the growth of these holes.

In Fig. 5.34, the velocity fields inside the discharge orifice are shown at three cutting planes. The velocity magnitude is drawn on the left-hand side whereas the non-axial velocity vectors on the right-hand side. The lowest cutting plane corresponds to the entrance of disk 3 from disk 2; and the highest one a position close to the injector outlet. The intermediate section is located in the middle of these two planes. At an early moment 0.37 ms, the double vortices can be noticed from Fig. 5.34a, in agreement with the literature in § 2.2.2.4. The boundary layer develops from the entrance of disk 3 to the injector exit. One can observe, at a later instant 0.71 ms, the liquid-gas interface (Fig. 5.34b). This indicates that gas enters into disk 3. The interface is large near the injector outlet. At the entrance of disk 3, its size is reduced. Notice a diminution of the boundary layer when the interface appears at this moment.

For the sake of clarity, we plot the shape of the liquid-gas interface inside the injector in Fig. 5.35a. Clearly, the interface even penetrates into disk 2 and almost

is in contact with the upper wall of the latter at 0.71 ms. Remark that at this time, a double hollow sheet is formed in two sides of a principal planar liquid film. This suggests that the swirl at the outlet section is very strong. In Fig. 5.35b, the $z-$ velocity component is plotted together with the liquid-gas interface in a cutting plane. The latter is perpendicular to the plane of symmetry of the injector and can be seen from Fig. 5.35a. The velocity of the gas which goes into the nozzle is of the same order as that of the ejected liquid moving in the opposite direction. The penetration of the gas inside the triple-disk injector, as reported by our numerical results, seems to be open for discussion as no previous study reports such behaviours.

In Fig. 5.36, we depict the velocity fields and the interface in the plane of symmetry of the triple-disk injector at two instants. Notice that the boundary layer is thin and complex, requiring an appropriate treatment of the near-wall flow.

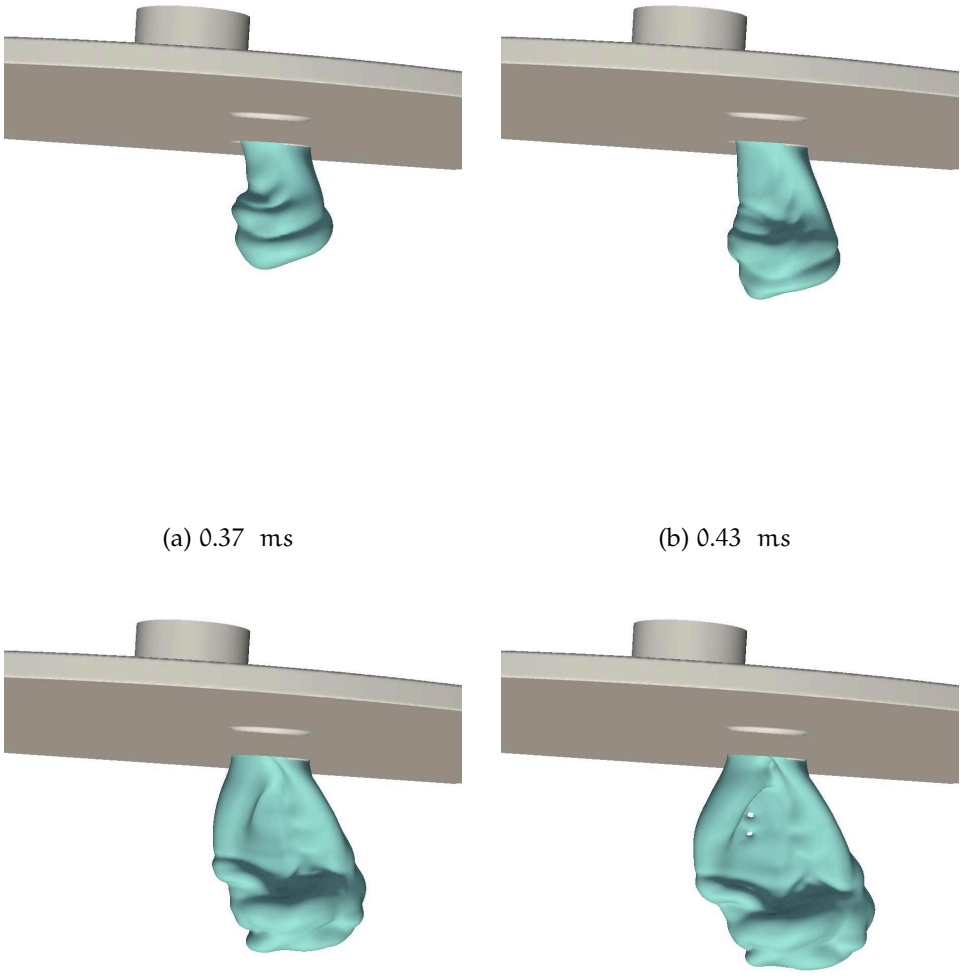

(a) 0.37 ms (b) 0.43 ms

(c) 0.51 ms (d) 0.54 ms

Figure 5.32: Temporal evolution of the liquid-gas interface (1)

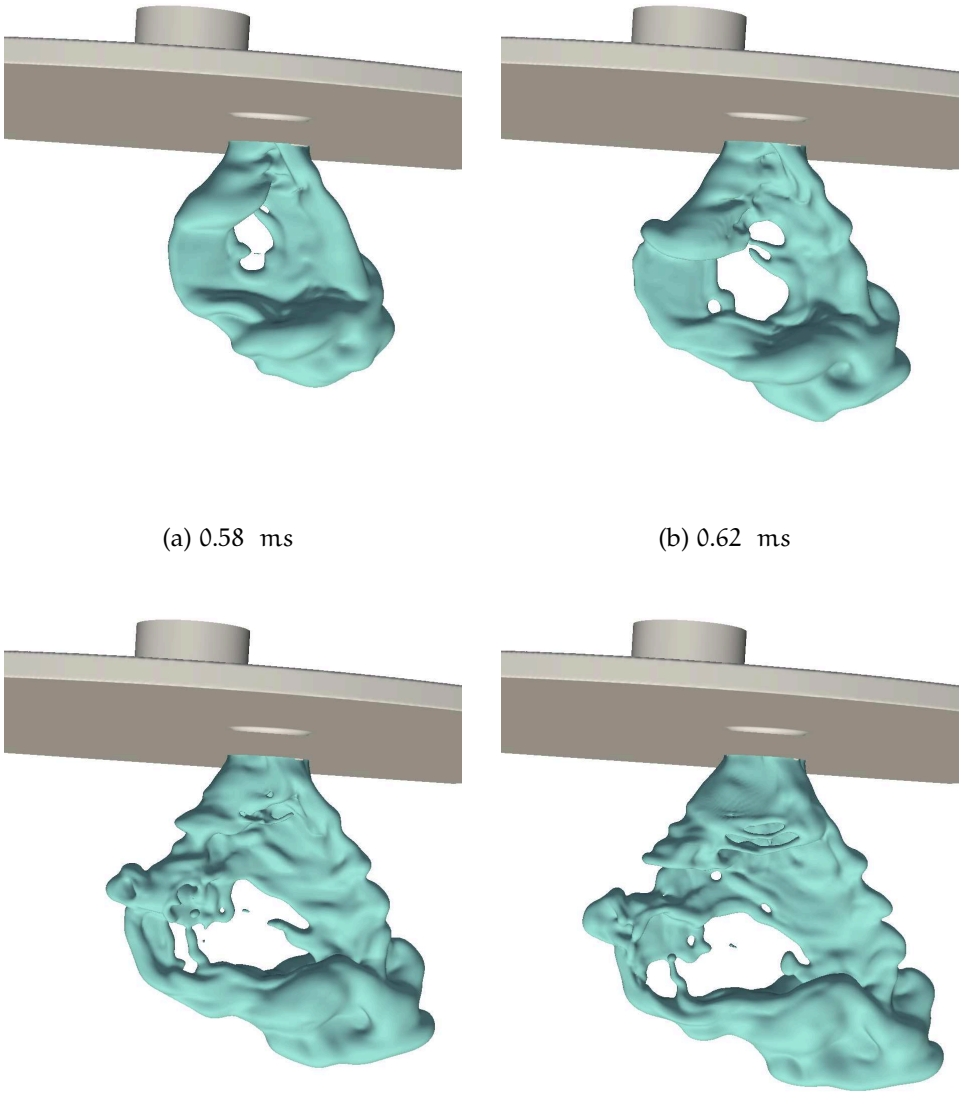

(a) 0.58 ms (b) 0.62 ms

(c) 0.67 ms (d) 0.71 ms

Figure 5.33: Temporal evolution of the liquid-gas interface (2)

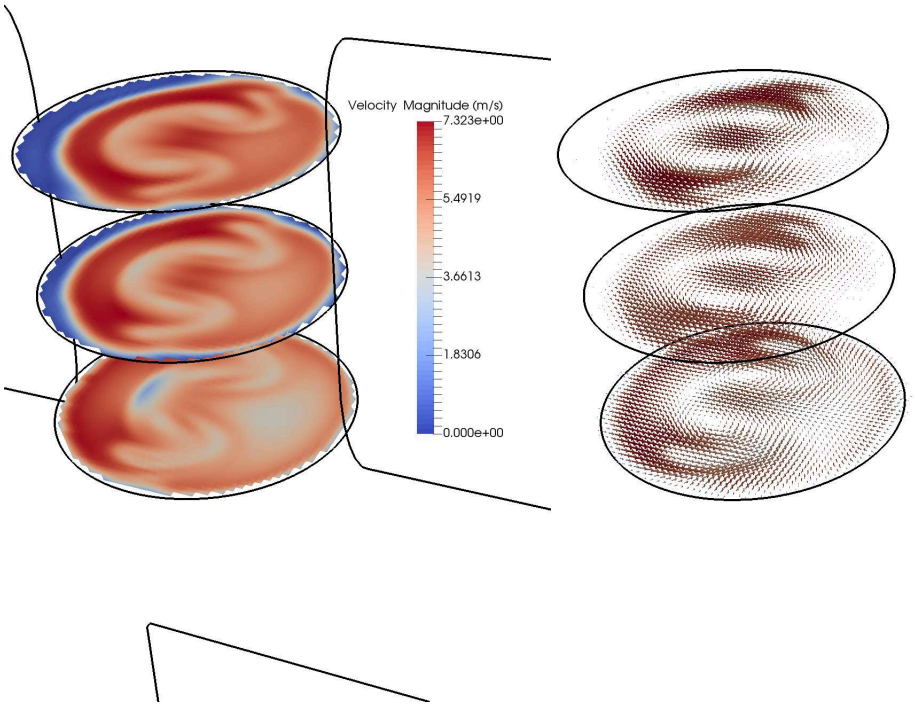

(a) 0.37 ms

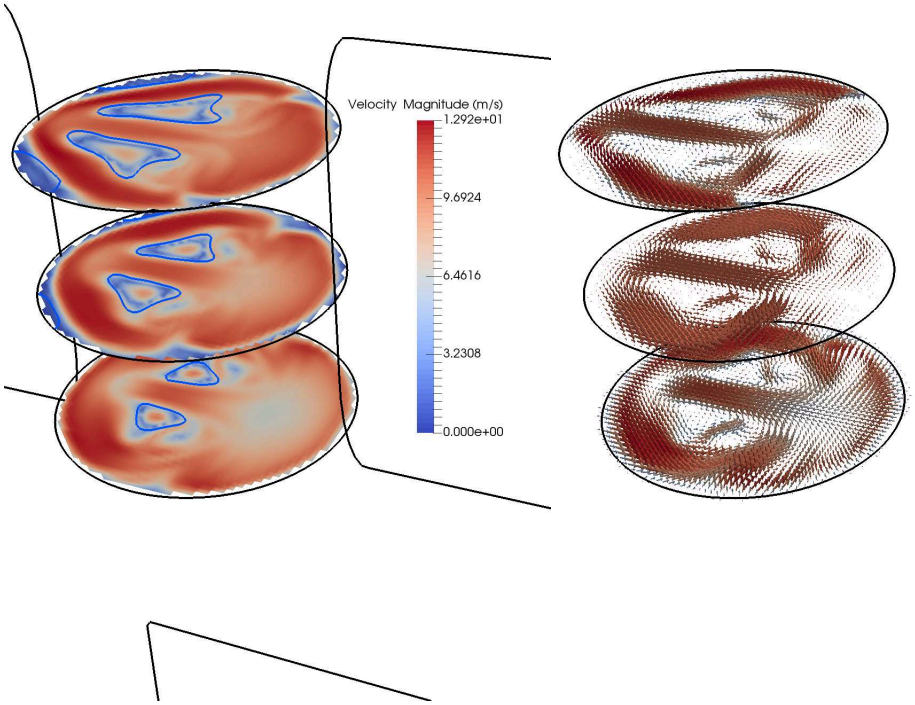

(b) 0.71 ms

Figure 5.34: Velocity field and liquid-gas interface in disk 3

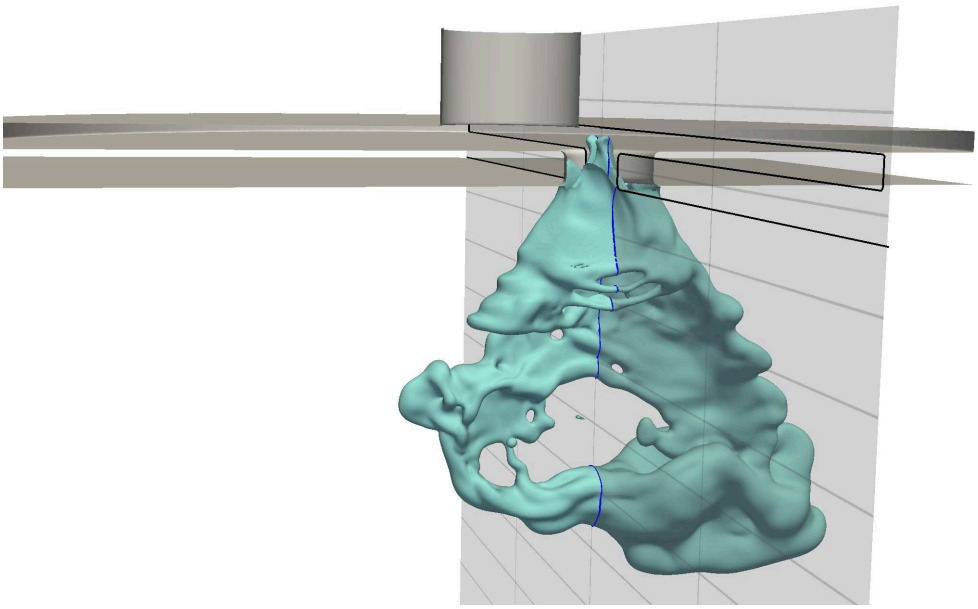

(a) Liquid-gas interface and a cutting plane

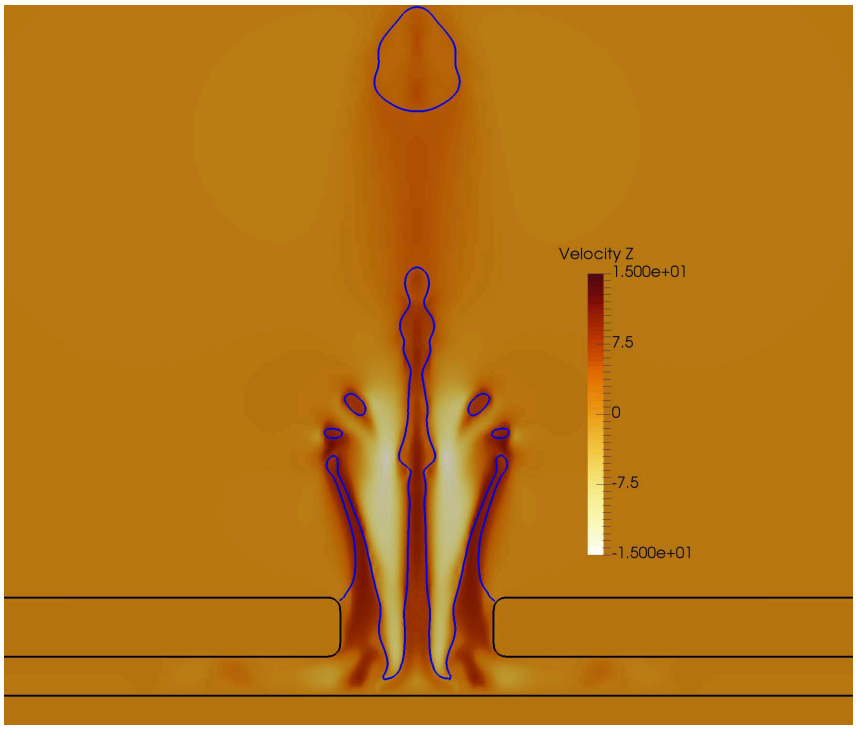

(b) Liquid-gas interface and velocity field at the cutting plane

Figure 5.35: Gas penetration inside the triple-disk injector at 0.71 ms

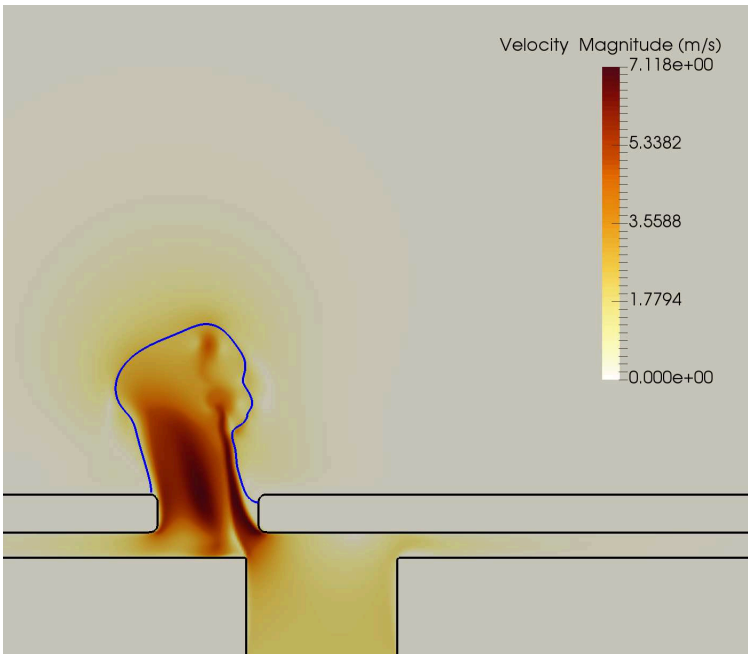

(a) 0.37 ms

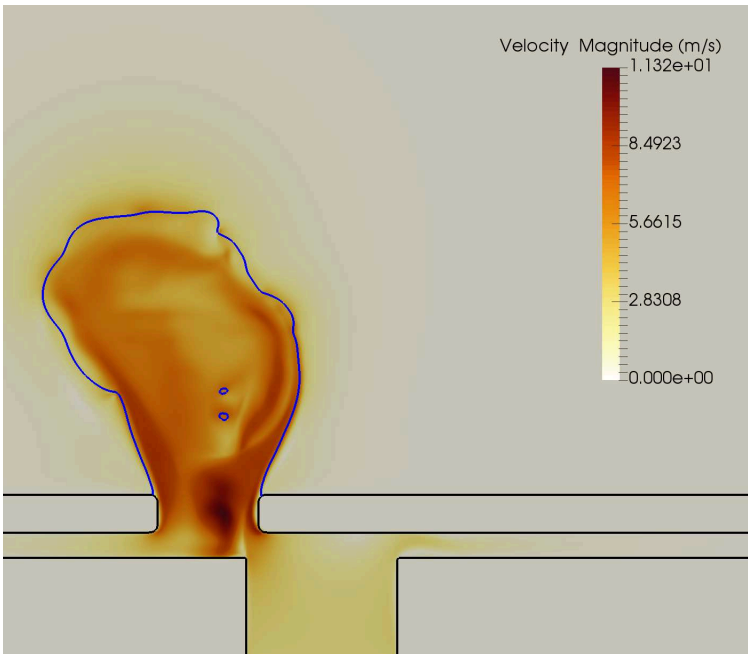

(b) 0.54 ms

Figure 5.36: Velocity field and liquid-gas interface in a cutting plane

6

CONCLUSIONS & PERSPECTIVES

This present study gathers some experimental analyses and numerical developments which aim to investigate the atomization process of the planar turbulent liquid sheets emanating from a triple-disk injector. The atomizer consists of three superposed disks having each a circular orifice hole. Moreover, the discharge orifice is deviated from the injector axis. Given this particular design, a complex internal flow is created. In effect, a double counter-rotating vortex is formed at the injector outlet, together with a consistent turbulence level. The double counter swirl stretches the flow to create a 2D film in the plane of symmetry of the injector. Meanwhile, the turbulence induces some perturbations that develop at the sheet edges. A ligament network appear and eventually breaks down into droplets.

As the very first step, to understand the disintegration of the liquid film, a backlight optical set-up is built to record the sheet images. These visual results are then processed under a multi-scale tool which enables the atomization analysis to be carried out. The use of the multi-scale approach is justified by the finding in the literature that mechanisms of liquid-gas interface evolution occur in a wide range of time and length scales. The main results of our experimental analyses are twofold and can be summarized as follows.

First, the contraction of the liquid film is affected by the perturbations appearing on its borders. This interaction could be inspected by two characteristic time scales - one representing the sheet contraction, the other specifying the development of the disturbances. While the first time scale depends on the sheet opening angle, the second scale varies with the surface tension coefficient. According to the relationship between these characteristic times, the perturbations more or less strongly influence the contraction of the liquid sheet.

Second, the multi-scale analysis allows an estimation of the ligaments' geometrical properties to be made. As for an individual ligament whose geometry changes in time, three involved mechanisms, i.e. stretching, capillary contraction and produc-

tion, are proposed for analysing the deformation of the ligament network. These mechanisms can be identified thanks to the variation rates of the specific length and the perimeter of the liquid threads. It is found that the stretching of the ligaments favours the poly-dispersion of the spray and the formation of fine droplets. Additionally, the fact that the drops are dispersed in diameter can be due to a high turbulence level which causes the snapshot-to-snapshot fluctuations or the elongation of the ligaments.

Interesting results not withstanding, some further explorations should be brought to the analysis to derive more benefits. First of all, for each image and each analysing window, cumulative scale distribution should be used to compute the corresponding scale distribution. The latter, together with the total surface area, enables the perimeter distribution of the eroded systems to be found. It can be expected that the temporal variations of the perimeter distribution give useful information about the snapshot-to-snapshot fluctuations of the liquid structures.

Next, based on the calculation of a maximum scale d_{max} for each image and each analysing window via the instantaneous cumulative scale distributions, the average value and the standard deviation of these maximum scales reflect the behaviours of the bulk of the liquid film.

Furthermore, isolating the ligament network from the liquid system could be done directly by the image processing. Thanks to the specific scale d_L, statistically detected or image by image, the ligaments can be easily erased by an opening operator at the very scale. The initial system is then subtracted by the resulting one to obtain only the liquid threads. Therefore, with the images of the latter available, the deformation of the ligaments could be examined in detail.

The other major part of the thesis involves the numerical works to simultaneously compute the nozzle flow and the film breakup in a unique simulation. As mentioned above, the internal flow has a significant impact on the sheet disintegration. It is claimed in the previous studies that the stronger the double swirl, the larger the liquid film. The thickness of the latter is thus reduced to yield small drops. Moreover, turbulence intensity is increased by the wall friction to promote the perturbations on the sheet edges. Near the nozzle exit, ligaments are more numerous, smaller in size and may divide into finer droplets.

The connection between the internal and external flows is implemented through two immersed boundary methods. The first one is based on the finite difference method and the second the finite volume method. In the Cartesian grid framework, these approaches are able to account for the irregular solid frontier. Moreover, when combined with a coupled level-set/volume-of-fluid method, these two immersed boundary methods can compute two-phase flows. Specifically, to avoid the constraint on the time step, the diffusion term is implicitly calculated in both cases. It is seen that the finite volume method is more suitable to track the liquid-gas interface inside the cut-cells by the volume-of-fluid method and thus mass-conserving. For validation purpose, numerical results are compared to the previous works in the literature and the analytical solutions.

The application of the developed methods concerns two complex configurations. The first one is performed on a liquid jet which issued by a cylindrical injector. Both finite difference and finite volume methods give similar results, reproducing the beginning of the instability of the jet. However, the rupture of the latter is not observed due to insufficient computational domain. In the second application, the planar turbulent liquid film produced by the triple-disk injector is the object of our simulation. It is shown that the implemented code is able to simultaneously take into consideration the internal and external flows. Nevertheless, the numerical results are still unsatisfactory, showing differences from the experimental ones. This suggests that further developments should be done in the future, concerning in particular turbulence modelling and specific treatment of the wall boundary layer. Furthermore, a detailed comparison could be made for the two-phase flow in the same injector geometry and operating conditions as those of Cousin et al. 2013 [15].

BIBLIOGRAPHY

[1] A. Arakawa. "Computational design for long-term numerical integration of the equations of fluid motion: Two-dimensional incompressible flow. Part I." In: *J. Comput. Phys.* 1.1 (1966), pp. 119–143.

[2] T. D. Aslam. "A partial differential equation approach to multidimensional extrapolation." In: *J. Comput. Phys.* 193.1 (2004), pp. 349–355.

[3] D. Bérubé and M. Jébrak. "High precision boundary fractal analysis for shape characterization." In: *Comput. Geosci.* 25.9 (1999), pp. 1059–1071.

[4] J. B. Blaisot and J. Yon. "Droplet size and morphology characterization for dense sprays by image processing: application to the Diesel spray." In: *Exp. Fluids* 39.6 (2005), pp. 977–994.

[5] N. Brémond. "Stabilité et atomisation des nappes liquides." PhD thesis. Université de Provence, 2003.

[6] N. Brémond and E. Villermaux. "Atomization by jet impact." In: *J. Fluid Mech.* 549 (2006), pp. 273–306.

[7] M. P. Brenner, J. Eggers, K. Joseph, S. R. Nagel, and X. D. Shi. "Breakdown of scaling in droplet fission at high Reynolds number." In: *Phys. Fluids* 9 (1997).

[8] F. Charru. *Hydrodynamic instabilities*. Cambridge University Press, 2011.

[9] J. L. Chen, M. Wells, and J. Creehan. "Primary atomization and spray analysis of compound nozzle gasoline injectors." In: *J. Eng. Gas Turbines Power* 120.1 (1998), pp. 237–243.

[10] Y. Cheny and O. Botella. "The LS-STAG method: A new immersed boundary/level set method for the computation of incompressible viscous flows in complex moving geometries with good conservation properties." In: *J. Comput. Phys.* 229.4 (2010), pp. 1043–1076.

[11] P. H. Chiu, R. K. Lin, and T. W. H. Sheu. "A differentially interpolated direct forcing immersed boundary method for predicting incompressible Navier–Stokes equations in time-varying complex geometries." In: *J. Comput. Phys.* 229.12 (2010), pp. 4476–4500.

[12] J. I. Choi, R. C. Oberoi, J. R. Edwards, and J. A. Rosati. "An immersed boundary method for complex incompressible flows." In: *J. Comput. Phys.* 224.2 (2007), pp. 757–784.

[13] A. J. Chorin. "Numerical solution of the Navier-Stokes equations." In: *Math. Comput.* 22.104 (1968), pp. 745–762.

[14] C. Clanet and E. Villermaux. "Life of a smooth liquid sheet." In: *J. Fluid Mech.* 462 (2002), pp. 307–340.

[15] J. Cousin, A. Berlemont, T. Ménard, and S. Grout. "Primary breakup simulation of a liquid jet discharged by a low-pressure compound nozzle." In: *Comput. Fluids* 63 (2012), pp. 165–173.

[16] M. Coutanceau and R. Bouard. "Experimental determination of the main features of the viscous flow in the wake of a circular cylinder in uniform translation. Part 1. Steady flow." In: *J. Fluid Mech.* 79.02 (1977), p. 231.

[17] N. Dombrowski, D. Hasson, and D. E. Ward. "Some aspects of liquid flow through fan spray nozzles." In: *Chem. Eng. Sci.* 12.1 (1960), pp. 35–50.

[18] N. Dombrowski and W. R. Johns. "The aerodynamic instability and disintegration of viscous liquid sheets." In: *Chem. Eng. Sci.* 18.3 (1963), pp. 203–214.

[19] C. Dumouchel. "On the experimental investigation on primary atomization of liquid streams." In: *Exp. Fluids* 45.3 (2008), pp. 371–422.

[20] C. Dumouchel. "Liquid atomization and spray: a multi-scale description." In: Hawaii, USA, 2017.

[21] C. Dumouchel, J. Cousin, and S. Grout. "Analysis of two-dimensional liquid spray images: the surface-based scale distribution." In: *J. Flow Vis. Image Process* 15.1 (2008), pp. 59–83.

[22] C. Dumouchel, J. Cousin, and K. Triballier. "On the role of the liquid flow characteristics on low-Weber-number atomization processes." In: *Exp. Fluids* 38.5 (2005), pp. 637–647.

[23] C. Dumouchel and S. Grout. "Application of the scale entropy diffusion model to describe a liquid atomization process." In: *Int. J. Multiph. Flow* 35.10 (2009), pp. 952–962.

[24] C. Dumouchel and S. Grout. "On the scale diffusivity of a 2D liquid atomization process analysis." In: *Physica A: Phys. Stat. Mech. Its Appl.* 390.10 (2011), pp. 1811–1825.

[25] C. Dumouchel, T. Ménard, and W. Aniszewski. "Towards an interpretation of the scale diffusivity in liquid atomization process: An experimental approach." In: *Physica A: Phys. Stat. Mech. Its Appl.* 438 (2015), pp. 612–624.

[26] C. Dumouchel, J. B. Blaisot, E. Bouche, T. Ménard, and T. T. Vu. "Multiscale analysis of atomizing liquid ligaments." In: *Int. J. Multiph. Flow* 73 (2015), pp. 251–263.

[27] C. Dumouchel, W. Aniszewski, T. T. Vu, and T. Ménard. "Multi-scale analysis of simulated capillary instability." In: *Int. J. Multiph. Flow* 92 (2017), pp. 181–192.

[28] J. B. Dupont and D. Legendre. "Numerical simulation of static and sliding drop with contact angle hysteresis." In: *J. Comput. Phys.* 229.7 (2010), pp. 2453–2478.

[29] B. Duret. "Simulation numérique directe des écoulements liquide-gaz avec évaporation: Application à l'atomisation." PhD thesis. Institut national des sciences appliquées de Rouen, 2013.

[30] M. V. Dyke. *Album of fluid motion*. 14th edition. Stanford, California: Parabolic Press, Inc., 2012.

[31] J. Eggers. "Nonlinear dynamics and breakup of free-surface flows." In: *Rev. Mod. Phys.* 69.3 (1997), pp. 865–930.

[32] J. Eggers and E. Villermaux. "Physics of liquid jets." In: *Rep. Prog. Phys.* 71.3 (2008), p. 036601.

[33] L. W. Evers. "Analogy between atomization and vaporization based on the conservation of energy." In: *SAE* 940190 (1994).

[34] R. Eymard, T. Gallouet, and R. Herbin. *Finite volume methods*. Vol. 7. Elsevier, 2000.

[35] N. Fdida and J. B. Blaisot. "Drop size distribution measured by imaging: determination of the measurement volume by the calibration of the point spread function." In: *Meas. Sci. Technol.* 21.2 (2010), p. 025501.

[36] R. P. Fedkiw, T. Aslam, B. Merriman, and S. Osher. "A non-oscillatory eulerian approach to interfaces in multimaterial flows (the ghost fluid method)." In: *J. Comput. Phys.* 152.2 (1999), pp. 457–492.

[37] R. P. Fraser, P. Eisenklam, N. Dombrowski, and D. Hasson. "Drop formation from rapidly moving liquid sheets." In: *AIChE J.* 8.5 (1962), pp. 672–680.

[38] F. Gibou and C. Min. "Efficient symmetric positive definite second-order accurate monolithic solver for fluid/solid interactions." In: *J. Comput. Phys.* 231.8 (2012), pp. 3246–3263.

[39] F. Gibou, R. P. Fedkiw, L. T. Cheng, and M. Kang. "A second-order-accurate symmetric discretization of the Poisson equation on irregular domains." In: *J. Comput. Phys.* 176.1 (2002), pp. 205–227.

[40] M. L. Glodowski, D. J. Michalek, and L. W. Evers. "The use of results from computational fluid dynamic fuel injector modeling to predict spray characteristics." In: *SAE* 961191 (1996).

[41] E. F. Goedde and M. C. Yuen. "Experiments on liquid jet instability." In: *J. Fluid Mech.* 40.03 (1970), pp. 495–511.

[42] S. Grout. "Analyse multi-échelle des processus d'atomisation et des sprays. Application aux injecteurs triple disque." PhD thesis. Université de Rouen, 2009.

[43] S. Grout, C. Dumouchel, J. Cousin, and H. Nuglisch. "Fractal analysis of atomizing liquid flows." In: *Int. J. Multiph. Flow* 33.9 (2007), pp. 1023–1044.

[44] A. S. Grove, F. H. Shair, and E. E. Petersen. "An experimental investigation of the steady separated flow past a circular cylinder." In: *J. Fluid Mech.* 19.1 (1964), p. 60.

[45] W. W. Hagerty and J. F. Shea. "A study of the stability of plane fluid sheets." In: *J. Appl. Mech.* 22 (1955), pp. 509–514.

[46] F. H. Harlow and J. E. Welch. "Numerical calculation of time-dependent viscous incompressible flow of fluid with free surface." In: *Phys. Fluids* 8.12 (1965), pp. 2182–2189.

[47] J. Heyse, F. Schatz, B. Ader, J. Schlerfer, and S. Haubold. "Electroformed multilayer orifice plate for improved fuel injection characteristics." In: *SAE* 971070 (1997).

[48] C. W. Hirt and B. D. Nichols. "Volume-of-fluid (VOF) method for the dynamics of free boundaries." In: *J. Comput. Phys.* 39.1 (1981), pp. 201–225.

[49] J. C. P. Huang. "The break-up of axisymmetric liquid sheets." In: *J. Fluid Mech.* 43.02 (1970), pp. 305–319.

[50] T. A. Kowalewski. "On the separation of droplets from a liquid jet." In: *Fluid Dyn. Res.* 17.3 (1996), pp. 121–145.

[51] A. H. Lefebvre. *Atomization and sprays*. New York, USA: Hemisphere Publishing Corporation, 1989.

[52] M. Lepilliez, E. R. Popescu, F. Gibou, and S. Tanguy. "An efficient two-phase flow solver in irregular domains." In: *Prepr. Submitt. J. Comput. Phys.* (2015), pp. 1–45.

[53] X. D. Liu, R. P. Fedkiw, and M. Kang. "A boundary condition capturing method for Poisson's equation on irregular domains." In: *J. Comput. Phys.* 160.1 (2000), pp. 151–178.

[54] J. López and J. Hernández. "Analytical and geometrical tools for 3D volume of fluid methods in general grids." In: *J. Comput. Phys.* 227.12 (2008), pp. 5939–5948.

[55] J. López, J. Hernández, P. Gómez, and F. Faura. "An improved PLIC-VOF method for tracking thin fluid structures in incompressible two-phase flows." In: *J. Comput. Phys.* 208.1 (2005), pp. 51–74.

[56] A. Mansour and N. Chigier. "Dynamic behavior of liquid sheets." In: *Phys. Fluids A: Fluid Dynamics* 3.12 (1991), pp. 2971–2980.

[57] S. Marella, S. Krishnan, H. Liu, and H. S. Udaykumar. "Sharp interface Cartesian grid method I: An easily implemented technique for 3D moving boundary computations." In: *J. Comput. Phys.* 210.1 (2005), pp. 1–31.

[58] P. Marmottant and E. Villermaux. "Fragmentation of stretched liquid ligaments." In: *Phys. Fluids* 16.8 (2004), pp. 2732–2741.

[59] T. Ménard. "Développement d'une méthode level-set pour le suivi d'interface. Application à la rupture de jet liquide." PhD thesis. Université de Rouen, 2007.

[60] T. Ménard, S. Tanguy, and A. Berlemont. "Coupling level-set/VOF/ghost-fluid method: validation and applications to 3D simulations of jet primary break-up." In: *Int. J. Multiph. Flow.* 33 (2007), pp. 511–524.

[61] D. J. Michalek, B. D. Peschke, and L. W. Evers. "Computational design of experiments for compound fuel injector nozzles." In: *SAE* 971617 (1997).

[62] F. A. Morrison. *An introduction to fluid mechanics*. Cambridge University Press, 2013.

[63] K. Nagasaka, T. Takagi, K. Koyanagi, and T. Yamauchi. "The development of fine atomization injector." In: *JSAE Rev.* 21.3 (2000), pp. 309–313.

[64] V. D. Ngô. "Etude de la morphologie des éléments d'un spray liquide et de leur production." PhD thesis. Université de Rouen, 2013.

[65] Y. T. Ng, C. Min, and F. Gibou. "An efficient fluid–solid coupling algorithm for single-phase flows." In: *J. Comput. Phys.* 228.23 (2009), pp. 8807–8829.

[66] E. Noël. "Simulation numérique directe d'écoulements à l'aide d'une méthode de frontière immergée." PhD thesis. Université de Rouen, 2012.

[67] B. Oesterlé. *Ecoulements multiphasiques: Des fondements aux méthodes d'ingénierie*. Hermes Science Publications, 2006.

[68] A. Okajima. "Strouhal numbers of rectangular cylinders." In: *J. Fluid Mech.* 123 (1982), pp. 379–398.

[69] S. Osher and J. A. Sethian. "Fronts propagating with curvature-dependent speed: Algorithms based on Hamilton-Jacobi formulations." In: *J. Comput. Phys.* 79.1 (1988), pp. 12–49.

[70] D. T. Papageorgiou. "On the breakup of viscous liquid threads." In: *Phys. Fluids* 7.7 (1995), pp. 1529–1544.

[71] S. Parrish and L. Evers. "Spray characteristics of compound silicon micro machined port fuel injector orifices." In: *SAE* 950510 (1995).

[72] J. E. Pilliod Jr. and E. G. Puckett. "Second-order accurate volume-of-fluid algorithms for tracking material interfaces." In: *J. Comput. Phys.* 199.2 (2004), pp. 465–502.

[73] W. T. Pimbley and H. C. Lee. "Satellite droplet formation in a liquid jet." In: *IBM J. Res. Dev.* 21.1 (1977), pp. 21–30.

[74] J. Plateau. In: *Acad. Sci. Bruxelles Mém.* 23 (1849), p. 5.

[75] E. G. Puckett, A. S. Almgren, J. B. Bell, D. L. Marcus, and W. J. Rider. "A high-order projection method for tracking fluid interfaces in variable density incompressible flows." In: *J. Comput. Phys.* 130.2 (1997), pp. 269–282. (Visited on 2015).

[76] D. Queiros-Conde, F. Foucher, C. Mounaïm-Rousselle, H. Kassem, and M. Feidt. "A scale-entropy diffusion equation to describe the multi-scale features of turbulent flames near a wall." In: *Phys. Stat. Mech. Its Appl.* 387.27 (2008), pp. 6712–6724.

[77] D. Queiros–Conde. "A diffusion equation to describe scale– and time–dependent dimensions of turbulent interfaces." In: *Proc. R. Soc. Lond. A* 459.2040 (2003), pp. 3043–3059.

[78] L. Rayleigh. "On the capillary phenomena of jets." In: *Proc. R. Soc. Lond.* 29.196-199 (1879), pp. 71–97.

[79] USA Rensselaer Polytechnic Institute New York. *Flow past a cylinder*. URL: http://www.rpi.edu.

[80] F. Risso. "The mechanisms of deformation and breakup of drops and bubbles." In: *Multiphas. Sci. Tech.* 12 (2000), pp. 1–50.

[81] M. Rudman. "A volume-tracking method for incompressible multifluid flows with large density variations." In: *Int. J. Numer. Meth. Fluids* 28.2 (1998), pp. 357–378.

[82] D. F. Rutland and G. J. Jameson. "A non-linear effect in the capillary instability of liquid jets." In: *J. Fluid Mech.* 46.2 (1971), pp. 267–271.

[83] F. Savart. In: *Ann. Chem.* 53 (1833), p. 337.

[84] W. A Sirignano and C Mehring. "Review of theory of distortion and disintegration of liquid streams." In: *Prog. Energy Combust. Sci.* 26.4–6 (2000), pp. 609–655.

[85] H. B. Squire. "Investigation of the instability of a moving liquid film." In: *Br. J. Appl. Phys.* 4.6 (1953), pp. 167–169.

[86] A. M. Sterling and C. A. Sleicher. "The instability of capillary jets." In: *J. Fluid Mech.* 68.03 (1975), pp. 477–495.

[87] S. R. Sternberg. "Biomedical image processing." In: *IEEE Computer* 1 (1983), pp. 22–34.

[88] M. Sussman and E. G. Puckett. "A coupled level-set and volume-of-fluid method for computing 3D and axisymmetric incompressible two-phase flows." In: *J. Comput. Phys.* 162.2 (2000), pp. 301–337.

[89] M. Sussman, E. Fatemi, P. Smereka, and S. Osher. "An improved level set method for incompressible two-phase flows." In: *Comput. Fluids* 27.5–6 (1998), pp. 663–680.

[90] M. Sussman, A. S. Almgren, J. B. Bell, P. Colella, L. H. Howell, and M. L. Welcome. "An adaptive level set approach for incompressible two-phase flows." In: *J. Comput. Phys.* 148.1 (1999), pp. 81–124.

[91] K. Taira and T. Colonius. "The immersed boundary method: A projection approach." In: *J. Comput. Phys.* 225.2 (2007), pp. 2118–2137.

[92] S. Taneda. *von Karman vortex street behind a cylinder*. URL: http://lfmi.epfl.ch.

[93] S. Tanguy. "Développement d'une méthode de suivi d'interface. Applications aux écoulements diphasiques." PhD thesis. Université de Rouen, 2004.

[94] G. Taylor. "The dynamics of thin sheets of fluid. III. Disintegration of fluid sheets." In: *Proc. R. Soc. A* 253.1274 (1959), pp. 313–321.

[95] G. Tryggvason, R. Scardovelli, and S. Zaleski. *Direct numerical simulations of gas-liquid multiphase flows*. Cambridge University Press. 2011.

[96] Y. H. Tseng and J. H. Ferziger. "A ghost-cell immersed boundary method for flow in complex geometry." In: *J. Comput. Phys.* 192.2 (2003), pp. 593–623.

[97] P. Vassallo and N. Ashgriz. "Satellite formation and merging in liquid jet breakup." In: *Pro. Math. Phys. Sci.* 433.1888 (1991), pp. 269–286.

[98] G. Vaudor. "Atomisation assistée par un cisaillement de l'écoulement gazeux. Développement et validation." PhD thesis. Université de Rouen, 2015.

[99] G. Vaudor, T. Ménard, W. Aniszewski, M. Doring, and A. Berlemont. "A consistent mass and momentum flux computation method for two phase flows. Application to atomization process." In: *Comput. Fluids* (2017).

[100] R. W. C. P. Verstappen and A. E. P. Veldman. "Symmetry-preserving discretization of turbulent flow." In: *J. Comput. Phys.* 187.1 (2003), pp. 343–368.

[101] E. Villermaux and C. Clanet. "Life of a flapping liquid sheet." In: *J. Fluid Mech.* 462 (2002), pp. 341–363.

[102] G. D. Weymouth and D. K. P. Yue. "Conservative volume-of-fluid method for free-surface simulations on cartesian-grids." In: *J. Comput. Phys.* 229.8 (2010), pp. 2853–2865.

[103] C. Wieselsberger. "New data on the laws of fluid resistance." In: *Technical report, National advisory committee for aeronautics* (1922).

[104] W. Xie and P. E. Desjardins. "A level set embedded interface method for conjugate heat transfer simulations of low speed 2D flows." In: *Comput. Fluids* 37.10 (2008), pp. 1262–1275.

[105] S. Xu. "The immersed interface method for simulating prescribed motion of rigid objects in an incompressible viscous flow." In: *J. Comput. Phys.* 227.10 (2008), pp. 5045–5071.

[106] S. Xu and Z. J. Wang. "An immersed interface method for simulating the interaction of a fluid with moving boundaries." In: *J. Comput. Phys.* 216.2 (2006), pp. 454–493.

[107] T. Ye, R. Mittal, H. S. Udaykumar, and W. Shyy. "An accurate cartesian grid method for viscous incompressible flows with complex immersed boundaries." In: *J. Comput. Phys.* 156.2 (1999), pp. 209–240.

[108] M. C. Yuen. "Non-linear capillary instability of a liquid jet." In: *J. Fluid Mech.* 33.1 (1968), pp. 151–163.

1.4